Techniques avancées de formation de voies en imagerie ultrasonore et problèmes inverses associés

Teodora Szasz

THÈSE

En vue de l'obtention du

DOCTORAT DE L'UNIVERSITÉ DE TOULOUSE

Délivré par : *l'Université Toulouse 3 Paul Sabatier (UT3 Paul Sabatier)*

Présentée et soutenue le *14/10/2016* **par :**

Teodora SZASZ

Advanced beamforming techniques in ultrasound imaging and the associated inverse problems

Techniques avancées de formation de voies en imagerie ultrasonore et problèmes inverses associés

---

JURY

Jean-Louis DILLENSEGER	Maître de conférences, Université de Rennes 1	Rapporteur
Nicole VINCENT	Professeur, Université Paris Descartes	Rapporteur
Philippe DELACHARTRE	Professeur, INSA Lyon	Examinateur
Mircea-Florin VAIDA	Professeur, Université Technique de Cluj-Napoca	Examinateur
Adrian BASARAB	Maître de conférences, Université Paul Sabatier	Directeur de Thèse
Denis KOUAMÉ	Professeur, Université Paul Sabatier	Directeur de Thèse

---

École doctorale et spécialité :
MITT : Image, Information, Hypermédia
Unité de Recherche :
Institut de Recherche en Informatique de Toulouse (UMR 5505)
Directeur(s) de Thèse :
Adrian BASARAB et *Denis KOUAMÉ*
Rapporteurs :
Jean-Louis DILLENSEGER et *Nicole VINCENT*

Acknowledgements

Firstly, I would like to thank Paul Sabatier University members and the doctoral school, EDMITT, for offering me the financial support during these three years of PhD. I am thankful to IRIT laboratory that offered me space and support during the master internship and PhD period. Also, I am grateful to Technical University of Cluj-Napoca, Romania for the financial support through the Erasmus scholarship during the master internship. The internship gave me the opportunity to meet my PhD supervisors, Dr. Adrian Basarab and Prof. Denis Kouamé and to discover the fascinating world of ultrasound imaging.

I will never be able to express in words the gratitude for the permanent support and help of my PhD supervisors Dr. Adrian Basarab and Prof. Denis Kouamé. They helped me integrate in their team and taught me the main concepts of ultrasound imaging and how to approach a PhD thesis. I really appreciate their time spent on correcting my articles. I know that, at the beginning, they probably spent more time on corrections than if they were writing the articles by themselves. But they knew that this is the only way I will be able to learn the right way of writing research articles. Also, I really appreciate their patience during my "learning french" process. I know that at the beginning the meetings in french with them were in a "franglish" language, that sometimes just myself I could understand, but they always motivated me to continue and practice doing presentations in french. This was so helpful when I had to do my first oral presentation in french at GRETSI conference in 2015. Thank you again. Now, looking back at these four years (one of internship and three of PhD), I can say, without any hesitation, that they are the best supervisors I could have. They are are experts in ultrasound imaging, amazing managers of the time and resources,

and wonderful teachers. They motivated me with their passion for research, and guided me very attentively during the entire work I did during my PhD. All the results I had during my PhD (and I am quite proud about them) were not been possible without their special help, guidance, and motivation. Thank you again!

I am truly grateful to Prof. Mircea-Florin Vaida for supporting me in my career since my first year of university at Technical University of Cluj Napoca, Romania. Since almost 10 years he is continuously guiding me in each important step of my career. He offered me the chance to work in a professional research laboratory, at IRIT, and he gave very precious advices, even in the most difficult situations. I really want to thank him for the last days, before my PhD defense, for being near me, encouraging me and motivating me. He always knows how to take out the best of me in critical moments (like preparing a good presentation in 3-4 days, with a terrible jet lag of 7 hours). Prof. Mircea-Florin Vaida is my best example of dedication to the students. He is the only professor I know that is everytime ready to help a good student, no matter of circumstances.

I would also like to thank Dr. Hervé Liebgott and Adeline Bernard from CREATIS laboratory at Lyon for offering me the possibility to work on their US scanners and their precious support during my PhD thesis. Almost all the experimental data in this manuscript was acquired with their US scanners.

Thank you Dr. Zhouye Chen for being in front of me in our office for 3 years. Thank you for being such an amazing colleague and friend. Thank you Rémi Abbal and Renaud Morin for helping me in my first year at IRIT and for being so patient during my "learning french" process. Many thanks to my colleagues and friends NingNing, Rose, Thang, Bérengère, Arturo, and Rémi.

Special thanks to Sébastien for the patience, help, continuously support, and love he offered me during my PhD. Thanks to my friends Julia, Vincent, and Hubert for all the special social moments we spent together.

I am truly grateful to my friend Luis, for inspiring and motivating me to cross borders that I never thought I will we able to pass. "You are the crack in my world".

The support of my family is endless...Thank you for your love, motivation, and for being such an amazing family. I want to dedicate this thesis to you.

Contents

Abstract

Ultrasound (US) allows non-invasive and ultra-high frame rate imaging procedures at reduced costs. Cardiac, abdominal, fetal, and breast imaging are some of the applications where it is extensively used as diagnostic tool.

In a classical US scanning process, short acoustic pulses are transmitted through the region-of-interest of the human body. The backscattered echo signals are then beamformed for creating radiofrequency(RF) lines. Beamforming (BF) plays a key role in US image formation, influencing the resolution and the contrast of final image.

The objective of this thesis is to model BF as an inverse problem, relating the raw channel data to the signals to be recovered. The proposed BF framework improves the contrast and the spatial resolution of the US images, compared with the existing BF methods.

To begin with, we investigated the existing BF methods in medical US imaging. We briefly review the most common BF techniques, starting with the standard delay-and-sum BF method and emerging to the most known adaptive BF techniques, such as minimum variance BF.

Afterwards, we investigated the use of sparse priors in creating original two-dimensional beamforming methods for ultrasound imaging. The proposed approaches detect the strong reflectors from the scanned medium based on the well-known Bayesian Information Criteria used in statistical modeling.

Furthermore, we propose a new way of addressing the BF in US imaging, by formulating it as a linear inverse problem relating the reflected echoes to the signal to be recovered. Our approach offers flexibility in the choice of statistical assumptions on the signal to be beamformed and it is robust to a reduced number of pulse emissions.

At the end of this research, we investigated the use of the non-Gaussianity properties of the RF signals in the BF process, by assuming α-stable statistics of US images.

List of Figures

LIST OF FIGURES

LIST OF FIGURES

List of Tables

LIST OF TABLES

Glossary

2D Two-dimensional

3D Three-dimensional

A4C Apical 4 Chambers

ADM alternating direction method

BF Beamforming

BIC Bayesian Information Criteria

BP Basis Pursuit

BS-Capon Beamspace Capon

CNR Contrast-to-noise ratio

CR Contrast ratio

CS Compressive Sensing

DAS Delay-and-Sum

DFT Discrete Fourier Transform

DL Diagonal loading

EN Elastic-net

ES-Capon Element-space Capon

Field II Ultrasound simulator software package

FWHM Full width at half maximum

IAA Iterative Adaptive Approach

LASSO Least Absolute Shrinkage and Selection Operator

LCMV Linear Constrained Minimum Variance

LS Least Squares

LV Left Ventricle

M-USBIC Beamformer based on MV RF image

ML Maximum Likelihood

MUSIC MUltiple SIgnal Classification

MV Minimum Variance

OMP Orthogonal Matching Pursuit

RF Radiofrequency

RG Resolution Gain

RV Right Ventricle

SαS Symmetric α-stable

SINR Signal-to-interference-plus-noise ratio

SNR Signal-to-noise ratio

TGC Time Gain Compensation

US Ultrasound

USBIC Beamformer based on DAS RF image

YALL1 Software package to solve optimization problems

RESUME ETENDU

Introduction

L'imagerie ultrasonore (US) est l'une des techniques d'imagerie médicale qui connait les développements les plus rapides notamment grâce à ses propriétés non invasives, ses méthodes d'acquisition rapides, et son coût modéré. L'imagerie cardiaque, abdominale, fœtale, ou mammaire sont quelques-unes des applications où elle est largement utilisée comme outil de diagnostic.

En imagerie US classique, des ondes acoustiques sont transmises à une région d'intérêt du corps humain. Les signaux d'écho rétrodiffusés, également appelés données brutes, sont ensuite traités pour créer des lignes radiofréquences (RF). **La formation de voies** (FV) joue un rôle clé dans l'obtention des images US, car elle influence la résolution et le contraste de l'image finale. La méthode standard en formation de voies dite DAS ("delay-and-sum") consiste à retarder et à pondérer les échos réfléchis avant de les moyenner. Les méthodes de FV existantes utilisent des poids fixes ou adaptatifs pour le moyennage. L'objectif de ce travail est de modéliser la formation de voies comme un problème inverse liant les données brutes aux signaux RF. Le modèle de formation de voies proposé ici améliore le contraste et la résolution spatiale des images échographiques par rapport aux techniques de FV existants.

Le premier chapitre de cette thèse donne le cadre théorique de l'imagerie US. En premier lieu, nous presentons les caractéristiques des signaux US, et fournissons une analyse de la propagation des ondes. Ensuite, nous présentons l'imagerie médicale US, et la manière dont les images sont affichées. Enfin, la formation de voies est introduite et les principales méthodes de formation de voies sont brièvement décrites, ainsi que leurs limites.

Le second chapitre présente l'état de l'art des méthodes de formation de voies existantes en imagerie médicale ultrasonore. Nous passons brièvement en revue les techniques de formation de voies les plus courantes, en commençant par la méthode dite DAS, puis les techniques émergentes les plus connues de formation de voies adaptatives, en mettant l'accent sur la méthode à variance minimale (MV) ainsi que ses variantes.

Une comparaison détaillée des différentes méthodes de formation de voies est ensuite présentée.

Le troisième chapitre propose l'utilisation des signaux qui exploitent une représentation parcimonieuse de l'image US. Notre méthode est basée sur la création de méthodes de formations de voies originales en deux dimensions pour l'imagerie US. Les approches proposées détectent les réflecteurs forts du milieu à imager sur la base de critères bayésiens bien connus et utilisés dans la modélisation statistique. En outre, ils permettent une sélection du niveau de bruit dans l'image finale BF.

Dans *le quatrième chapitre*, nous proposons une nouvelle façon d'aborder la formation de voies en imagerie US, en la formulant comme un problème inverse linéaire liant les échos réfléchis au signal final. Notre approche présente deux avantages majeurs : i) sa flexibilité dans le choix des hypothèses statistiques sur le signal avant la formation de voies (les statistiques Laplaciennes et Gaussiennes) et ii) sa robustesse à un nombre réduit d'impulsions d'émissions. Le cadre proposé est souple et permet de trouver un compromis entre la suppression du bruit et la netteté de l'image résultante. Nous illustrons la performance de notre approche à la fois sur des données simulées et sur des données *in vivo* de carotide et de thyroïde.

Dans *le cinquième chapitre*, nous présentons une nouvelle méthode de formation de voies pour l'imagerie médicale US basée sur l'utilisation de caractéristiques statistiques des signaux supposées α-stable. Bien que le traitement du signal US se soit largement appuyé pendant de nombreuses années sur l'hypothèse Gaussienne, il a été montré que les échos RF peuvent être modélisés avec plus de précision par une loi statistique à "queue lourde". Par exemple, les propriétés statistiques des signaux RF peuvent être considérés, d'après le théorème central limite generalisé, α-stables. La principale contribution de ce chapitre est l'utilisation des propriétés non-gaussiennes des signaux RF dans le processus de formation de voies. Il s'agit de la première tentative considérant spécifiquement une distribution α-stable, pour la formation de voies en imagerie US.

Enfin, *le sixième chapitre* présente les contributions de la thèse et les perspectives.

Chapitre 1 : L'imagerie ultrasonore

Principe de l'imagerie ultrasonore

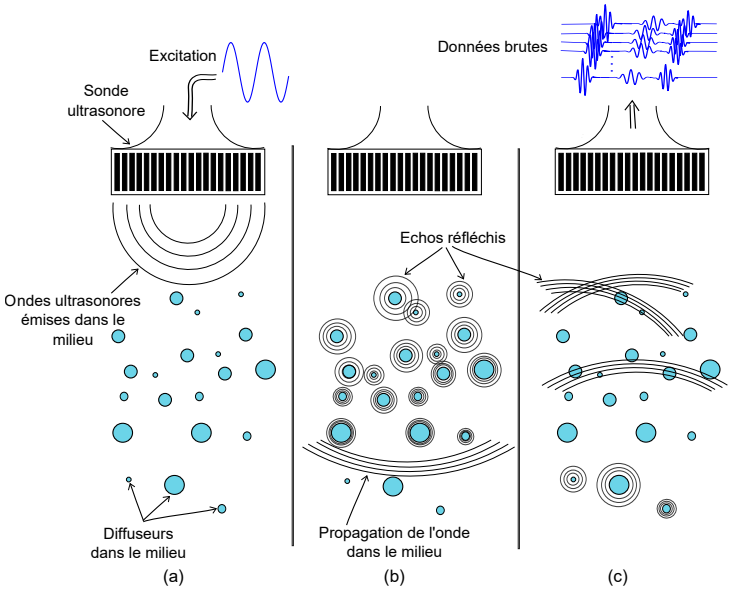

Figure 1: Principe de l'imagerie US : (a) une impulsion électrique (excitation) est transmise au transducteur piézoélectrique qui la transforme en une onde US; (b) l'onde se propage et interagit avec le milieu; (c) les ondes réfléchies reçues par le transducteur sont converties en signaux électriques (données brutes).

Le principe de l'imagerie ultrasonore (US) est illustré à la Fig. 1. Il repose sur l'interaction entre les ondes US et le milieu qui contient les diffuseurs. Ces dernières sont produites à l'aide de matériaux piézoélectriques constituant la sonde US et sont émises en direction du milieu (Fig. 1(a)). Au cours de leur propagation à travers le milieu, des phénomènes de réflexion et de transmission se produisent à l'interface de milieux ayant différentes impédances acoustiques. De plus, l'amplitude de l'onde US est atténuée en raison des phénomènes d'absorption et de diffusion [Kuttruff, 1991].

Actuellement, la grande majorité des sondes US sont constituées de plusieurs éléments disposés linéairement ou sectoriellement. Ils permettent à la fois l'émission des ondes US et la réception des échos réfléchis par le milieu (Fig. 1(b)). Ces échos, transformés en signaux électriques puis numérisés, représentent les données brutes acquises par le système US (Fig. 1(c)). Afin d'améliorer la résolution spatiale, le rapport signal

sur bruit, ainsi que le contraste des images, des méthodes de formation de voies sont appliquées aux données US brutes pour produire des signaux radiofréquences (RF).

Visualisation des images ultrasonores

Pour des raisons de lisibilité, les images RF sont finalement converties en images en mode B (brillance), à l'aide de post-traitements classiques tels que le filtrage passe-bande, la détection d'enveloppe et la compression logarithmique. Afin de pouvoir comparer les résultats proposés dans cette thèse avec les techniques de formations de voies existantes, nous utiliserons les mesures les plus courantes de qualité d'image : le rapport de contraste (RC) [Xu et al., 2014a], le rapport contraste sur bruit (RCB) [Rindal et al., 2014], et le rapport signal sur bruit (RSB) [Jensen and Austeng, 2014].

Formation de voies en imagerie ultrasonore

Les techniques de formation de voies jouent un rôle majeur dans la qualité des images US [Van Veen and Buckley, 1988]. La méthode couramment employée en imagerie US utilise les opérations classiques de retard et somme dite DAS (delay-and-sum) [Thomenius, 1996]. Avec cette méthode, les donées brutes reçues par les éléments de la sonde sont d'abord focalisées afin de compenser les retards dus aux différences de temps de propagation, avant d'être sommées en les pondérant par des coefficients. Ces coefficients forment la fenêtre d'apodisation en réception. Malgré son avantage lié essentiellement à sa rapidité, la méthode par retard et somme ne permet pas d'obtenir une résolution spatiale et un contraste optimal. Afin d'améliorer la qualité des images RF, de nombreux travaux existant proposent d'adapter les fenêtres d'apodisation aux données, ou autrement dit de les estimer à partir des données brutes. L'une des méthodes les plus utilisées est celle du filtre de Capon [Capon, 1969]. Son rôle est d'appliquer une fenêtre d'apodisation optimale afin d'estimer la forme d'onde du signal désiré aussi précisément que possible, tout en rejetant les signaux indésirables. D'autres exemples de formeurs de faisceaux adaptatifs sont les techniques MUSIC [Schmidt, 1981] et Maximum Likelihood (ML)([Krim and Viberg, 1996, Stoica and Sharman, 1990]).

Chapitre 2 : La formation de voie dans l'imagerie médicale ultrasonore : état de l'art

La formation de voies (FV) permet d'amplifier les signaux réfléchis depuis des positions connues, tout en atténuant les signaux provenant de positions indésirables. Ceci est classiquement réalisé en retardant et en appliquant des poids spécifiques aux signaux réfléchis. Les formeurs de voies peuvent être soit indépendants des données (fixes), dépendants des données (adaptatifs), en fonction du calcul des poids appliqués aux signaux réfléchis.

Formation de voies non-adaptative

La formation de voies par retard et somme, dite DAS (delay-and-sum), sélectionne les poids $\boldsymbol{w}_{DAS}$ indépendamment des données :

$$\boldsymbol{w}_{DAS} = \frac{\mathbf{1}}{M}, \tag{1}$$

où $\mathbf{1}$ est un vecteur colonne de longueur M constitué de "un" car les données brutes ont été focalisées à l'aide de retards.

Nous considérons ci-après le schéma d'acquisition classique où une série de K voies focalisées est transmise avec M éléments. Les K voies focalisées sont transmises avec des angles d'incidence différents $\theta_k, k = 1, \cdots, K$. L'image finale RF US est un ensemble de lignes RF. Chacune d'elle étant le résultat de la formation de voies à partir des signaux RF bruts provenant d'une émission dans la direction θ_k, $k \in \{1, \ldots, K\}$, en utilisant M éléments du transducteur. La formation de voies classique par retard et somme peut être exprimée comme suit :

$$\hat{\boldsymbol{s}}_k = \boldsymbol{w}^H \boldsymbol{y}_k, \tag{2}$$

où $\boldsymbol{y}_k \in \mathbb{C}^{M \times N}$ sont les données brutes compensées en temps reçues par le m-ième élément de la sonde US, et correspondant à l'émission dans la direction θ_k, et $\boldsymbol{w}$ est le vecteur des poids du formateur de voies et de taille $M \times 1$.

Formation de voies adaptative

Bien que la formation de voies par retard et somme utilise des poids fixes, le but de la formation de voies à variance minimum (MV) est d'appliquer un ensemble de poids dépendant des données (d'où le nom adaptatif). Ceci afin d'estimer la forme d'onde

du signal désiré aussi précisément que possible, tout en rejetant les signaux parasites. L'expression des poids utilisés par la MV est :

$$\boldsymbol{w}_{MV} = \frac{\boldsymbol{R}_k^{-1}\mathbf{1}}{\mathbf{1}^T\boldsymbol{R}_k^{-1}\mathbf{1}}, \tag{3}$$

où $\boldsymbol{R}_k$ est la matrice de covariance. Il est à noter que dans la pratique, une simple estimation de la matrice de covariance peut être faite. Celle-ci peut être mal conditionnée et ainsi engendrer des résultats moins bons que ceux de la méthode par retard et somme.

Afin d'améliorer la robustesse de la formation de voies MV, différentes techniques ont été proposées dans la littérature : sous-matrice d'étalement (pour décorréler des signaux cohérents), moyenne temporelle (pour conserver des statistiques de speckle), rehaussement de la diagonale (pour améliorer la robustesse de l'inversion de la matrice de covariance), pondération par facteur de cohérence (pour augmenter la résolution et le contraste de l'image obtenue après l'application de la méthode MV), ou encore utilisation de sous-bandes de fréquences.

La formation de voies dans d'autres domaines

Un problème particulier résolu par la formation de voie est la localisation de sources (en particulier sur la direction d'arrivée). Le problème inverse sur lequel est basé le problème de la localisation des sources peut être exprimé comme suit :

$$\boldsymbol{y} = T(\boldsymbol{x}) + \boldsymbol{n}, \tag{4}$$

où $\boldsymbol{x} \in \mathcal{X}$ est inconnu, $\boldsymbol{y} \in \mathcal{Y}$ est le vecteur des mesures (observations), $\mathcal{X}$, sont des espaces de Hilbert, et $\boldsymbol{n}$ est un bruit blanc gaussien. Le but est de trouver $\boldsymbol{x}$ à partir de $\boldsymbol{y}$ connaissant la transformation T. La solution de (4) est généralement présentée comme :

$$\hat{\boldsymbol{x}} = \underset{\boldsymbol{x}}{\operatorname{argmin}}(\|\boldsymbol{y} - T(\boldsymbol{x})\|_2^2 + P(\boldsymbol{x})), \tag{5}$$

où le premier terme, $\|\boldsymbol{y} - T(\boldsymbol{x})\|_2^2$ est le terme d'attache aux données, et $P(\boldsymbol{x})$ est une fonction traduisant les connaissances à priori sur $\boldsymbol{x}$. Ce terme est aussi appelé le terme de régularisation. Dans cette thèse, nous avons modélisé le problème de FV en imagerie médicale US en utilisant le problème inverse formulé dans (4) et nous avons appliqué différentes techniques de régularisation dans le but de résoudre (5).

Chapitre 3 : Formation de voies par detection des échos forts en imagerie ultrasonore

Dans ce chapitre, nous proposons une méthode de formation de voies qui exploite une représentation parcimonieuse des images RF. Une détection automatique des forts échos susceptibles de représenter les frontières entre les organes ou des structures hyperéchogènes a été effectuée en réalisant un compromis entre la parcimonie spatiale de ces structures et la forme des données brutes. L'image ainsi obtenue est par la suite combinée linéairement avec une image classiquement formée, afin de garder le speckle habituel des images. Nous avons montré à travers des résultats de simulations réalistes et un résultat expérimental sur fantôme (matériau de test) que la méthode proposée améliore le contraste et le rapport signal sur bruit comparé à des approches de formation de voies classiques.

Formation de voies proposée

La détection est basée sur un compromis entre la parcimonie spatiale des images obtenues et le respect des données brutes. Le modèle parcimonieux de l'image RF considéré s'écrit sous la forme suivante [Tur et al., 2011] :

$$\begin{gathered}\boldsymbol{S}(x,n) = \sum_{p=1}^{P} a_p \boldsymbol{h}_p(x - x_p, n - n_p), \\ x = x_1, \cdots, x_M \quad \text{et} \quad n = 1, \cdots, N,\end{gathered} \tag{6}$$

avec n et x les variables spatiales respectivement axiales (dans la direction de propagation des ondes) et latérales, $\boldsymbol{S}(x,n)$ la représentation parcimonieuse de l'image RF après formation des voies, (x_p, n_p) avec $p = 1 \cdots P$ les positions spatiales des P plus forts diffuseurs du milieu imagé. Les a_p représentent les amplitudes des diffuseurs et $\boldsymbol{h}_p(x,n)$ sont les formes d'ondes réfléchies par chaque diffuseur.

Dans notre modèle, les positions, les amplitudes et les réponses produites par chaque diffuseur sont considérées inconnues et seront estimées. La parcimonie est liée au fait que le nombre de diffuseurs forts K est très faible dans la grille spatiale 2D des positions considérées initialement par le formeurs de voies. Notre méthode est constituée de deux étapes. La première détecte un fort diffuseur potentiel en se basant sur l'image RF formée par l'approche par retard et somme ou par variance minimum. La deuxième étape valide ce choix en évaluant l'évolution d'une fonction de coût faisant appel aux données

brutes. A chaque itération, le nouveau diffuseur détecté est accepté selon une fonction de coût dont l'objectif est de trouver un compromis entre un faible nombre d'échos forts et le respect des données brutes. Cette fonction, inspirée du critère d'information Bayesien [Konishi and Kitagawa, 2008] est adaptée à l'imagerie US.

Expériences

Les approches proposées, nommées USBIC (basées sur le retard et la somme) et M-USBIC (basé sur la variance minimum), ont été évaluées sur trois différents exemples simulés en utilisant le programme de simulation Field II et des acquisitions sur des fantômes US. Le premier milieu simulé est basé sur une hypothèse de réflecteurs parcimonieux. Le second est basé sur des données simulées à partir d'un milieu contenant des réflecteurs parcimonieux, un kyste, et du speckle, en utilisant une sonde multi-éléments. Le troisième exemple représente la simulation d'une image cardiaque en vue apicale 4-chambre (A4C), comme suggérée dans [Alessandrini et al., 2012]. Les données expérimentales ont été acquises avec une plateforme de recherche Ultrasonix MDP.

Résultats

La première simulation consiste en un milieu contenant 14 réflecteurs parcimonieux, alignés latéralement à -2 mm et 2 mm. Le milieu ne contient pas du speckle. Dans la simulation, nous avons évalué le potentiel des méthodes proposées à détecter avec précision les réflecteurs forts dans des milieux parcimonieux. Les résultats montrent que l'ensemble des 14 réflecteurs positionnés parcimonieusement est détecté aux positions correctes. La deuxième simulation contient des réflecteurs forts et un kyste dans un milieu avec du speckle. Le principal avantage de notre méthode est d'améliorer le contraste pour des structures hyperéchogènes. Cependant, en ajoutant le speckle sur des images finales, malgré une réduction du contraste, nous parvenons à maintenir un contraste voisin de celui obtenu par des techniques de formation de voies existantes. Troisièmement, les résultats de formation de voies sur une vue A4C simulée montrent que les méthodes proposées améliorent le contraste des structures du ventricule, tout en conservant leurs formes. Enfin, en les appliquant sur des données expérimentales, nous avons montré que la méthode proposée offre un meilleur compromis entre le contraste et la préservation du speckle, comparée aux formateurs de voies par retard et somme et à variance minimum.

Chapitre 4 : Formation de voies en imagerie ultrasonore par un problème inverse régularisé

Dans ce chapitre, nous proposons d'effectuer la formation de voies en imagerie ultrasonore par un problème inverse régularisé basé sur un modèle linéaire reliant les échos réfléchis au signal final recherché. La contribution majeure de ce chapitre est l'amélioration des techniques de formation de voies existantes en combinant le modèle direct proposé formulé suivant la direction latérale des images avec une approche d'inversion régularisée. De plus, la méthode proposée permet de réduire fortement le nombre d'émissions US requises.

En premier lieu, les statistiques laplaciennes (ℓ_1) et gaussiennes (ℓ_2), deux des régularisations les plus courantes dans de tels problèmes d'imageries, seront considérées ici ([Chen et al., 1998, Tikhonov, 1963]). En second lieu, nous avons également appliqué à notre cadre, une méthode de régularisation complexe combinant ℓ_1 et ℓ_2, appelée régularisation « elastic-net » [Zou and Hastie, 2005]. En outre, notre méthode ouvre de nouvelles perspectives pour les termes de régularisation plus complexes (par exemple, [Chen et al., 2016a, Michailovich and Rathi, 2015]) pour améliorer davantage les résultats.

Formation de voies proposée

La méthode proposée est appliquée séquentiellement de la même manière à chaque échantillon (profondeur). Pour chaque profondeur n, nous souhaitons estimer le signal correspondant à un réflecteur en fonction de son emplacement, qui contiendra des pics dominants à la position des réflecteurs. Nous rappelons ici que nous utilisons le même mode d'acquisition que celui décrit dans le Chapitre 2, où une série de K voies focalisées sont transmises avec M éléments, avec des angles d'incidence différents $\theta_k, k = 1, \cdots, K$. Comme il s'agit de plusieurs directions, pour réduire la complexité élevée, nous proposons d'utiliser les données formées par la méthode par retard et somme au lieu de les former à partir des données brutes. Ensuite, nous utilisons un outil couramment utilisé dans les approches de localisation des sources permettant de réduire la complexité de calcul [Fuchs, 1996, Tian and Van Trees, 2001]. Plus précisément, pour chaque profondeur n, nous projetons les données obtenues lors de la formation de voies par retard

et somme dans un nouvel espace de formation de voies representé par les matrices $\boldsymbol{A}$ et $\boldsymbol{A}_{BS}$.

Notre modèle est formulé ainsi :

$$\boldsymbol{z}[n] = (\boldsymbol{A}_{BS}^H \boldsymbol{A})\boldsymbol{x}[n] + \boldsymbol{D}^H \boldsymbol{g}[n], \tag{7}$$

où $\boldsymbol{z}[n] \in \mathbb{C}^{P\times 1}$ est le vecteur transformé formé par l'échantillonnage des lignes latérales formées par la methode par retard et somme sur une grille de P positions, $\boldsymbol{D}$ de taille $K \times P$ est une matrice de décimation, $\boldsymbol{x}[n]$ de taille $K \times 1$ est le profil latéral à estimer à la profundeur n, et $\boldsymbol{A}$ respectivement $\boldsymbol{A}_{BS}$ sont les matrices de projection des capteurs vers les reflecteurs dans le milieu et des reflecteurs vers les capteurs.

Une façon d'inverser le problème est d'utiliser des techniques standards de régularisation. En considérant que le signal $\boldsymbol{x}[n]$ suit les statistiques laplaciennes, la minimisation de la fonction de coût s'écrit :

$$\boldsymbol{x}[n] = \underset{\boldsymbol{x}[n]}{\operatorname{argmin}}(||\boldsymbol{z}[n] - (\boldsymbol{A}_{BS}^H \boldsymbol{A})\boldsymbol{x}[n]||_2^2 + \lambda||\boldsymbol{x}[n]||_1), \tag{8}$$

où $||\cdot||_1$ désigne la norme ℓ_1. Nous avons utilisé l'outil d'optimisation YALL 1 [Zhang, 2009] pour résoudre (8).

Expériences

Les approches proposées, appelées de façon générique dans ce chapitre : « Base Pursuit beamforming » (BP BF), « Least Squares beamforming » (LS BF), et « Elastic-Net beamforming » (EN BF), ont été évaluées en utilisant des données simulées et des données expérimentales *in vivo* de la carotide et de la thyroïde.

Résultats

Nous présentons les résultats de formation de voies sur des données de la thyroïde avec une tumeur. Nous pouvons observer que contrairement à l'image DAS, où la tumeur est difficile à distinguer (voir Fig. 2(a)), les méthodes proposées (BP, LS, et EN) améliorent la visualisation des principales structures, et renforcent les bords de la tumeur (voir Fig. 2(b)-(d)).

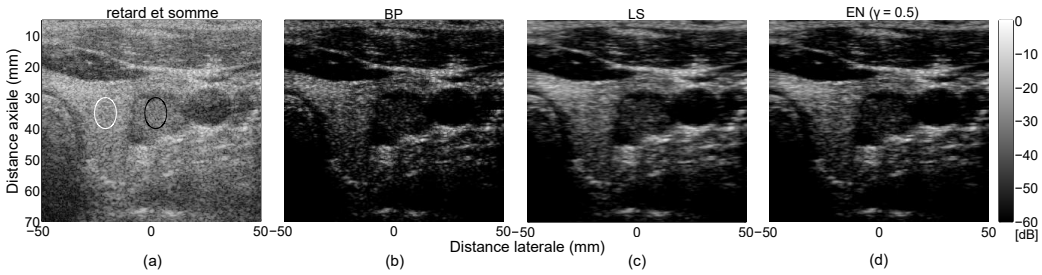

Figure 2: Les résultats de la formation de voies (a) par retard et somme, (b) BP, (c) LS, et (d) EN ($\gamma = 0.8$) sur des données *in vivo* de la thyroïde avec une tumeur.

Conclusions

Contrairement aux techniques existantes qui utilisent des poids adaptatifs, nous avons regularisé notre problème inverse de formation de voies en utilisant des hypothèses statistiques laplaciennes, gaussiennes, et « elastic-net ». La FV à base de régularisation proposée permet de réduire fortement le nombre de transmissions US (par un facteur cinq dans nos exemples), tout en améliorant la qualité des images formées en termes de résolution et de contraste par rapport aux formeurs de voies existants.

Chapitre 5 : Formation de voies en imagerie ultrasonore utilisant une loi stable

Dans ce chapitre, nous présentons une nouvelle méthode de formation de voies basée sur la caractérisation statistique des signaux par des distributions α-stable. La principale contribution présentée dans ce chapitre est l'utilisation des propriétés non gaussiennes des signaux RF dans le processus de formation de voies (voir par exemple [Pereyra and Batatia, 2012, Alessandrini et al., 2011, Zhao et al., 2016b]). A notre connaissance, ceci est la première tentative de considérer spécifiquement une distribution α-stable pendant la formation de voies en imagerie US.

Formation de voies proposée

Le modèle linéaire direct présenté dans le Chapitre 4 est ici inversé en utilisant une régularisation par pseudo-norme plus générale ℓ_p, avec p automatiquement lié au paramètre α estimé à partir des données brutes [Achim et al., 2015]. Notre solution de FV est basée sur l'hypothèse d'une distribution α-stable des signaux US. La loi stable est une généralisation de la distribution gaussienne (pour $\alpha = 2$, la distribution stable est réduite à la distribution gaussienne) [Shao and Nikias, 1993].

Dans [Achim et al., 2015], il a été montré que la régularisation par norme ℓ_p est bien adaptée pour reconstruire des signaux suivant une distribution α-stable symétrique ($S\alpha S$). En outre, il a été démontré que le choix optimal pour le paramètre p est plus petit, mais aussi proche que possible de α [Achim et al., 2015], généralement $p = \alpha - 0,01$. Selon le degré de parcimonie du milieu, la valeur de p, directement liée à α estimée à partir de $\boldsymbol{y}$ (soit $p = \alpha - 0,01$) peut prendre des valeurs plus petites que 1. Dans ce cas, la fonction de coût à minimiser devient non convexe. Plusieurs solutions pour résoudre ces problèmes non convexes existent dans la littérature. Dans ce travail, nous avons utilisé l'algorithme d'optimisation semi-quadratique proposé dans [Cetin and Karl, 2001].

Expériences

Afin d'évaluer la méthode de FV proposée (notée FV α-stable), nous avons utilisé à la fois des données simulées et *in vivo*. Les données simulées contiennent 3 diffuseurs situés à 50 mm de profondeur et une structure de kyste anéchoïque de 10 mm de rayon

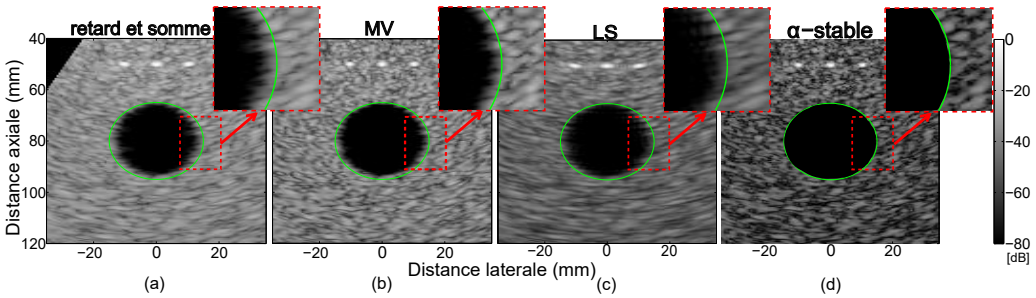

Figure 3: Les résultats de la formation de voies (a) par retard et somme, (b) à variance minimum (c) LS, et (d) α-stable sur des données simulées contenant 3 réflecteurs et un kyste hypoéchogène.

situé à 80 mm de profondeur, noyés dans du speckle. Les émissions correspondaient à 52 ondes planes (pour la méthode proposée) et à 260 ondes planes (pour les méthodes de formation de voies par retard et somme et à variance minimum) transmises avec des angles compris entre -30° et 30°. Les données *in vivo* représentent la glande thyroïde d'un sujet atteint d'une tumeur maligne. L'acquisition a été réalisée avec un système clinique d'échographie Sonoline Elegra modifié à des fins de recherche, et équipé d'un transducteur en réseau linéaire Siemens Medical Systems 7.5L40 P / N 5260281-L0850 émettant des séries d'ondes focalisées.

Résultats

Nous présentons ici les résultats de FV des données simulées contenant 3 réflecteurs et un kyste hypoéchogène. Nous pouvons observer que la formation de voies par retard et somme (Fig. 3(a)) n'est pas en mesure de résoudre la dimension du kyste circulaire. En effet, le kyste apparaît plus étroit que sa dimension d'origine, en raison de la faible résolution fournie par la formation de voies par retard et somme. La méthode à variance minimum (Fig. 2(b)) et la LS (Fig. 2(c)) fournissent de meilleurs résultats, à savoir une dimension du kyste plus proche de sa dimension réelle. Toutefois, lorsque nous utilisons une formation de voies α-stable (Fig. 2(d)), nous obtenons de meilleurs résultats en termes de résolution spatiale, de contraste , par rapport aux méthodes par retard et somme, à variance minimum et LS. Nous notons que les méthodes par retard et somme et à variance minimum ont utilisé des données brutes obtenues avec cinq fois plus d'émissions US que notre méthode (i.e 260 ondes planes). Grâce à cet exemple,

nous avons montré le potentiel de notre méthode à travailler avec un nombre réduit d'émissions.

Conclusions

Dans ce chapitre, nous avons proposé une nouvelle méthode de formation de voies en généralisant le modèle proposé précédemment (présentée dans le Chapitre 4). Notre méthode utilise une régularisation par pseudo-norme ℓ_p pour résoudre notre problème inverse. De plus, p est calculé automatiquement en le reliant aux statistiques α-stables des images US. Ainsi, notre méthode, contrairement aux approches à variance minimale, ne nécessite qu'un seul réglage des paramètres. Elle pourrait également être d'un intérêt dans d'autres domaines d'application tels que l'estimation de la direction d'arrivée. Les travaux futurs porteront sur l'évaluation d'autres stratégies d'acquisition (par exemple, émissions d'ultrasons dans des directions aléatoires) ou encore sur la prise en compte des termes de régularisation communs pour la reconstruction conjointe de plusieurs lignes latérales.

Introduction

Ultrasound (US) imaging is one of the most fast-developing medical imaging techniques, allowing non-invasive and ultra-high frame rate procedures at reduced costs. Cardiac, abdominal, fetal, and breast imaging are some of the applications where it is extensively used as diagnostic tool.

In a classical US scanning process, short acoustic pulses are transmitted through the region-of-interest of the human body. The backscattered echo signals, also called raw channel data, are then processed for creating radiofrequency (RF) beamformed lines. **Beamforming** (BF) plays a key role in US image formation, influencing the resolution and the contrast of final image. The standard way of BF is to delay and weight the reflected echoes before averaging them. Most of the existing BF methods are using fixed (data-independent) or adaptive (data-depended) weights. The focus of these methods is to calculate the weights applied to the reflected echoes, such that only the signals of interest are preserved. Data-independent BF methods provide results with low resolution and contrast. The results are improved by data-dependent BF methods. However, their computation complexity is high and they are not adequate for real-time applications.

The objective of this work is to model BF as an inverse problem, relating the raw channel data to the signals to be recovered. The proposed BF framework improves the contrast and the spatial resolution of the US images, compared with the existing BF methods.

The first chapter of the thesis provides the background of ultrasound imaging. Firstly, it illustrates the characteristics of US signals, and analyzes the propagating waves. Secondly, beamforming technique is introduced. Then, the main source localization methods are briefly described, together with their limitations. Thirdly, we present the medical US imaging, and the way the US images are displayed.

The second chapter provides the state-of-the-art of the existing BF methods in medical US imaging. We briefly review the most common beamforming techniques, starting with the standard delay-and-sum (DAS) BF method and emerging to the most known adaptive BF techniques, with focus on the minimum variance (MV) BF and its improvements. A detailed comparison between the presented BF methods is presented.

The third chapter investigates the use of sparse priors in creating original two-dimensional beamforming methods for ultrasound imaging. The proposed approaches detect the strong reflectors from the scanned medium based on the well-known Bayesian Information Criteria used in statistical modeling. Moreover, they allow a parametric selection of the level of speckle in the final beamformed image.

In the *fourth chapter*, we propose a new way of addressing the BF in US imaging, by formulating it as a linear inverse problem relating the reflected echoes to the signal to be recovered. Our approach presents two major advantages: i) its flexibility in the choice of statistical assumptions on the signal to be beamformed (Laplacian and Gaussian statistics are tested herein) and ii) its robustness to a reduced number of pulse emissions. The proposed framework is flexible and allows for choosing the right trade-off between noise suppression and sharpness of the resulted image. We illustrate the performance of our approach on both simulated and experimental data, with *in vivo* examples of carotid and thyroid.

In *the fifth chapter*, we present a new beamforming method for ultrasound medical imaging based upon the statistical characterization of the ultrasound signals by α-stable distributions. In the chapter four we have reformulated BF in US imaging as a linear inverse problem, associating the raw channel data to the RF signals to be recovered. While US signal processing has widely relied for many years on the assumption of Gaussianity it was shown that RF echoes can be more accurately modelled by a power-law shot noise model. For example, the statistical properties of the RF signals were related, based on the generalized central limit theorem, to α-stable distributions. The main contribution of this chapter is the use of the non-Gaussianity properties of the RF signals in the beamforming process. This is the first attempt of specifically considering an α-stable distribution while beamforming the received echoes in US imaging.

Finally, *the sixth chapter* discusses the contributions of the thesis and the future works.

1

Ultrasound imaging

Before we discuss about the beamforming process and contributions we proposed, it is necessary to present the main principles of ultrasound imaging. Thus, we start the first chapter of the manuscript by presenting the most important aspects of ultrasound (US) imaging, which are very important for a good understanding of the material presented in this thesis. Firstly, the principle of ultrasound imaging is described, together with the basic physical phenomenon. Then, the techniques for US image visualization, with focus on medical US imaging are presented. Finally, the basics of beamforming (BF) are introduced, and some of the most common BF techniques are described.

1.1 Ultrasound imaging principles

We start this chapter by describing the basic principle of US imaging, including sound propagation and classical scanning methods of the medium.

1.1.1 Principle of ultrasound imaging

Ultrasonic field has been extensively developing since 1970s and it represents approximately 25% of all medical imaging examinations performed in the world at the beginning of 21st century [(IAEA), 2014]. There exist distinct fields of study within ultrasonics, with different applications, as: underwater acoustics, applications for monitoring and control, medical ultrasonics for therapy, diagnosis, surgery, biotechnology, nanotechnology, and defense. All these domains are in continuous development.

Ultrasound signals are acoustical waves with frequencies in the range 20 kHz to 1 GHz. These waves are produced by electrically exciting a piezoelectric transducer which is capable of generating and detecting ultrasound energy. Note that the same transducer is used for both transmission and reception of the ultrasound waves in the medium. In function of their frequencies, the acoustic waves can be classified as:

- **Infrasounds**: $f \leq 20$ Hz. These sound waves cannot be perceived by human ear. Their main application is monitoring the earthquakes.

- **Audible sounds**: 20 Hz $\leq f \leq$ 20 kHz. This is the hearing range of frequencies in humans and most of the animals.

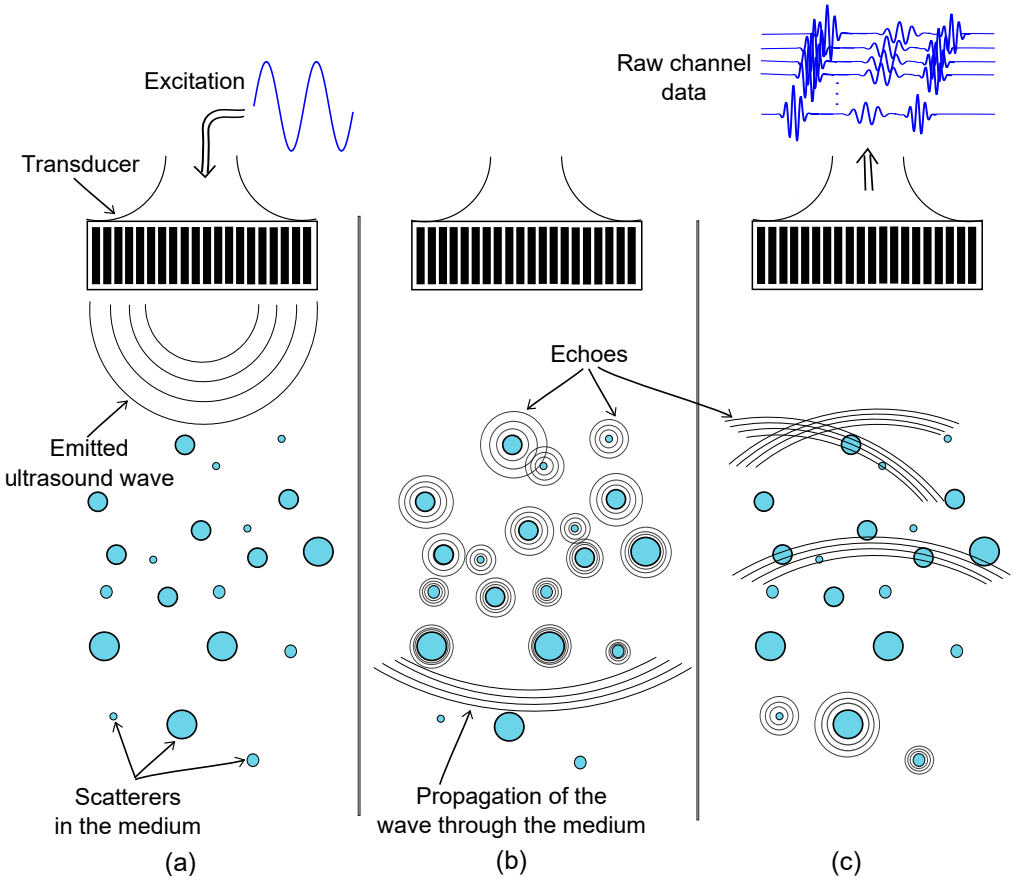

Figure 1.1: The principle of ultrasound imaging: (a) an electrical pulse (excitation) is transmitted to the piezoelectric transducer, transforming the pulse into an ultrasound wave; (b) the wave propagates and interacts with the medium; (c) the reflected waves received by the transducer are transformed in electrical signals (raw channel data).

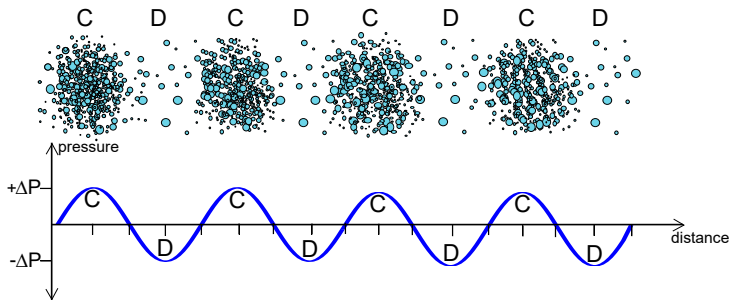

Figure 1.2: Propagation of a 1D longitudinal wave in homogeneous, loss-less medium. The pressure $p(x,t)$ is alternatively compressed (C) and expanded (D).

- **Ultrasounds**: 20 kHz $\leq f \leq$ 1 GHz. They contain frequencies higher than the upper audible limit of human hearing. Their main application domains are industry and medicine.

- **Hypersounds**: $f \geq$ 1 GHz. They are also called 'microwave acoustics'. A quantitative investigation of such waves can be done using Bragg diffraction [Kuttruff, 1991].

Fig. 1.1 presents the basic principle of ultrasound imaging. Firstly, acoustic waves (vibrations) are generated (Fig. 1.1(a)). The emitted ultrasound waves are propagating and interacting to the medium (Fig. 1.1 (b)). Due to the interaction and due to the inhomogeneities that are present within the medium, some reflected and diffused waves will rise. These echoes propagate back towards the transducer, which will translate them in electrical signals (raw channel data) proportional with the received echoes (Fig. 1.1 (c)).

Until here, we presented the basic principle of ultrasound imaging, without taking into account the properties of sound, their propagation laws, the design of the transducers, or aspects about how we can visualize the signals reflected from the medium. Leaving out the details, the next few sections will present the sound and transducer properties, for a better understating of the principle of interaction between the sound and the particles in the propagating medium. For a more thorough covering of the material presented in this section the reader is referred to [(IAEA), 2014].

1.1.2 Sound propagation in medium

We present here the main properties of the sound and the way it interacts with the medium, by emphasizing the phenomena of propagation, reflection, transmission, scattering, absorption, and attenuation.

The tissue is a medium where sounds propagate and where exchange between kinetic and potential energy takes place. In biological tissues and water, we primarily find longitudinal waves. This type of waves is propagated by the tissue particles that are alternatively compressing and decompressing, as illustrated in the Fig. 1.2.

The propagation phenomenon can be described by the wave equation. A wave in homogeneous medium without attenuation, at a position (x, y, z) of the propagating space and at a time t can be described by a second-order differential equation:

$$\nabla^2 p - \frac{1}{c^2}\frac{\partial^2 p(x,y,z,t)}{\partial t^2} = 0, \tag{1.1}$$

where ∇^2 is the Laplacian operator and $\nabla^2 p = \frac{\partial^2}{\partial x^2}p + \frac{\partial^2}{\partial y^2}p + \frac{\partial^2}{\partial z^2}p$ and c is the speed of sound in the medium and has the expression:

$$c = \frac{1}{\sqrt{\kappa\rho}}, \tag{1.2}$$

where ρ is the medium density and $\kappa[\mathrm{Pa}^{-1}]$ the medium compressibility. The average speed of sound in the human body is 1540 m/s. It is slowest in air/gasses and fastest in solids. The values of speed of sound in different biological materials are described in Table 1.1.

The other parameters of the Table 1.1 will be introduced later in the manuscript.

When the wave propagates in one direction, for example x direction, it is referred to as plane wave. In this case, the propagation equation (1.1) become (e.g., [Angelsen, 2000b, Angelsen, 2000a]):

$$\frac{\partial^2 p(x,t)}{\partial x^2} - \frac{1}{c^2}\frac{\partial^2 p(x,t)}{\partial t^2} = 0, \tag{1.3}$$

where $p(x,t)$ represents the pressure that is function of the position x and time t.

One solution of (1.3), important for this work, in the case of plane wave equation given by:

Material	**c(m/s)**	**Z(kg·m^{-2}·sec^{-1}) $\times 10^{-4}$**	**dB/cm at 1 MHz**
Air	330	0.0004	12
Water	1480	1.48	0.0022
Fat	1450-1460	1.34-1.38	0.52
Brain	1560	1.55	0.85
Liver	1555-1570	1.65	0.96
Kidney	1560	1.62	1.0
Spleen	1570	1.64	1.0
Blood	1550-1560	1.61-1.65	0.17
Muscle	1550-1600	1.62-1.71	1.2
Lens of eye	1620	1.85	2.0
Skull bone	3360-4080	6.0-7.8	11.3

Table 1.1: Speed of ultrasound c, specific acoustic impedance Z, and attenuation coefficients μ (at 1-MHz) for some selected materials [(IAEA), 2014].

$$p(x,t) = Ae^{j(\omega t - kx)}, \tag{1.4}$$

where A is the amplitude of the propagating signal, $\frac{\omega}{2\pi}$ is the frequency, and $k = \frac{\omega}{c}$ is the wavenumber. The name of plane wave equation is given by the fact that the wavefronts form planes in the 3-D space. Note that (1.4) is defined for one spatial dimension.

Considering that the plane wave in (1.4) propagates through the medium and is reflected, the measured signal at the sensor is defined as:

$$y(t) = Ae^{j(\omega t - kx)}. \tag{1.5}$$

The acoustic properties of the medium are characterized by the acoustic impedance, which can be seen as the opposition to the flow of sound through a surface. The acoustic impedance, Z, similar to the electric impedance, allows the characterization of a medium based on its density, ρ, and the speed of sound in that medium:

$$Z = \rho c. \tag{1.6}$$

The commonly used unit to quantify the specific acoustic impedance is the rayl, and it is defined as 1[rayl] = 1[kg·m^{-2}·s^{-1}]. The specific acoustic impedance of some selected biological tissues are presented in Table 1.1.

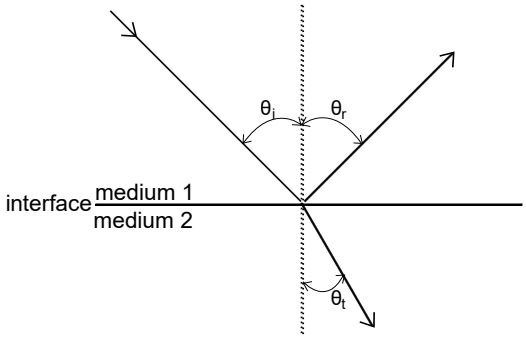

Figure 1.3: Transmission and reflection of an acoustic wave on a planar interface between two media with different acoustic impedances (Z_1 for medium1 and Z_2 for medium2, $Z_1 \neq Z_2$); θ_i - angle of incidence and θ_r - angle of reflection, where $\theta_i = \theta_r$; θ_t-different, because the speed of sound is different in the medium2.

1.1.2.1 Reflection and transmission

During the propagation, sound can travel different types of tissues. In this case, reflection or transmission phenomena may occur which are described in this section.

Through the propagation of the wave in the medium, a portion of the incident energy (I_i) is reflected (I_r), while the second portion is transmitted (I_t), as illustrated in Fig. 1.3. The reflection coefficient α_R is used to measure the reflection between two adjacent tissues with different impedances, Z_1 and Z_2:

$$\alpha_R = \frac{I_r}{I_i} = \frac{(\frac{Z_2}{\cos\theta_t} - \frac{Z_1}{\cos\theta_i})^2}{(\frac{Z_2}{\cos\theta_t} + \frac{Z_1}{\cos\theta_i})^2}. \tag{1.7}$$

The sound wave that is not reflected, will be transmitted into the medium. The transmission coefficient α_T is expressed as:

$$\alpha_T = \frac{I_t}{I_i} = 1 - \alpha_R. \tag{1.8}$$

The equations governing the angles of incidence θ_i, reflection θ_r, and transmission θ_t, are the following:

$$\begin{aligned} \theta_i &= \theta_r, \\ \frac{\sin\theta_i}{\sin\theta_t} &= \frac{c1}{c2}, \end{aligned} \tag{1.9}$$

where $c1$ and $c2$ are the sound velocities in the medium 1, respectively medium 2.

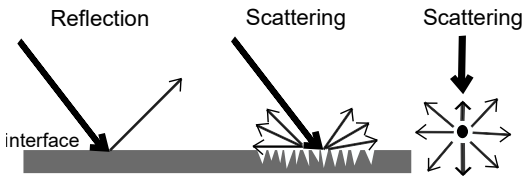

Figure 1.4: The difference between reflection and scattering phenomena.

In the case when $\theta_i = \theta_t = 0$, we can rewrite (1.7) depending just on the ratio between Z_1 and Z_2:

$$\alpha_R = \frac{I_r}{I_i} = \frac{(Z_2 - Z_1)^2}{(Z_2 + Z_1)^2}. \tag{1.10}$$

Considering a soft tissue as interface, by using the values of the specific acoustic impedance in the Table 1.1, it can be shown that the intensity of the reflected ultrasound wave at some interface can reach 0.1% of the incident intensity. The reflection on other types of interfaces (e.g., skull bone) can be higher due to higher specific acoustic impedance.

1.1.2.2 Scattering, absorption, and attenuation

We saw that reflection occurs at flat, smooth interfaces, where the transmitted wave is reflected in a single direction depending on the angle of incidence. However, in biological tissues, the interface is not always perfectly smooth, thus the phenomenon of *scattering* (or diffuse reflection) may occur. Scattering also occurs when the dimension of the target is negligible to the wavelength (e.g., blood cells). The difference between reflection and scattering is illustrated in the Fig. 1.4.

Attenuation represents the loss in energy (intensity) of the propagating ultrasound wave due to scattering and absorption processes. Typically it is approximated by an exponential function of the distance x and it depends linearly on the initial intensity [Angelsen, 2000b]:

$$I(x) = I(0)e^{-\mu x}, \tag{1.11}$$

where μ[dB/cm] is the intensity attenuation coefficient, measured in decibels per centimeter. The attenuation depends on the type of the tissue and is proportional to the frequency f. Table 1.1 contains the values of the attenuation coefficients μ for a

1 MHz ultrasound signal for some selected materials. Low frequency will permit the investigation of deeper located parts of a body, at the price of the degradation of the axial resolution (detailed in the Section 1.2.2) which is inversely proportional to the frequency.

In US imaging system, as echoes are attenuated with the depth, time gain compensation (TGC) is applied to the signal. TGC is used to compensate the effects of absorption. Gain is applied to the signal as function of time (distance).

1.1.2.3 Speckle

Scattering occurs when the dimension of the target is negligible to the wavelength (see Section 1.1.2.2).

The *speckle* pattern is the result of the scattering process of the incident ultrasound wave that propagates through medium's scatterers (see Section 1.1.2.2). The speckle texture appears due to the diffuse reflexion, the resulting waves interacting both through the constructive and destructive interferences.

1.1.3 Transducers

In the Section 1.1.2 we characterized sound and described the phenomena that arise when it propagates through a medium and interacts with it. However, in ultrasonic systems, the transducers are the emitters and receivers of sounds. Thus, in this section we present the main components of a transducer and its properties.

Transducers are the key component of an ultrasound system, being capable of generating and detecting ultrasonic energy. In ultrasound systems, the typical conversions are electrical to ultrasonic energy (in transmission), or ultrasonic to electrical energy (in reception) [Ensminger and Bond, 2011]. In transmission, the transducer can be seen as a loudspeaker, transmitting acoustic pulses which will propagate in the body (Fig. 1.1(a)). In reception, it acts as a microphone, recording the echoes received from the body and converting them into electrical signals (Fig. 1.1(c)). The resulting signals are then beamformed and presented as an ultrasound image. We delay the details of beamforming process and ultrasound image visualization until see Section 1.3, respectively Section 1.2.

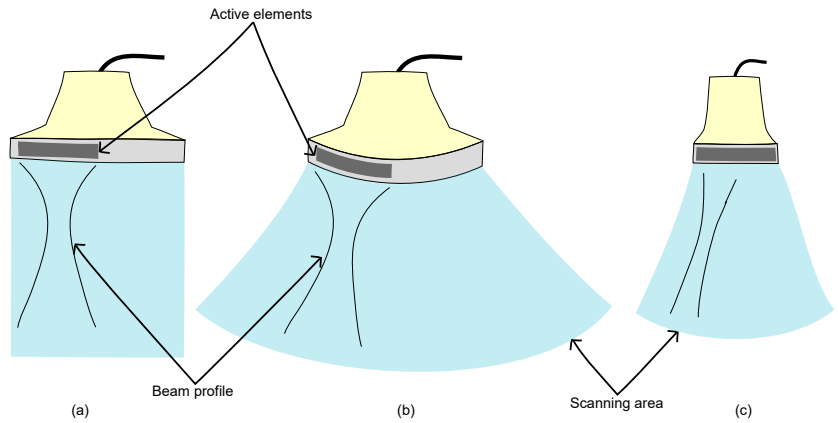

Figure 1.5: Principle of electronic sweeping with (a) linear array, (b) convex array, and (c) phased array.

Transducer can be seen as a piezoelectric sensor. Piezoelectric effects are defined in the *American Institute of Physics Handbook* [Dwight E. Gray, 1957] as "the phenomena of separation of charge in a crystal by mechanical stresses and the converse". Transducers are usually composed as arrays of small piezoelectric crystals. The array configuration plays a major role in the dynamic focusing and in the electronic beamforming. However, the topics of focusing and beamforming are very challenging and we discuss them in Section 1.3.

However, before describing beamforming, it is important to present the main configurations of the transducer array, how their configuration can influence the scanned region of interest, and the main medical applications of each configuration. In the next section we touch upon these topics.

1.1.4 Scanning

The first ultrasound probes were composed of a single piezoelectric crystal and the images were formed by mechanically rotating or translating the probe. Nowadays, the probes includes a large number (ranging between 64 to 512) of piezoelectric crystals. Instead of using mechanical rotation or translation, electronic sweeping or steering is used. Exciting few adjacent crystals by an electric pulse, will produce an ultrasound beam. In the classical scanning process, the echoes reflected by the scanning medium will be received by the same number of crystals. We will touch upon the topic of the number of the elements used in the transmission or reception in Section 1.1.5.

Typically, the ultrasound transducers can be found in three main configurations: linear, convex, or phased arrays. Fig. 1.5 illustrates the three configurations and the electronic sweeping for each case. In general, the convex and phased array configurations are also named sector arrays, since they will provide sector scans. Linear arrays will provide rectangular scans.

Rectangular scans (images) are obtained by using linear transducers that have the piezoelectric crystals arranged in a line (Fig. 1.5(a)). One reflected pulse results from each different subaperture composed of a number of active elements of the transducer. This subaperture is shifted over a region of interest in the body. The shape of the field of view (FOV) is rectangular, so the resulted 2D images are also rectangular. Such a probe can be used, for example, for investigation of shallow objects (e.g., carotid arteries, thyroid, or cysts in the liver).

Sector scans are produced using convex or phased arrays. Generally, it uses 100-200 beams that are steered (mechanically or electronically) with different angles. The angles are defined by delaying the signals transmitted by each element. The FOV is enlarged due to their capability of producing a fan-shaped field of view.

By using *convex arrays*, the piezoelectric crystals are arranged on a convex surface. Thus, a larger area than the one obtained using linear arrays can be scanned (Fig. 1.5(b)). The principle of shifting the active transducer's subaperture over the probe is the same as for linear array. This type of configuration is generally used for heart and abdomen investigations.

Phased arrays permit reducing the number of elements of transducer, while obtaining a large FOV (Fig. 1.5(c)). All the probe's elements are used in transmission and reception. To control the direction of the beam, the emitted (and/or received) signals are delayed.

The 3D scanning can be obtained either by using piezoelectric elements arranged in a rectangular grid form, or by mechanically moving a 2D US probe. This configuration allows the steering of the ultrasound beam in two directions, creating a 3D FOV.

1.1.5 Imaging modalities

In Section 1.1.4 we discussed about the common configurations of the elements of an transducer: linear, convex, or phased arrays. Moreover, Fig. 1.5 illustrates that in the case of linear and convex arrays, just some elements of the probe are used in transmission

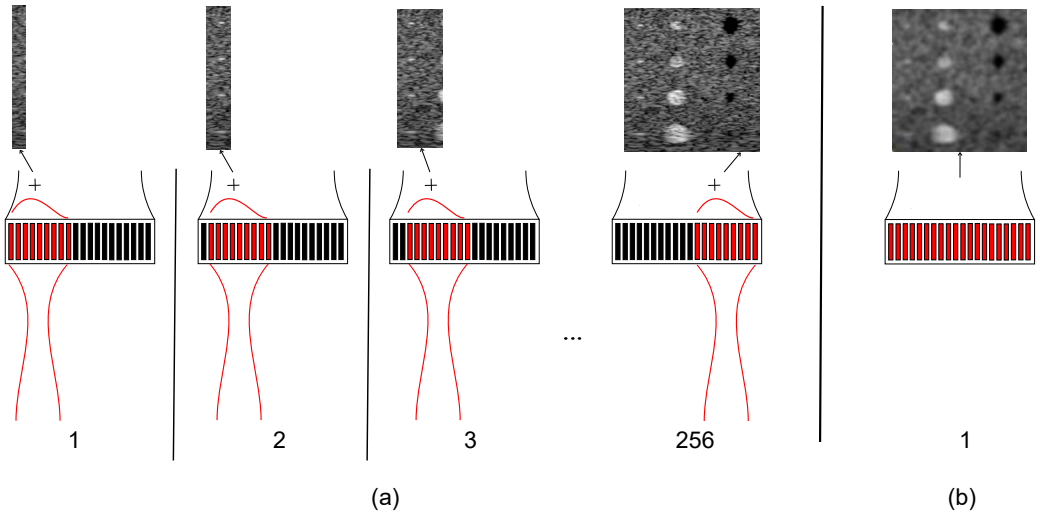

Figure 1.6: Ultrasound imaging modalities: (a) conventional and (b) plane-wave imaging.

or reception. In fact, we will see in this section that Fig. 1.5(a)-(b) illustrate the standard scanning modality. Besides the standard modality, we introduce plane-wave imaging modality which is of great interest for applications involving high frame rates. Both modalities are presented next in this section.

Fig. 1.6 presents the two aforementioned imaging modalities in ultrasound imaging. The *standard US imaging* Fig. 1.6(a) sequentially scans the medium using focused beams. Each focus beam will allow the reconstruction of one image line. A typical 2D US image contains multiple lines (64 to 512). The *frame rate* of the imaging depends on the time required to transmit, receive and process the reflected echoes (beamforming process). At maximum depth, d_p, the pulse repetition interval, T_R is:

$$T_R \geq \frac{2d_p}{c}. \tag{1.12}$$

Thus, the pulse repetition rate, f_R is:

$$f_R = \frac{1}{T_R}. \tag{1.13}$$

If K emissions are required to form an US image, the image frame rate is calculated as:

$$F = \frac{1}{KT_R}. \tag{1.14}$$

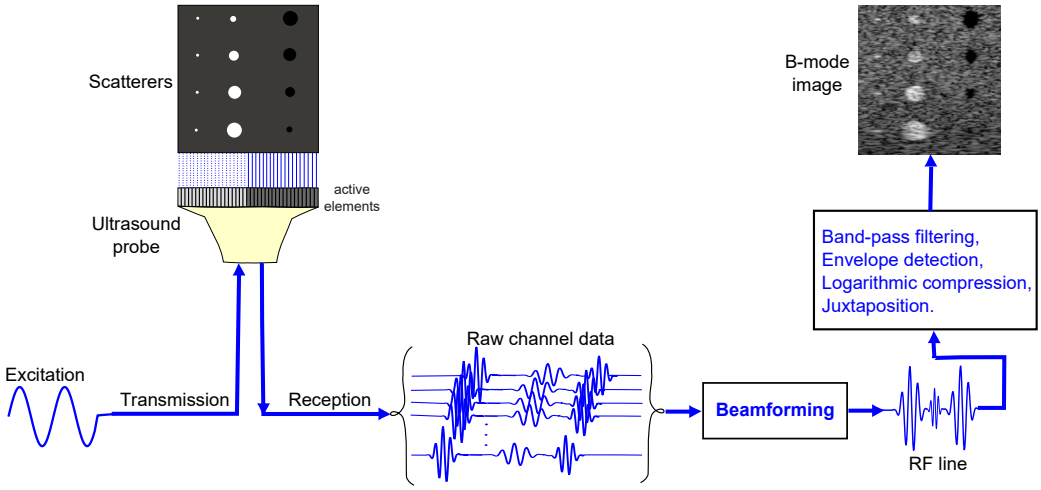

Figure 1.7: General ultrasound scanning process.

Some applications require higher frame rates (for example, the echography, for heart motion analysis). To increase the frame rate and decrease acquisition time, *plane-wave* imaging can be a great solution. Plane-wave imaging uses all the elements in transmission/reception to construct an US image. Of course, this image have lower resolution than the one obtained in standard US imaging Fig. 1.6(b). However, the resolution of the image can be increased by compounding, by using several steered emissions (e.g., [Zhao et al., 2015a]). More details about the resolution of ultrasound imaging and the main used image quality metrics of US imaging are discussed in Section 1.2.2, respectively Section 1.2.3.

1.2 Ultrasound image visualization

Before we discuss about the US imaging quality and the common metrics used to measure the resolution and the contrast of an US image, it is important to understand the techniques of US image visualization.

In Section 1.1 we presented the principle of US imaging, from the excitation of the transducer, through the interaction between the acoustic waves with the particles in the medium, until the formation of the raw channel data (see Fig. 1.1). The entire scanning process, after the reception of the raw channel data by the transducer, is illustrated in the Fig. 1.7. Thus, BF techniques are applied to raw channel data to form the

radiofrequency (RF) data. Since the topic of BF is the main attraction of this work, we delay the details about BF techniques until Section 1.3, where the main BF categories are presented. In this way, we will continue the discussions from Section 1.3 to Chapter 2, where we present the main BF techniques applied to medical US. However, before describing BF, we shall discuss about how ultrasound imaging is visualized.

After receiving the echoes (raw channel data) reflected by the tissues (medium) using the principle described in Fig. 1.1, BF in reception is applied in order to improve the spatial resolution, the signal-to-noise ratio, and the contrast of the images. The US images that result after the BF process, are called RF images, and are the result of juxtaposing multiple RF signals. For visualization reasons, the RF images are then converted into B (brightness) mode images, using conventional post-processing techniques such as band-pass filtering, envelope detection, logarithmic compression, and scan conversion. These techniques will be briefly described in the following paragraphs.

Let us denote with $\boldsymbol{s}_i(n)$ the RF signal formed after beamforming the raw channel data corresponding to the emission i, $n = 1, \cdots N$, where N is the length of the signal recorded over time at a sampling rate f_s. The reconstruction of the B-mode image starting from the RF signals (signals obtained after the beamforming process) is described in Fig. 1.8.

1.2.1 Image visualization modes

As stated in Section 1.1.4, the first US probes were composed of a single piezoelectric crystal, acting as both a transmitter and a receiver. Thus, a single signal could be recorded at a particular time instance and was displayed as time series, corresponding to a one-dimensional scan. This type of visualization is called *amplitude mode* (A-mode) imaging.

The most common type of imaging is the *brightness mode* (B-mode), illustrated in the Fig. 1.8. The image points are displayed in an rectangular grid, in gray scale with brightness proportional with the amplitude of the reflections.

The newest technology is the three-dimensional (3D) imagining, that uses two-dimensional (2D) transducer arrays.

Other US imaging modes can be also found: *motion mode* (M-mode) displays the echoes from one scan line over time; *colorflow* presents the velocities of the blood flow;

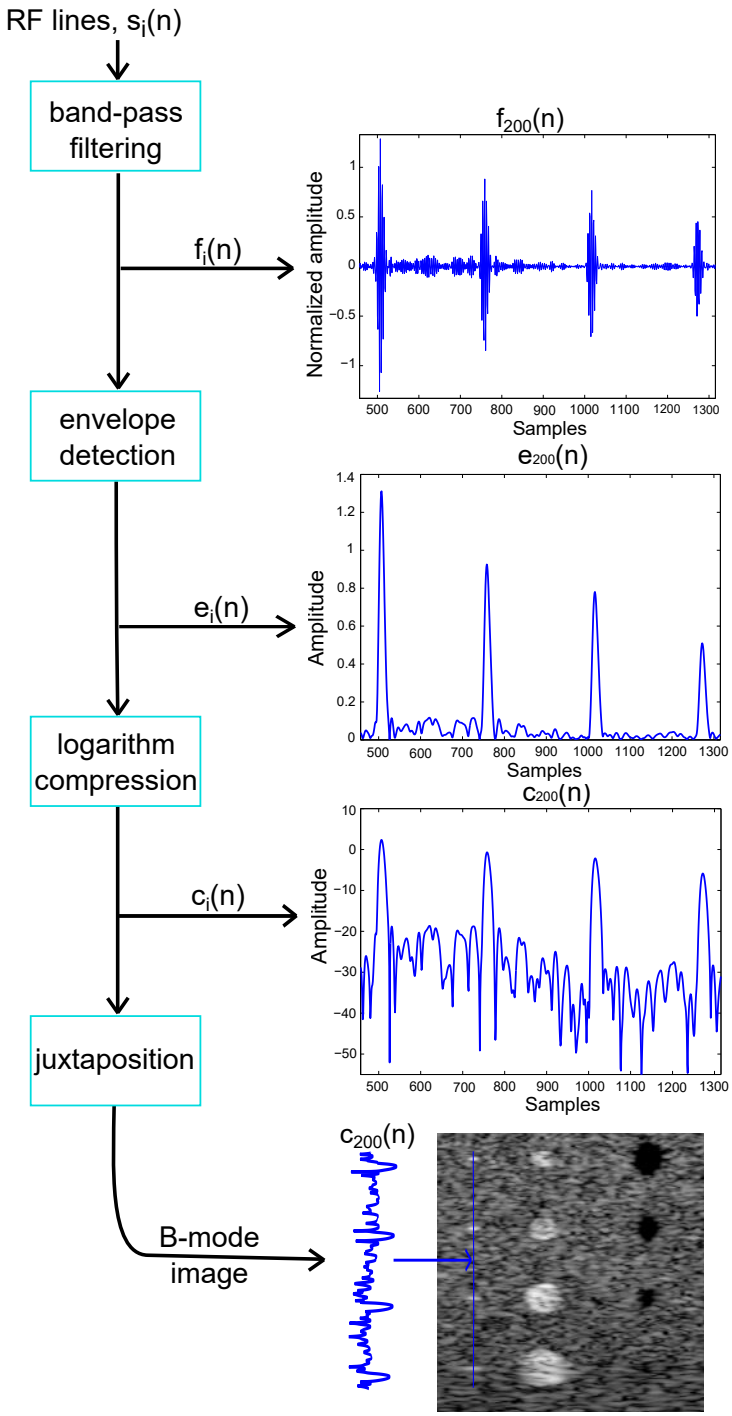

Figure 1.8: Reconstruction of B-mode image from RF signals. Intermediate data is illustrated in the right side of the figure.

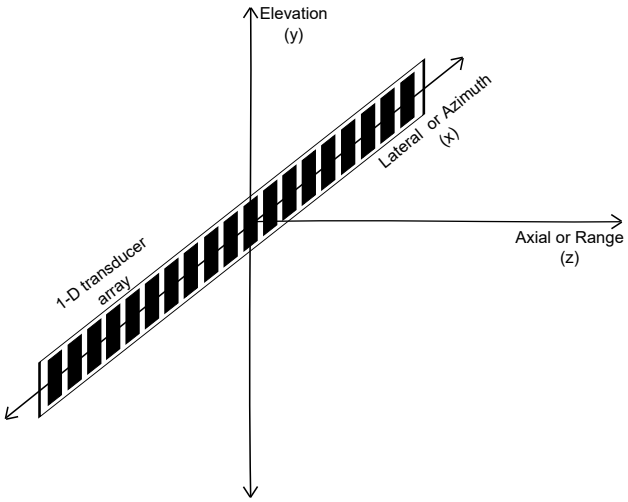

Figure 1.9: The spatial coordinate system for illustrating the axial and lateral resolution configuration of an 1-D ultrasound transducer array. The transducer is divided into elements in the lateral direction. The transmitted US wave propagates in the axial direction.

harmonic imaging shows the image harmonics generated by non-linear propagation. These and other imaging techniques are detailed in e.g., [Merton, 1997, Jensen, 2007].

1.2.2 Image resolution

Ultrasound image quality is strongly influenced by the spatial resolution (both axial and lateral resolution). Fig. 1.9 illustrates the spatial coordinate system for describing spatial resolution of an 1-D ultrasound transducer.

Axial resolution is the capability to distinguish between two structures lying in the direction of the propagation of the ultrasound beam. Axial resolution depends on the speed of sound, c, and the bandwidth of the ultrasound probe, B, [Foster et al., 2000]:

$$r_{ax} = \frac{2c}{B}. \tag{1.15}$$

Usually, for central frequencies of $3-3.5$ MHz, the axial resolution is about 0.2 mm.

Lateral resolution is the ability to distinguish between two structures lying in the lateral direction. Lateral resolution depends directly on wavelength,λ, and focal distance, L_f, and it depends inverse directly on the diameter of the ultrasound probe, D, [Foster et al., 2000]:

$$r_{lat} = \lambda \frac{L_f}{D}, \tag{1.16}$$

Thus, thinner the beam, better the lateral resolution. It also depends on the geometry of the transducer, the frequency, and the focal point. Beamforming (i.e., DAS BF, see Fig. 2.3) can be used to focus the ultrasound beam in order to obtain the optimal resolution in the region of interest. Moreover, dynamic focusing allows the focus of the beam on multiple points along a given direction.

1.2.3 Image quality metrics

We conclude the part of this section devoted to US image visualization by describing the most common US image quality metrics that are used in this dissertation to compare between the results proposed and existing BF techniques. In this work, they were computed based on the envelope-detected signals independent of image display range. Based on two regions R_1 and R_2 belonging to two different structures, the contrast ratio (CR) is defined as e.g., [Xu et al., 2014a]:

$$CR = |\mu_{R_1} - \mu_{R_2}|, \tag{1.17}$$

where μ_{R_1} and μ_{R_2} are the mean values in the region R_1, respectively R_2.

The contrast-to-noise ratio (CNR) is defined as e.g., [Rindal et al., 2014]:

$$CNR = \frac{|\mu_{R_1} - \mu_{R_2}|}{\sqrt{\sigma_{R_1}^2 + \sigma_{R_2}^2}}, \tag{1.18}$$

where σ_{R_1} and σ_{R_2} are the standard deviations of intensities in R_1, respectively R_2.

Basically, CNR and CR compare a region of interest (ROI) to the level of the background. The greater the CR and CNR, the more perceptible the structure in the medium and better the contrast of US images.

The signal-to-noise ratio (SNR) is defined as the ratio between the mean value μ and the standard deviation σ in homogeneous regions e.g., [Jensen and Austeng, 2014]:

$$SNR = \frac{\mu}{\sigma}. \tag{1.19}$$

Higher levels of SNR indicate grater useful information compared to noise. Thus, in US imaging, grater values of SNR are preferable.

The resolution gain (RG) is defined in [Taxt and Strand, 2001] as the ratio between the normalized autocorrelation function with values higher than 3 dB (computed for the DAS beamformed image in our case), over the normalized autocorrelation function (higher than 3 dB) of the images formed by using the other BF methods. Note that a value of RG > 1 needs to be achieved for achieving a better resolution than classical beamformers.

1.3 Introduction to beamforming

A general discussion about beamforming (BF) in US imaging is described in this section. Then, we describe it in more detail in Chapter 2, where we present the state of the art of the BF techniques used in medical US imaging.

The beamformer (or spatial filter) [Van Veen and Buckley, 1988] is the ultrasound system's "engine", being the main component responsible for image formation. Its benefit is twofold:

- Steer or focus the ultrasound transducer towards a signal coming from a specific point, usually called focal point.
- Improve the contrast, spatial resolution and the signal-to-noise ratio of the ultrasound image.

BF enables the selectivity of acoustic signals reflected from some known positions, while attenuating the signals from other positions. This is classically done by delaying (focusing) and applying some specific weights to the reflected signals. All these concepts and examples of beamformers will be presented in the Chapter 2.

2

Beamforming in medical ultrasound imaging: State of the art

Contents

In this chapter we describe the standard beamforming method (data-independent), which consist in focusing (delaying) and weighting the raw channel data before averaging them. Then, we present the adaptive beamformers and their main issues. Finally, we briefly describe how beamforming could be modelled in other domains.

2.1 Focusing

One of the first major steps in beamforming is focusing. In transmission, delays are applied to control the contributions coming from all transducer's elements to hit a given point, called focal point in emission. In reception, the echoes received by the elements (raw channel data) are delayed such that they sum contributions coming from the same given point of the medium (focal point in reception).

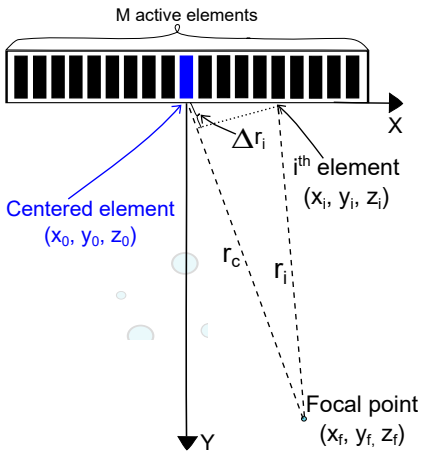

Figure 2.1: Spatial 2D configuration. The US probe contains M active elements with the central element is illustrated in blue. The distance from the i-th element to the focal point is r_i. The distance from the central element to the focal point is r_c. The delay that is applied to the signal emitted by the i-th element is Δr_i. In (2.4), the pressure denoted $p_0(x, y, z, t)$ refers to the one corresponding to the central element, highlighted by blue.

To calculate the delays, the ray acoustics theory can be used [Jensen, 1999]. Fig. 2.1 describes the main elements used in the calculation of the delay, Δr_i in order to hit the i-th element to focal point. The distance from the i-th element to the point of interest, $S(x, y)$, is:

$$r_i = \sqrt{(x_i - x_f)^2 + (y_i - y_f)^2 + (z_i - z_f)^2}, \tag{2.1}$$

where (x_i, y_i, z_i) is the center of the i-th element and (x_f, y_f, z_f) is the position of the focal point. The central element of the transducer is situated at the position (x_0, y_0, z_0), and its distance to the focal point, r_c, is expressed as:

$$r_c = \sqrt{(x_0 - x_f)^2 + (y_0 - y_f)^2 + (z_0 - z_f)^2}. \tag{2.2}$$

Thus from (2.1) and (2.2), the delay needed to be applied to the i-th element in order to compensate the time of flight is equal to:

$$\Delta t_i = \frac{1}{c}\Delta r_i = \frac{1}{c}(r_c - r_i), \tag{2.3}$$

where c is the speed of sound in the medium. Thus, the selection of each focal point can be done using the delays expressed in (2.3), but under the assumption of constant c.

2.2 Main ultrasound imaging elements

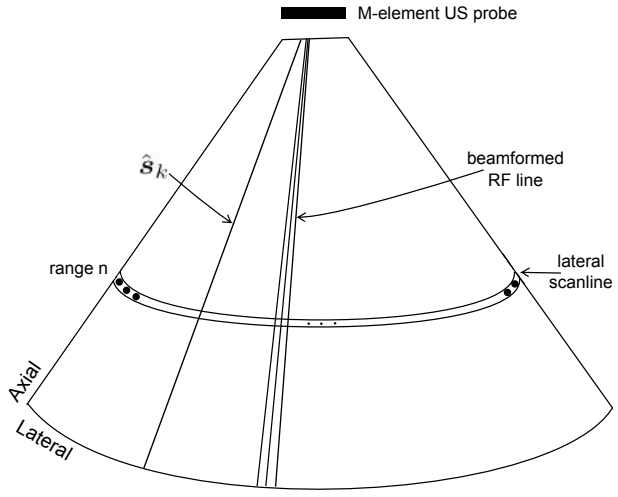

Figure 2.2: The main US imaging elements to model beamforming.

Fig. 2.2 presents the main elements used to model the beamforming process. We will extensively use this elements to mathematically describe the different BF methods presented in this dissertation.

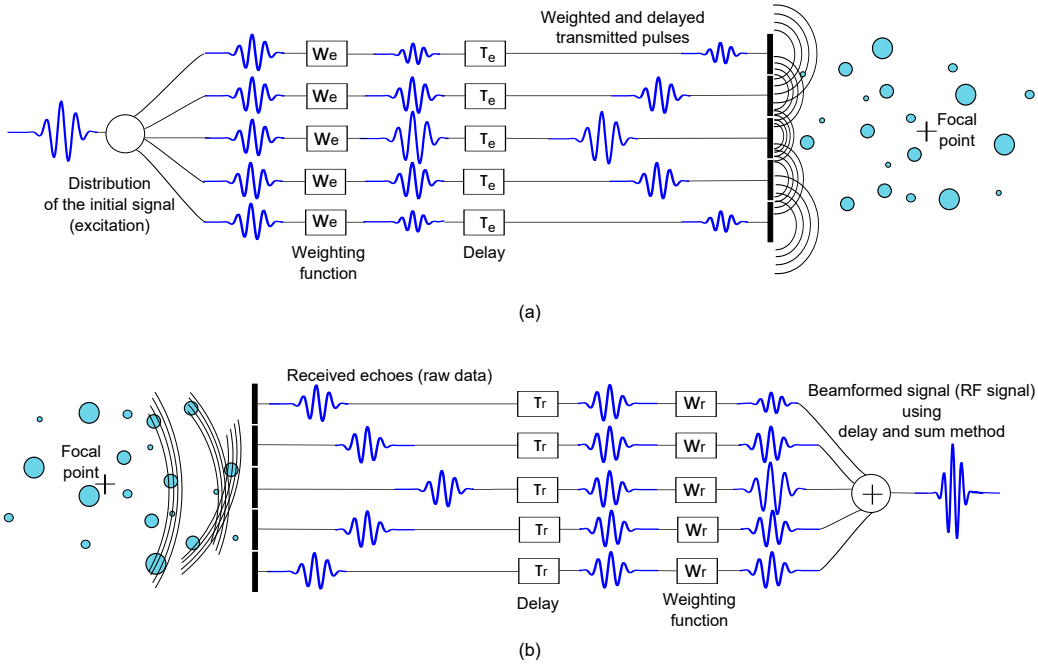

Figure 2.3: Principle of delay-and-sum (DAS) beamformer for (a) emit and (b) receive.

We consider, without loss of generality, the particular setup of an M-element US probe (M can be also the number of the active elements of the probe). A series of K focused beams are transmitted with different incident angles $\theta_k, k = 1, \cdots, K$. The returning echoes are recorded using the same US probe, being time-delayed, such that the time-of-flight is compensated, so that the backscatter from the point of interest is summed up coherently. If we consider that each of the recorded raw signal after the time-delay compensation has N time samples, the size of the recorded data from all the K directions will be $M \times N \times K$.

2.3 Data-independent beamforming: DAS

After focusing the raw data, different weights are applied to the focused data. Depending on the calculation of the weights applied to the output array of the reflected signals, beamformers can be either data-independent (fixed), or data-dependent (adaptive). We present hereafter the most common data-independent beamforming method, called delay-and-sum (DAS), see for e.g., [Thomenius, 1996].

The principle of DAS BF is illustrated in the Fig. 2.3 for both emit and receive.

In emission, (Fig. 2.3(a)), both the amplitude (through weighting) and the time of excitation (through delays) are controlled at each transducer's element, such that the weighted and delayed transmitted pulses add up constructively in the focal point. The expression of the pressure field is:

$$P(x, y, z, t) = \sum_{i=1}^{M} w_i p_0(x - x_i, y - y_i, z - z_i, t - \Delta t_i), \tag{2.4}$$

where (x, y, z) represents the spatial location, t represents the time, M is the total number of elements, w_i is the weight of the i-th element, centered at the position x_i, y_i, and z_i, Δt_i is the time delay applied to the signal that excited the i-th element, and p_0 is the pressure field generated by one element with center at the origin of the coordinate system. Because all the elements of the US probe are identical, each of the element can be expressed as function of the centered element's pressure (the central element is highlighted in blue in Fig. 2.1).

In reception, (Fig. 2.3(b)), the echoes received by the elements of US probe, also called raw channel data, are focused (delayed) in order to compensate the delays due to the time-of-flight differences. Then, the resulting signals are weighted (using a weighting function, also called apodization function) and further summed up to form one RF signal. The applied weights form the apodization window in reception.

Beamforming is more flexible in reception than in emission. In emission, once the elements have been excited, we cannot control anymore the process of beamforming. However, in receive, the raw channel data can be stored and the weighting functions can be selected function of the recorded data, according to the depth.

To mathematically model DAS BF, we consider hereafter the classical acquisition scheme presented in the Section 2.2, where a series of K focused beams is transmitted with M elements (Fig. 2.2). The final RF US image is a collection of RF beamformed lines, each of which being the result of beamforming the raw RF signals coming from an emission in the direction θ_k, $k \in \{1, \ldots, K\}$, using M elements of the transducer. The classical DAS BF can be expressed as:

$$\begin{aligned} \hat{\boldsymbol{s}}_k(n) = \boldsymbol{w}^H(n)\boldsymbol{y}_d^{(k)}(n) = \sum_{m=1}^{M} w_m(n)\boldsymbol{y}_m^{(k)}(n - \Delta_m(n)) \\ n = 1, \cdots, N, \quad k = 1, \cdots, K, \end{aligned} \tag{2.5}$$

where $\Delta_m(n)$ is the time delay for focusing at the point of interest sample, being dependent on the distance between the m-th element and the point of interest, w_m are the BF weights, $\boldsymbol{y}_m^{(k)} \in \mathbb{C}^{N\times 1}$ is the raw channel data received by the m-th element of the US probe, corresponding to the emission steered at angle θ_k, and $(\cdot)^H$ represents the conjugate transpose. Note that where $\boldsymbol{y}_d^{(k)} \in \mathbb{C}^{M\times N}$ is the time-compensated version of $\boldsymbol{y}_m^{(k)}$. A simplified form of (2.5) can be formulated as:

$$\hat{\boldsymbol{s}}_k = \boldsymbol{w}^H \boldsymbol{y}_k, \tag{2.6}$$

where $\boldsymbol{y}_k \in \mathbb{C}^{M\times N}$ is the time-compensated version of $\boldsymbol{y}_m^{(k)}$ in (2.5) for the k-th emission (for the sake of generality, we consider $\boldsymbol{y}_k$ to be complex-valued data), and $\boldsymbol{w}$ is the vector of the beamformer weights of size $M \times 1$.

DAS BF selects the weights independent on data, solving:

$$\min_{\boldsymbol{w}} \boldsymbol{w}^H \boldsymbol{w}, \quad \text{such that} \quad \boldsymbol{w}^H \mathbf{1} = 1, \tag{2.7}$$

where $\mathbf{1}$ is a length M column-vector of ones since the raw channel data was focused using time-delays. The solution of (2.7) is:

$$\boldsymbol{w}_{DAS} = \frac{\mathbf{1}}{M}. \tag{2.8}$$

If we replace (2.8) in (2.6) we get:

$$\hat{\boldsymbol{s}}_k = \frac{1}{M}\mathbf{1}^T \boldsymbol{y}_k, \tag{2.9}$$

where $\{\cdot\}^T$ denotes the transpose. A common technique used in US is to apply weighting functions such as Hanning, or Hamming apodizations to (2.9) to further reduce the sidelobes of $\hat{\boldsymbol{s}}_k$, resulting in improved contrast of the beamformed image, at the cost of a slight lateral spatial resolution degradation.

2.4 Data-dependent beamforming

The fact of beamforming dependently on the raw channel data is called adaptive beamforming. Adaptive beamformers calculate the weights from the statistics of the received data in order to converge to an optimal response in terms of maximization of the SNR at the beamformer output. Thus, the contributions of the noise and the signals that arrive from other directions than the desired one are minimized.

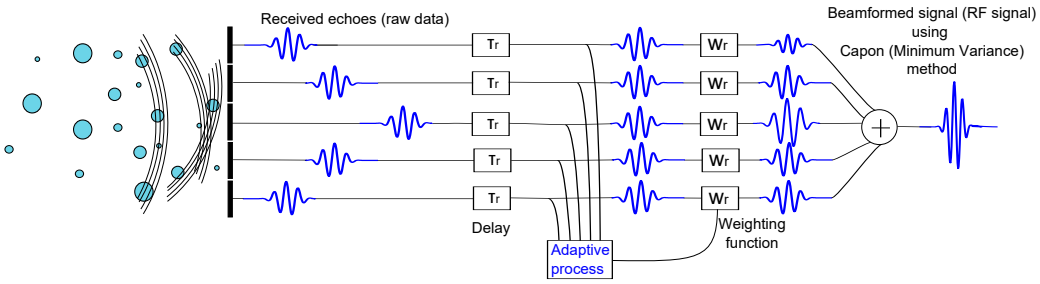

Figure 2.4: Principle of Capon (Minimum Variance) beamforming in reception.

The main challenge in applying adaptive BF to medical ultrasound imaging is the *correlation* between the signal and the interference. The signal and the interference are highly correlated, due to the fact that the US probe is receiving echoes reflected by the same region of interest. There are different techniques to deal with correlation, that will be discussed in the next sections.

2.4.1 Capon or minimum variance beamformer

The classic DAS beamforming (Fig. 2.3) has the weights independent of the transmitted pulses (in emission) or raw channel data (in reception).

In reception, the idea of adaptive beamforming is to use the received echoes (raw channel data) to calculate the weights. One of the most widely used methods is Capon filter, also called Minimum Variance (MV) [Capon, 1969]. While the DAS beamformer uses fixed data-independent weights, $\mathbf{w}$, the aim of MV is to apply an optimal set of weights in order to estimate the desired signal waveform as accurately as possible, while rejecting the interfering signals. Fig. 2.4 illustrates the beamforming process when MV method is used. The optimal weights in the sense of MV, can be obtained from the expression of the signal-to-interference-plus-noise ratio ($SINR$) [Li and Stoica, 2006]:

$$SINR = \frac{\sigma_s^2 |\boldsymbol{w}^H \boldsymbol{a}|^2}{\boldsymbol{w}^H \boldsymbol{R}_k \boldsymbol{w}}, \tag{2.10}$$

where $\boldsymbol{R}$ of size $M \times M$ is the interference-plus-noise covariance matrix, σ_s^2 is the signal power and $\boldsymbol{a}$ the steering vector. To have a maximum $SINR$, the output interference-plus-noise power is minimized, while maintaining a distortionless response to the desired signal:

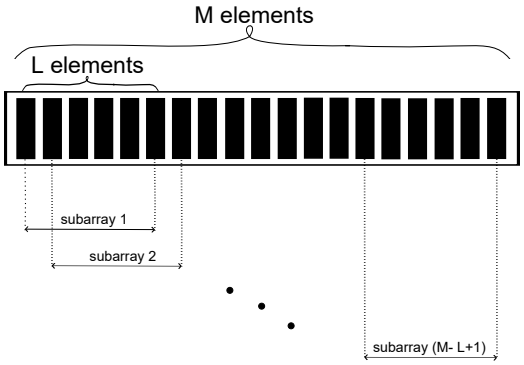

Figure 2.5: Subbarray division. The M elements of the array are divided into overlapping subarrays of length L. Then, the spatial covariance matrices of the $M - L + 1$ subarrays are averaged.

$$\min_{\boldsymbol{w}} \boldsymbol{w}^H \boldsymbol{R}_k \boldsymbol{w}, \text{ such that } \boldsymbol{w}^H \mathbf{1} = 1. \tag{2.11}$$

Therefore, the solution of (2.11), also called the minimum variance distortionless response beamformer, is:

$$\boldsymbol{w}_{MV} = \frac{\boldsymbol{R}_k^{-1}\mathbf{1}}{\mathbf{1}^T \boldsymbol{R}_k^{-1}\mathbf{1}}. \tag{2.12}$$

As in practical situation the analytical form of $\boldsymbol{R}_k$ is not known, it is usually replaced by the estimated covariance matrix derived from P received samples (snapshots), denoted by $\hat{\boldsymbol{R}}_k$:

$$\hat{\boldsymbol{R}}_k = \frac{1}{P}\sum_{p=1}^{P} \boldsymbol{y}_k(p)\boldsymbol{y}_k^H(p). \tag{2.13}$$

In order to decorrelate the coherent signals received from the M elements, the *subarray-averaging* (spatial averaging) method is generally used (see Fig. 2.5). Specifically, the linear array of M elements is divided into $M-L+1$ overlapping subarrays of size L, and the covariance matrices from all subarrays are averaged [Synnevag et al., 2007a]. Usually, a value of $L \leq \frac{M}{2}$ will ensure that the covariance matrix is invertible. However, it was shown that when using subarray-averaging technique, the tissue may appear less homogeneous and may give different statistics compared with DAS [Synnevag et al., 2007b]. To retain the speckle statistics, the temporal averaging (corresponding to depth) was introduced in [Synnevag et al., 2009]. The authors of [Synnevag et al., 2009] suggested

a *temporal averaging* over $2T+1$ time samples. By applying both spatial and temporal averaging, the equation of the estimated covariance matrix becomes:

$$\tilde{\boldsymbol{R}}_k(t) = \frac{1}{(2T+1)(M-L+1)} \sum_{t=-T}^{T} \sum_{l=1}^{M-L+1} \boldsymbol{y}_k^{(l)}(t) \boldsymbol{y}_k^{(l)}(t)^H, \tag{2.14}$$

where $\boldsymbol{y}_k^{(l)}$ is the dynamically focused raw channel data corresponding to the l-th subarray of size L.

By averaging both in the spatial (lateral direction) and temporal (axial direction) domains, the resolution can be further improved, with no contrast degradation. The adaptive weights are calculated by replacing $\tilde{\boldsymbol{R}}_k$ in (2.12). These weights will be then used in (2.6) in order to obtain the RF signals after MV beamforming. Thus, the RF signals of the MV beamformer can be expressed as:

$$\tilde{\boldsymbol{s}}_k = \boldsymbol{w}_{MV}^H \boldsymbol{y}_k, \tag{2.15}$$

Note that the constraint in (2.11) assures that only the waves reflected from the focal point are passed with unit gain, the others being suppressed. However, phase aberrations may occur, resulting in targets that may appear out of the focus. These reflections will be minimized by using a robust MV beamformer. To increase the robustness of MV beamforming, different techniques exist in the literature, that are able to constrain the level of supression outside the focal point. In Section 2.4.2 we discuss and compare the most common approaches.

2.4.2 Improved MV beamformer approaches

In the next sections we discuss three of the most common techniques to improve the robustness of the MV beamformer: diagonal loading, coherence factor, and the use of frequency subbands.

2.4.2.1 Diagonal loading

One way to increase the robustness of MV beamformer is to apply the *diagonal loading* (DL) technique before the inversion of the estimated covariance matrix in 2.11 [Synnevag et al., 2007a]. This technique consists in adding a constant, ϵ, to the estimated covariance matrix, such that $\tilde{\boldsymbol{R}}_k$ becomes $\tilde{\boldsymbol{R}}_k + \epsilon \boldsymbol{I}$, where $\boldsymbol{I}$ is the identity matrix. There exist different methods to compute the value of ϵ (see more details in

[Li et al., 2003]), but the most common way is to fix ϵ to be proportional to the power of the received signals:

$$\epsilon = \Delta \cdot \text{tr}\{\tilde{\boldsymbol{R}}_k\}\boldsymbol{I}, \tag{2.16}$$

where Δ is a constant and $\text{tr}\{\cdot\}$ is the trace operator. In [Synnevag et al., 2007a] a robust solution is obtained when $\Delta = \frac{1}{L}$. Thus, by replacing (2.16) in (2.12), the expression of the weights when diagonal loading technique and temporal and spatial averaging are applied, becomes:

$$\boldsymbol{w}_{MV}^{(DL)} = \frac{(\tilde{\boldsymbol{R}}_k + \frac{\Delta}{L}\text{tr}\{\tilde{\boldsymbol{R}}_k\}\boldsymbol{I})^{-1}\mathbf{1}}{\mathbf{1}^T(\tilde{\boldsymbol{R}}_k + \frac{\Delta}{L}\text{tr}\{\tilde{\boldsymbol{R}}_k\}\boldsymbol{I})^{-1}\mathbf{1}}. \tag{2.17}$$

In order to obtain the RF signals, the weights obtained in the (2.17) are replaced in (2.15).

2.4.2.2 Coherence factor weighting

In [Asl and Mahloojifar, 2012, Asl and Mahloojifar, 2009], the robustness of the MV beamformer was increased by combining it with the *coherence factor* (CF) weighting. However, CF weighting can also be applied as extension to DAS beamforming, increasing the resolution and the contrast of the resulted image compared with DAS. It was shown that the resolution and the contrast of the final image are improved. The CF technique is used as an extension to MV, being based on the spatial spectrum of the aperture data. Basically, it represents the ratio of the mainlobe energy to the total energy and it is used as an index of the focusing quality [Li and Li, 2003], being referred also as the Mallart-Fink focusing factor [Mallart and Fink, 1994] (2.18). Even if the resolution and the contrast of the images are improved, [Xu et al., 2014b] showed that the resulting images may be altered due to the low SNR and SINR. Thus, they proposed the spatio-temporally smoothed coherence factor (StS-CF), which is a variant of the CF applied on raw channel data that was previously divided in subarrays in the lateral direction, as shown in the Fig. 2.5, and temporally divided. In this way, the artifacts stemming from low SNR and SINR are attenuated. The equation of the spatio-temporally smoothed CF is written as:

$$\boldsymbol{CF} = \frac{|\sum_{m=1}^{M}\boldsymbol{y}_k(m)|^2}{M\sum_{m=1}^{M}|\boldsymbol{y}_k(m)|^2}. \tag{2.18}$$

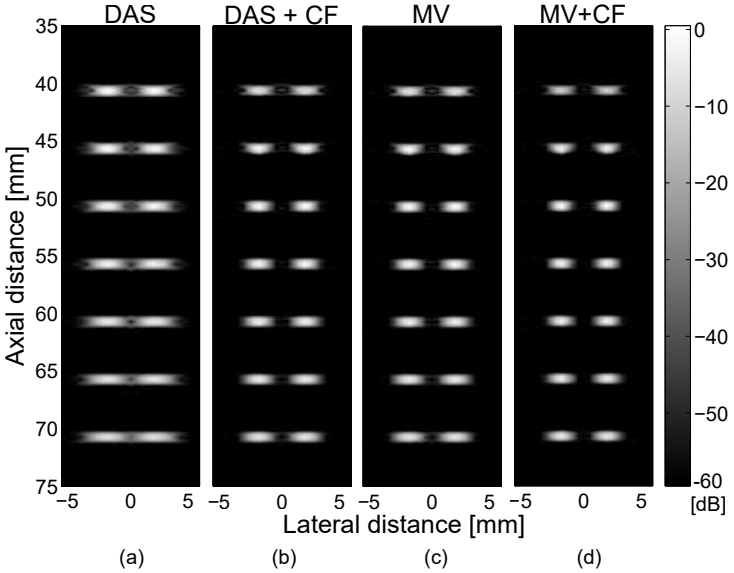

Figure 2.6: Comparison between (a) DAS, (b) DAS+CF, (c) MV, and (d) MV+CF. For simulations, an US probe of $M = 64$ active elements was used. Subarray-averaging method was applied to MV with subarrays of size $L = 32$. In this case, no temporal averaging was used, so $K = 0$.

Thus, (2.15) can be re-written as follows after applying CF weighting:

$$\tilde{\boldsymbol{s}}_k^{(CF)} = \frac{\boldsymbol{CF}}{M - L + 1} \boldsymbol{w}_{MV}^H \boldsymbol{y}_k. \tag{2.19}$$

Fig. 2.6 shows the comparison between DAS BF (Fig. 2.6(a)) and MV BF (Fig. 2.6(c)) and the effect of applying the CF weighting for both DAS BF (Fig. 2.6(b)) and MV BF (Fig. 2.6(d)). We can observe that the best result is obtained when MV with CF weighting is used (Fig. 2.6(d)). Note that the aforementioned BF methods were tested on a simulated medium that contains 14 punctual scatterers, laterally aligned in pairs of two, at lateral positions of -2 mm and 2 mm. The BF methods used in this example were implemented by the author of the dissertation. The simulated medium was obtained using the Field II simulation program [Jensen and Svendsen, 1992].

Fig. 2.7 illustrated the lateral profiles at depth 50 mm (Fig. 2.7(a)) and depth 70 mm (Fig. 2.7(b)) corresponding to the Fig. 2.6. We can observe that the narrower mainlobes are obtained by using MV with CF weighting.

Note that other solutions exist in the literature to improve the classical CF weighting. For example,[Nilsen and Holm, 2010] addressed CF weighting using Wiener postfilter

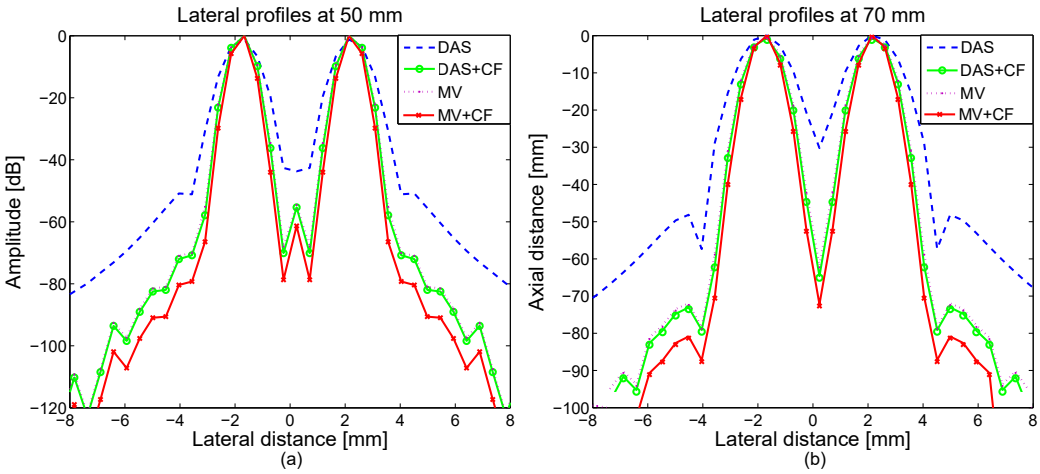

Figure 2.7: Comparison of the lateral profiles at (a) 50 mm and 70 mm from Fig. 2.6.

for DAS beamforming. Hovewer, was shown in [Xu et al., 2014b] that StS-CF provides better results in terms of contrast, resolution, and robustness to low SINR.

2.4.2.3 Frequency subbands

Another approach to improve the robustness of the MV beamformer was proposed by Holfort *et al.* in [Holfort et al., 2009]. Using the discrete Fourier transform (DFT) they transform the raw channel data into frequency subbands and calculates a set of complex apodization weights for each frequency subband. Compared with DAS, they obtain an increase of contrast and lateral resolution even in the case of plane-wave US imaging (when only one emission is used). However, Diamantis *et al.* provide in [Diamantis et al., 2014] a comparison between the temporal and frequency subband approaches of MV for US images and show that there are insignificant differences, in terms of spatial resolution and contrast. Even more, the frequency subband MV solution needs up to three times more calculations than the temporal one. Moreover, Rindal *et al.* contest the improvement in contrast related to MV, and show that the improvement is rather due to the increase in lateral resolution [Rindal et al., 2014].

2.5 Subspace methods: MUSIC

MUSIC beamformer [Schmidt, 1981] is the most known method in the category of eigenspace-based beamformers. Its main development is based on the idea of separating the eigenspace of the covariance matrix of the raw channel data into signal and noise components using prior information about the covariance of the noise. The covariance matrix, $\mathbf{R}$ is decomposed as:

$$\boldsymbol{R} = \boldsymbol{U}\Lambda\boldsymbol{U}^H = \boldsymbol{U}_s\Lambda_s\boldsymbol{U}_s^H + \boldsymbol{U}_n\Lambda_n\boldsymbol{U}_n^H = \boldsymbol{U}_s\Lambda_s\boldsymbol{U}_s^H + \sigma^2\boldsymbol{U}_n\boldsymbol{U}_n^H, \tag{2.20}$$

where $\boldsymbol{U}$ and Λ are the eigenvalue decomposition of $\boldsymbol{R}$, and $\boldsymbol{U}_s, \boldsymbol{U}_n, \Lambda_s$, and $\Lambda_n = \sigma^2\boldsymbol{I}_{M-K}$ are the partitions of the eigenspectrum into signal plus noise and signal subspaces. K in this case, is the number of the point reflectors (scatterers) in the medium. To calculate the optimal weights $\boldsymbol{w}$ in the adaptive process in Fig. 2.4, the value of $\boldsymbol{R}$ obtained after applying (2.20), is replaced in (2.12). The limitation of this method is that the number of the point reflectors, K, needs to be strictly less than the number of the elements of the transducer, $K < M$. Note that, because of the large number of scatterers in the medium, the assumption of $K < M$ can hardly be guaranteed in medical US.

MUSIC beamformer is commonly used in source localization applications (typically in wireless communications, radar, sonar, and exploration seismology) [Chen et al., 2002]. The results of such beamformer consist in sharp peaks at the estimated source locations. More details about its application to medical ultrasound are discussed in Chapter 2.

2.6 Parametric methods: Maximum Likelihood

Maximum Likelihood (ML) beamformers are based on models containing parameters to be estimated and a variety of assumptions need to be taken into account (see e.g., [Krim and Viberg, 1996, Stoica and Sharman, 1990]). One possible assumption can be the shape of the signals, that can be modeled as deterministic or using statistical assumptions. Noise is usually modeled as stationary Gaussian. An example of an ML beamformer penalty function is:

$$\boldsymbol{L}_{ML}(\boldsymbol{\theta}) = ||\hat{\boldsymbol{R}} - \boldsymbol{R}||_F^2 = ||\hat{\boldsymbol{R}} - (\boldsymbol{A}\boldsymbol{S}\boldsymbol{A}^H + \sigma^2\boldsymbol{I})||_F^2, \tag{2.21}$$

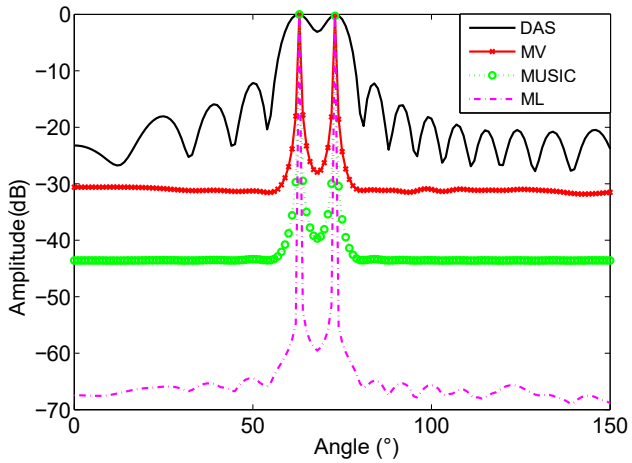

Figure 2.8: Comparison between DAS, MV, MUSIC, and ML beamformers performance to localize two sources (scatterers) in the medium.

where $||\cdot||_F$ is the Frobenius norm, $\boldsymbol{\theta}$ contains the locations for all K sources (or scatterers) in the medium, $\boldsymbol{\theta} = [\theta_1, \cdots, \theta_K]$, σ^2 is the variance of the noise, $\boldsymbol{I}$ is the identity matrix, and $\boldsymbol{A}$ is the array manifold vector $\boldsymbol{A} = [\boldsymbol{a}_1 \cdots \boldsymbol{a}_k]^T$, with $\boldsymbol{a}_i = [1 \; e^{-j\omega\Delta t_i} \ldots e^{-j\omega(M-1)\Delta t_i}]^T$. The aim of ML beamformer is to find $\boldsymbol{\theta}$ such that the penalty function in (2.21) is minimized.

The computational complexity is higher than for the aforementioned beamformers, but the benefits of ML beamformers consist in the ability to resolve coherent signals.

Fig. 2.8 compares the performances of DAS, MV, MUSIC, and ML beamformers to detect sources located at angles $\theta = 60°$ and $\theta = 70°$. The beamformers operated on a linear array with 15 elements and $\frac{\lambda}{2}$ spacing between the elements (λ is the wavelength). We can observe that the best localization of the two sources in this example, is obtained when using ML beamformer.

2.7 Beamspace beamforming

Starting from the MV BF method presented in Section 2.4.1, re-named element-space based Capon (ES-Capon) in [Nilsen and Hafizovic, 2009], Nilsen *et al.* proposed a beamspace beamformer (BS-Capon) that allowed reducing the computational complexity of the MV BF by a ratio of 3.

The beamspace transformation is expressed as follows:

$$\boldsymbol{y}_{k_{BS}} = \boldsymbol{B}\boldsymbol{y}_k, \tag{2.22}$$

where $\boldsymbol{B} = [\boldsymbol{b}_1, \cdots, \boldsymbol{b}_M]^T$ is the $M \times M$ Butler matrix whose elements are defined as:

$$b_{mn} = \frac{1}{\sqrt{M}} e^{j\frac{2\pi}{M}(m-\frac{1}{2})n}. \tag{2.23}$$

$\boldsymbol{B}$ is an unitary matrix ($\boldsymbol{B}\boldsymbol{B}^H = \boldsymbol{B}^H\boldsymbol{B} = \boldsymbol{I}_{M\times M}$), equivalent to an M-point discrete Fourier transform (DFT) matrix. $\boldsymbol{I}_{M\times M}$ is the identity matrix of size $M \times M$.

The transformation in (2.22) is applied to all signals and weights vectors in the element-space (ES) to find their beamspaced version. Therefore, the weights of ES-Capon BF are formed by solving:

$$\min_{\boldsymbol{w}_{BS}} \boldsymbol{w}_{BS}^H \boldsymbol{R}_{BS} \boldsymbol{w}_{BS}, \quad \text{such that} \quad \boldsymbol{w}_{BS}^H e_1 = 1. \tag{2.24}$$

The solution of (2.24) is:

$$\boldsymbol{w}_{BS} = \frac{\boldsymbol{R}_{BS}^{-1} e_1}{e_1^T \boldsymbol{R}_{BS}^{-1} e_1}, \tag{2.25}$$

where $\boldsymbol{R}_{BS} = E[\boldsymbol{y}_{k_{BS}} \boldsymbol{y}_{k_{BS}}^H]$ is the covariance matrix of $\boldsymbol{y}_{k_{BS}}$ and e_m is a $M \times 1$ vector having the value 1 in the m-th position and zero in all other positions. Finally, we can state that BS-Capon BF can be seen as the description of the Capon filter from (2.12) in the Fourier domain.

As stated before in this section, in the case of DAS, MV, and BS-Capon BF, the final RF US image is a collection of RF beamformed lines, each of which being the result of beamforming the raw RF signals coming from a focused wave emission in the direction θ_k, $k \in \{1, \ldots, K\}$, using the M elements of the transducer.

2.7.1 Multi-beam beamforming

Recently, to improve the MV BF, Nilsen *et al.* proposed a beamspace adaptive beamformer, BS-Capon. Unlike MV BF, they based their BF method on orthogonal beams formed in different directions [Nilsen and Hafizovic, 2009]. This technique was also applied by Jensen *et al.* to develop an adaptive beamformer based on multibeam covariance matrices [Jensen and Austeng, 2012], called multi-beam Capon beamformer.

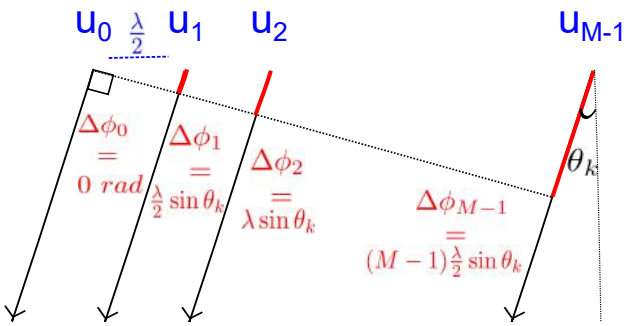

Figure 2.9: Phase shift compensation of the focused raw channel data.

In their work, a covariance matrix is calculated for each range in the image, based on the idea that the beams were transmitted with different angles. Thus, the authors of [Jensen and Austeng, 2012] were able to reduce the computation time of MV BF, while improving the resolution of point-like reflectors.

Jensen *et. al.* used beamspace processing described in Section 2.7 for reducing the dimensionality of the data, and proposed a new approach of Capon BF, called multi-beam Capon BF [Jensen and Austeng, 2012]. For more convenience, let us briefly recall their approach. For a given range (depth) n (see Fig. 2.2), let us select its corresponding lateral scanline. Since the signals $\boldsymbol{y}_{k_{BS}}$ have been focused in axial direction (by applying time delays) before being beamformed, we just need to compensate the phase-shifts based on the distances from the samples of the lateral scanline (equivalent, in our case, with K, the number of beam directions).

The compensation of the phase-shifts, $\Delta\phi_m$, with $m = 0, \cdots, M-1$ is depicted in Fig. 2.9, assuming that the time-compensated data reaches the elements at angle θ_k. We consider the first elements as reference, so its phase-shift is 0. Thus, based on the far-field assumption, the complex exponential version of the manifold vector for a given direction k, that corresponds to the incident angle θ_k, can be formulated as (see e.g., [Jensen and Austeng, 2012, Kautz and Zoltowski, 1996]):

$$\boldsymbol{a}_{\theta_k} = [1 \;\; e^{-j\pi\sin(\theta_k)} \cdots e^{-j(M-1)\pi\sin(\theta_k)}]^T. \tag{2.26}$$

Thus, by using phase shifts, for focusing along a lateral scanline, contrarily to the matrix $\boldsymbol{R}_{BS}$ used in BS-Capon, for a given range n, the covariance matrix $\boldsymbol{R}[n]$ will cover all the

directions $\theta_k,\ k = 1, \cdots, K$. Therefore, the weights corresponding to a given direction θ and a range n will be formed by solving:

$$\min_{\boldsymbol{w}} \boldsymbol{w}^H \boldsymbol{R}[n]\boldsymbol{w}, \quad \text{such that} \quad \boldsymbol{w}^H \boldsymbol{a}_{\theta,n} = 1, \tag{2.27}$$

having the solution:

$$\boldsymbol{w}_{\theta,n} = \frac{\boldsymbol{R}^{-1}[n]\boldsymbol{a}_{\theta,n}}{\boldsymbol{a}_{\theta,n}^T \boldsymbol{R}^{-1}[n]\boldsymbol{a}_{\theta,n}}. \tag{2.28}$$

These weights are then applied to calculate the signal corresponding to a lateral scanline, at a range n.

2.8 User parameter-free beamforming approaches: IAA

Iterative Adaptive Approach (IAA), referred to as user free-parameter adaptive BF, was firstly applied in US medical imagining for an accurate estimation of the blood velocity spectrum using only few transmissions [Gudmundson et al., 2011]. Jensen and Austeng compared IAA BF for medical US imaging with DAS and proved better resolution of point targets and better geometry of the cyst-like structures [Jensen and Austeng, 2014]. Unfortunately, the main disadvantage of IAA is that requires much more computations than MV.

Based on the beamspace processing technique (see Section 2.7) and on the calculation of the multibeam covariance matrix discussed in the Section 2.7.1, Jensen *et al.* applied IAA [Yardibi et al., 2008] to US medical imaging, [Jensen and Austeng, 2014]. Following this recent work, a covariance matrix, $\bar{\boldsymbol{R}}[n]$ based on $\bar{K}$ potential reflectors placed across a considered lateral scanline, was defined as:

$$\bar{\boldsymbol{R}}[n] = \sum_{k=1}^{\bar{K}} |\boldsymbol{y}_{BS}[n]|^2 \boldsymbol{a}_\theta \boldsymbol{a}_\theta^T = \boldsymbol{A}_{BS} \boldsymbol{P} \boldsymbol{A}_{BS}^T, \tag{2.29}$$

with $\boldsymbol{y}_{BS}[n] \in \mathbb{C}^{N_b \times \bar{K}}$ the beamspaced time-delayed raw channel data at a given range n, before applying the phase-shift transform. $\boldsymbol{A}$ is the matrix containing the manifold column-vectors defined in (2.26), and $\boldsymbol{P}$ a diagonal matrix with the elements of $|\boldsymbol{y}_{BS}[n]|^2$ along its diagonal.

The values of $\boldsymbol{P}$ are then iteratively updated and calculated by taking into account the weights corresponding to a lateral scanline, following (2.28). Finally, $\boldsymbol{P}$ is used to

Input: The sample covariance matrix, $\hat{\boldsymbol{R}}$, see (2.13).
Output: Amplitude squared matrix, $\boldsymbol{P}$.
1) Initial estimate of the power of each reflector by applying matched spatial filtering $\Rightarrow$ the squared version of DAS BF:

$$\boldsymbol{P}_{\theta}^{(init)} = \boldsymbol{a}_{\theta}^{T}\hat{\boldsymbol{R}}\boldsymbol{a}_{\theta}. \tag{2.30}$$

2) Iterate the following steps:

- Use $\boldsymbol{P}$ in (2.29) $\Rightarrow \bar{\boldsymbol{R}}$.
- The adaptive weights are calculated based on (2.28) $\Rightarrow \boldsymbol{w}_{\theta,n}^{T}$.
- The weights are used in (2.30) to update $\boldsymbol{P}$:

$$\boldsymbol{P}_{\theta} = \boldsymbol{w}_{\theta,n}^{T}\hat{\boldsymbol{R}}\boldsymbol{w}_{\theta,n}. \tag{2.31}$$

Until the algorithm converges. The diagonal of $\boldsymbol{P}$ contains the contribution of each potential reflector.

Algorithm 1: IAA algorithm applied to US imaging [Jensen and Austeng, 2014].

estimate the amplitude of each reflector of the IAA BF result. This is described in Algorithm 1.

Contrarily of DAS, MV and BS-Capon BF where, to form the final beamformed image, the RF lines are juxtaposed in the lateral direction, multi-beam Capon and IAA BF are axially juxtaposing the beamformed lateral scanlines to form the final beamformed image.

Fig. 2.10 illustrates the comparison between the aforementioned BF methods. The simulated data contains 6 point reflectors (4 axially aligned at the lateral distance of 0 mm and 2 laterally aligned at axial distance of 50 mm, horizontally separated by 1 mm). An hypoechoic cyst (the black circle of diameter 5 mm, centered axially at 50 mm and laterally at 15 mm) was simulated. A phased array probe of 64 elements was used, with central frequency, f_0, of 3 MHz. When using DAS BF, see Fig. 2.10(a), we can observe that the point reflectors are hardly distinguished from speckle, and the geometry of the cyst is not well defined. MV (Fig. 2.10(b)) and multi-beam Capon (Fig. 2.10(c)) beamformers give better result in terms of contrast and resolution of the point-like reflectors (see the reflector situated at depth 40 mm). The geometry of the cyst is also well resolved. Finally, with IAA BF (Fig. 2.10(d)), as stated previously in

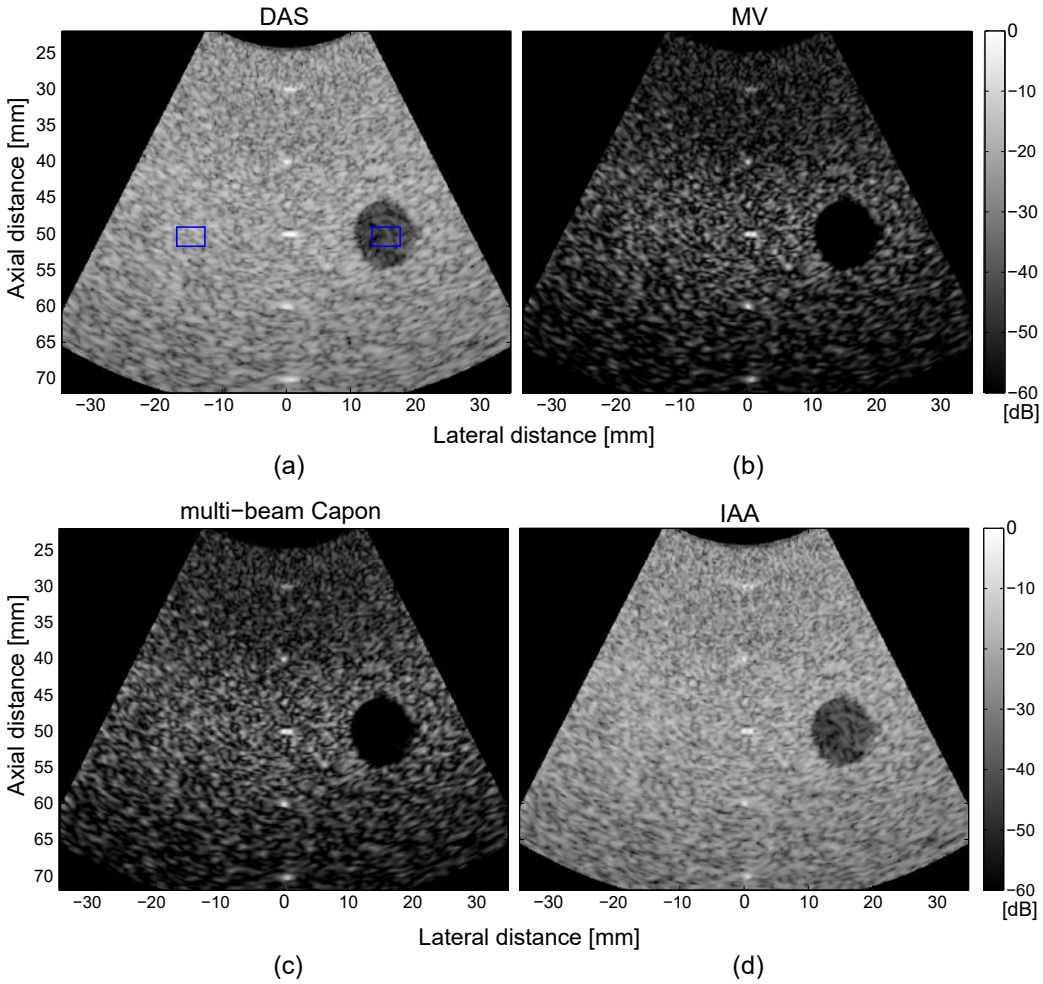

Figure 2.10: Simulated cyst phantom and point reflectors, using an 64-element, 3-MHz phased array. (a) DAS, (b) MV (L=32, T=10), (c) multi-beam Capon (L=32), (d) IAA. At depth 50 mm there are two point reflectors horizontally aligned, with a distance of 1 mm between them.

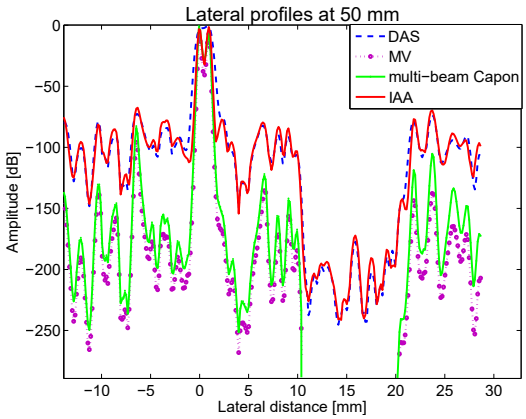

Figure 2.11: Lateral profiles at 50 mm of the beamformed images in Fig. 2.10.

Table 2.1: CR, CNR, and SNR values for beamformed images in Fig. 2.10

BF Method	CR[dB]	CNR	SNR
DAS	22.54	3.22	1.05
MV	**29.74**	2.87	0.54
multi-beam Capon	29.38	2.91	0.54
IAA	21.56	**3.25**	**1.09**

this section, the point reflectors are better resolved than DAS, MV, and multi-beam Capon (see for e.g. the point reflectors at depth 40 mm and 60 mm), while the structure of the speckle is maintained.

Fig. 2.11 contains the lateral profiles at depth 50 mm of the images in Fig. 2.10. Note that DAS BF is not capable to distinguish between the 2 close point reflectors, separated by 1 mm. However MV, multi-beam Capon, and IAA can resolve them until almost -40 dB. Regarding the cyst-like structure, we can observe that only MV and multi-beam Capon are capable to resolve its original geometry, with the exact diameter of 10 mm. In this example, DAS and IAA produce a cyst with the diameter less than 10 mm.

In Table 2.1 the values of CR, CNR, and SNR (see their definition in Section 1.2.3) are calculated for each BF method. The R_1 and R_2 regions are highlighted (with blue color) in Fig. 2.10(a). We can observe that while MV gives the best result in terms of

CR, it also degrades the SNR. However, IAA improves the CNR, while maintaining a good SNR level.

2.9 Compressive sampling beamforming

Sparse modelling gained a special interest in medical US, as for example in the applications that concern compressive sensing (CS), e.g., [Quinsac et al., 2010]. Based on compressive sampling, a frequency domain beamforming method was also proposed, called compressed beamforming [Chernyakova and Eldar, 2014]. This method allowed to reduce the number of samples needed to beamform an image containing strong reflectors, while exploiting the low bandwidth of the US signals. Tur *et al.* [Tur et al., 2011] modelled the echoes reflected by multiple reflectors located at unknown position in the medium, as a sum of a small number of pulses with known shapes. Based on this, Wagner *et al.* [Wagner et al., 2012] proposed a two-dimensional reconstruction method for US imaging, called "compressed beamforming". They used multiple array elements in receive and beamformed the sub-Nyquist received samples.

A time domain implementation of CS used in beamforming process is described in [David et al., 2015a]. Their approach is capable of reducing the number of transmissions and the number of the receiving elements in receive, while decreasing the sampling frequency. Firstly, they performed a 1D simulation to demonstrate that CS preserves resolution even if the number of the elements of US probe in reception is reduced. Then, they applied time domain CS to 2D images, by formulating beamforming as a matrix multiplication, linking the raw channel data, denoted in their paper by R and the image to be recovered, I, by using the expression: $R = GI$, where G is a linear operator, defined by simulating the Green's functions. They also applied their method on cardiac datasets [David et al., 2015b].

2.10 Beamforming in other domains

As stated in Chapter 1, beamforming has many practical applications: in wireless communications, radar, sonar, underwater acoustics, applications for monitoring and control. One particular problem solved by beamforming is source localization (with accent on the direction of arrival). Basically, the aim is to find the location of the waves that are impinging on the array of sensors. Concretely, we are interested in finding

the location of each scatterers in Fig. 1.1(c), based on the data they are reflecting and that is received by the array of sensors. Of course, this is challenging in practice, since the estimation needs to be robust in noisy conditions and to take into account the correlation of the sources. Of course, several solutions have been already discussed to estimate the direction of arrival (see Section 1.3) that treat the estimation as a direct problem. However, source location was also modeled as an inverse problem (see for e.g. [Malioutov et al., 2005, Malioutov et al., 2002, Malioutov et al., 2003]).

2.10.1 Mathematical formulation of inverse problems

Generically, the inverse function on which the source localization problem is based can be expressed as:

$$\boldsymbol{y} = T(\boldsymbol{x}) + \boldsymbol{n}, \tag{2.32}$$

where $\boldsymbol{x} \in \mathcal{X}$ is unknown, $\boldsymbol{y} \in \mathcal{Y}$ is the vector of measurements (observations), $\mathcal{X}$, $\mathcal{Y}$ are Hilbert spaces, and $\boldsymbol{n}$ is generally assumed to be a white Gaussian noise. The aim is to find $\boldsymbol{x}$ from $\boldsymbol{y}$ knowing the transformation T. However, the mapping from $\boldsymbol{y}$ to $\boldsymbol{x}$ can generate multiple difficulties as: lack of solutions, non-unique solutions, or discontinuous dependence of the solution on the observation. In these cases, the problem becomes ill-posed. The solution of (2.32) consists in regularizing the ill-posed problem as:

$$\hat{\boldsymbol{x}} = \underset{\boldsymbol{x}}{\operatorname{argmin}}(\|\boldsymbol{y} - T(\boldsymbol{x})\|_2^2 + P(\boldsymbol{x})), \tag{2.33}$$

where the first term, $\|\boldsymbol{y} - T(\boldsymbol{x})\|_2^2$ is the data-fidelity term, and $P(\boldsymbol{x})$ is a function related to the prior information one has on $\boldsymbol{x}$. $P(\boldsymbol{x})$ is thus the regularization term and contains a parameter that balances the two terms of (2.33). Moreover, $P(\boldsymbol{x})$ can be either convex or non-convex. We will see in Chapter 4 that the regularization plays a very important role in the quality of the solutions. Generally, regularization is using some prior assumptions about $\boldsymbol{x}$ to solve the ill-posed problem in (2.33), see, e.g., [Engl et al., 1996]. [Tikhonov, 1963] was the first to deal numerically with ill-posedness by introducing regularization. In this dissertation we investigate different numerical optimization tools to solve the inverse problem in (2.33).

Note that the model presented in (2.32) has already practical applications in US imaging, for different post-processing (directly on the beamformed image) techniques. Some examples are: deconvolution (e.g., [Michailovich and Tannenbaum, 2007] and

[Chen et al., 2016b]), despeckling (see e.g. [Michailovich and Tannenbaum, 2006]), and super-resolution (see e.g. [Morin et al., 2013]) techniques.

2.10.2 Beamforming as inverse problem in medical ultrasound imaging

In this thesis we modeled beamforming in medical ultrasound imaging by using the inverse problem formulated in (2.32) and we applied different regularization techniques in order to solve (2.33). How the regularization function is formed, details about the regularization parameter, and the differences from source localization methods, are explained in the next chapters, where we describe in details the contributions of this dissertation. The advantages of using such a formulation are the improvement in contrast and spatial resolution of the beamformed image and the formulation of beamforming based on a general mathematical model. Moreover, the proposed frameworks are flexible and allow for choosing the right trade-off between noise suppression and sharpness of the resulted image.

In contrast to existing BF methods in US imaging using regularized inverse problem approaches (see e.g., [Lavarello et al., 2006, Lingvall, 2004, Lingvall and Olofsson, 2007, Madore and Meral, 2012, Viola et al., 2008, Wan and Ebbini, 2009]), our methods does not use the system point spread function (PSF) in the direct model or in the inversion process. Thus, the proposed BF techniques does not require any experimental measurement (e.g., [Ellis et al., 2010]) or estimation of the PSF (e.g., [Jensen, 1992, Michailovich and Tannenbaum, 2007, Zhao et al., 2015b]). Basically, in the proposed frameworks, the observation data $\boldsymbol{y}$ is the raw channel data of the US system, while the structures of $T(\boldsymbol{x})$ and $P(\boldsymbol{x})$ are differently formulated in each of the three contributions, in function of the application and aims of the proposed beamforming methods. We present in details each of the contributions in Chapters 3, 4, and 5.

2. BEAMFORMING IN MEDICAL ULTRASOUND IMAGING: STATE OF THE ART

3

Strong reflector-based beamforming in medical ultrasound imaging

This chapter is based on the journal paper [Szasz et al., 2016c]. Part of this chapter was also published in [Szasz et al., 2014] and [Szasz et al., 2015].

Contents

3.1 Introduction

This chapter investigates the use of sparse priors in creating original two-dimensional beamforming methods for ultrasound imaging. The proposed approaches detect the strong reflectors from the scanned medium based on the well known Bayesian Information Criteria used in statistical modeling. Moreover, they allow a parametric selection of the level of speckle in the final beamformed image.

Firstly, we propose a sparse signal representation by extending the DAS BF method presented in Section 2.3 with BIC (Bayesian Information Criteria) selection criteria. Then, we extend MV BF method presented in Section 2.4.1 with BIC in order to exploit the advantages of the MV BF to our sparse modeling. Finally, we propose a new method that computes the final beamformed image by combining the sparse representation with the DAS and MV beamformed results. Compared with DAS and MV, we increase the contrast while preserving the speckle (that frequently contain important clinical information) in the final beamformed image.

3.2 Beamforming with sparse priors

Based on the beamforming methods reviewed in Chapter 2, the proposed method consists in detecting and reinforcing the strong reflectors in the RF images. In practice, these reflectors may be associated to the tissue boundaries or the small hyperechoic structures (see, e.g., [Tur et al., 2011], [Wagner et al., 2012]).

As we will explain below, the strong reflector detection is based on the minimization of the Bayesian Information Criteria (BIC), balancing between data fidelity and a sparsity-based penalization term [Konishi and Kitagawa, 2008].

3.2.1 Sparse strong reflector model

The strong reflector model of an RF image $\boldsymbol{S}$, considered herein as a collection of M RF lines each one having N samples, is given as:

$$\begin{aligned} \boldsymbol{S}(x,n) &= \sum_{p=1}^{P} a_p \boldsymbol{h}_p(x-x_p, n-n_p), \\ x = x_1, \cdots, x_M \quad &\text{and} \quad n = 1, \cdots, N, \end{aligned} \tag{3.1}$$

where n stands for the time or axial (longitudinal) direction, x is the lateral direction variable, and $\boldsymbol{S}(x,n)$ is the beamformed RF image. (x_p, n_p), with $p = 1, \cdots, P$ are the positions of the P strong reflectors to be detected during the proposed beamforming process. We denote with a_p the amplitudes of the strong reflectors and with $\boldsymbol{h}_p(x,n)$ the backscattered pulse corresponding to the strong reflector p, both supposed unknown and to be estimated. In this case the term sparsity is related to the relatively low number of strong reflectors to be detected by the proposed method.

3.2.2 Strong reflector detection and parameter estimation

In this section, we describe the proposed process of strong reflector detection and parameter estimation. The proposed method is mainly divided in two steps: the detection step, based on the previously beamformed RF lines, finds the strong reflectors taking into account the amplitudes of the RF signals. Then, the validation step uses the raw channel data to confirm the previously detected reflectors through the BIC criteria. The main reason of processing the detection of the strong reflectors on beamformed data instead of raw channel data is related to the SNR that is naturally higher on standardly beamformed data compared to raw channel data. Thus, we expect that the results are less affected by the low SNR when detecting the peaks on DAS or MV images.

For the ease of understanding, we use the same notations as in Chapter 2, corresponding to a classical pulse echo US image (see Section 1.1.5). The raw channel data is collected with the corresponding M elements (which can represent either the active elements of the probe of all the elements of the probe), resulting into a data matrix of size $M \times N$, denoted by $\boldsymbol{Y}_d^{(k)}$. More precisely, $\boldsymbol{y}_d^{(k)}(n)$ is a $M \times 1$ line corresponding to emission number (k) and to depth n, after the dynamic focalisation of the received echoes. As explained in the Section 2.3 and Section 2.4.1, the total amount of raw channel data is used in non-adaptive BF process to obtain the DAS beamformed RF image denoted herein by $\hat{\boldsymbol{S}}$, or in an adaptive BF process to form the MV beamformed RF image denoted herein by $\tilde{\boldsymbol{S}}$. We denoted in Section 2.3 by $\hat{\boldsymbol{s}_k}$, and in Section 2.4.1 by $\tilde{\boldsymbol{s}_k}$ the k^{th} RF signals extracted from $\hat{\boldsymbol{S}}$, respectively $\tilde{\boldsymbol{S}}$. Our strong reflector detection and parameter estimation method uses both the raw channel data $\boldsymbol{Y}_d^{(k)}$, and the beamformed RF images $\hat{\boldsymbol{S}}$ or $\tilde{\boldsymbol{S}}$. Both proposed approaches, using the DAS or MV beamformed RF images, are similar and will be referred as USBIC, respectively M-USBIC in the reminder of this chapter.

Two main steps are used within the proposed method. The first step uses $\hat{\boldsymbol{S}}$ or $\tilde{\boldsymbol{S}}$ to detect a potential strong reflector (its position, amplitude, and pulse response). The second step validates this choice and estimation based on a cost function implying the raw channel data. The first and the second steps are alternatively repeated until the algorithm stops (the minimum of BIC is reached). Moreover, an initial one-dimensional (1D) approach is followed by a two-dimensional (2D) refinement, both using the two aforementioned steps. In the following, we describe only the steps required to form the USBIC beamformed RF image (denoted with $\boldsymbol{S}^{(P)}$ in this chapter). In this case we use as input the DAS beamformed RF image $\hat{\boldsymbol{S}}$, and the raw channel data $\boldsymbol{Y}_d^{(k)}$. The steps to form the M-USBIC beamformed RF image (when the MV beamformed RF image $\tilde{\boldsymbol{S}}$ and the $\boldsymbol{Y}_d^{(k)}$ are the inputs) are identical with the ones required to form USBIC beamformed RF image.

3.2.2.1 1D initialization procedure:

For each beamformed RF line $\hat{\boldsymbol{s}}_k$ at lateral position x_k the strong reflector detection and validation are iterated. For iteration p, the two steps are process as follows:

Step 1 - Strong reflector detection

$$\begin{aligned} n_p &= \underset{n\setminus\{n_1,\cdots,n_{p-1}\}}{\operatorname{argmax}} (|\hat{\boldsymbol{s}}_k(n)|), \\ a_p &= |\hat{\boldsymbol{s}}_k(n_p)|, \\ \boldsymbol{h}_p(x_k,n) &= \hat{\boldsymbol{S}}(x_k,n) \circ \boldsymbol{w}_{\boldsymbol{h}}(n), \\ n &= [n_p - \frac{\tau_{pulse}\cdot f_s}{2}, \cdots, n_p + \frac{\tau_{pulse}\cdot f_s}{2}], \end{aligned} \tag{3.2}$$

where n_p is in the interval $\{1,\ldots,N\}$, $\hat{\boldsymbol{S}}(x_k,n)$ is the DAS beamformed image, $\boldsymbol{w}_{\boldsymbol{h}}$ is a Hanning window, τ_{pulse} is the predefined pulse length (equal to twice the excitation length in this dissertation), f_s is the sampling frequency, $\circ$ defines the Hadamard product, and argmax stands for the argument of the maximum. The current form of the detected strong reflector RF signal, after p iterations, is:

$$\boldsymbol{s_k}^{(p)} \triangleq \boldsymbol{S}^{(p)}(x_k,n) = \sum_{l=1}^{p} a_l \boldsymbol{h}_l(x_k,n), \tag{3.3}$$

where $\boldsymbol{s_k}^{(p)}$ is the $k-th$ column of the RF image $\boldsymbol{S}^{(p)}(x,n)$, at the iteration p.

Step 2 - Validation In the second step of each iteration, a cost function is calculated balancing between on the one hand, the data fidelity between the current RF model in (3.3) and the raw channel data and on the other hand, the sparsity of the strong reflectors. The BIC evaluation criterion [Konishi and Kitagawa, 2008] is one of the most used information criteria in statistics, having the role of assessing the closeness between the predictive distribution defined by a statistical model and the true distribution. A statistical model uses the observed data to approximate the true distribution of certain probabilistic events. Let $g(v_n|\hat{\theta})$ be a statistical model estimated by the maximum likelihood method. Than, the BIC criterion is defined as:

$$BIC(n) = -2\log g(v_n|\hat{\theta}) + p\log n, \tag{3.4}$$

where θ is the unknown parameter, $\hat{\theta}$ is its estimator, and v_n are the observations, $v_n = \{v_1, v_2, \cdots, v_n\}$. Inspired from the application of BIC with IAA for obtaining sparsity by estimating the number of sources in array processing, described in [Yardibi et al., 2010], BIC was adapted herein to US imaging. The cost function $f_{1D}(p)$ has the following form:

$$f_{1D}(p) = \overbrace{\log(\|\boldsymbol{s_k}^{(p)} \cdot \mathbf{1}^\top - \boldsymbol{y}_d^{(k)}\|_2^2)}^{\text{data fidelity}} + \underbrace{\lambda p \log(N)}_{\text{sparsity constraint}}, \tag{3.5}$$

where λ is an user-defined parameter fixing the compromise between the data attachment and the sparsity. Even if the automatic choice of the λ is out of the scope of this chapter, note that there exist in literature several approaches that automatically determine the value of this kind of hyperparameter, e.g., [Candes et al., 2008, Dobigeon et al., 2012, Galatsanos and Katsaggelos, 1992, Ramani et al., 2012].

For each RF line, *Step 1* and *Step 2* are iterated until the cost function in (3.5) starts to increase (i.e. $f_{1D}(p+1) > f_{1D}(p)$). Note that the data fidelity term is not related to already beamformed RF lines, but to the raw channel data (native data received by each element of the US probe), at each iteration, having the dimension $M \times N$. Let us denote by Ψ the set of all the strong reflector positions detected from all individual RF lines. Applied on each RF line, the algorithm tends to overestimate the number of strong reflectors. Moreover and more important, it does not ensure a spatial coherence between the neighboring RF lines. For this reason, a 2D approach follows the 1D method, and is presented bellow. It will choose a subset of strong reflectors of

Ψ respecting a 2D BIC criteria. The main advantage of applying the 1D approach is to speed up (at least three times in our experiments) the 2D process that will have as input just the potential strong reflectors detected previously by the 1D method for each RF line.

3.2.2.2 2D refinement procedure:

For the refinement of the previously detected reflectors (by the 1D approach) we use the set Ψ, representing all the strong reflectors positions of all the RF lines. For all strong reflectors detected in the 1D approach, an 2D - adapted BIC criteria is applied. The process of the 2D refinement iteratively gathers the best positions from the set Ψ, as follows:

$$n_p = \underset{n \in \Psi \setminus \{n_1, \cdots, n_{p-1}\}}{\operatorname{argmax}} (a_n), \tag{3.6}$$

where a_n is expressed in (3.2). The selected strong reflectors are plugged into the 2D BIC criteria, given by:

$$f_{2D}(p) = \overbrace{\log(\sum_{k=1}^{M} \|\boldsymbol{s_k}^{(p)} \cdot \mathbf{1}^\top - \boldsymbol{y}_d^{(k)}\|_2^2)}^{\text{data fidelity}} + \underbrace{\lambda p \log(N)}_{\text{sparsity constraint}}, \tag{3.7}$$

where $\boldsymbol{s_k}^{(p)}$ is defined in (3.3). The 2D validation step is iterated until the function $f_{2D}(p)$ starts to increase, similar as for the *1D initialization approach*. Moreover, as stated in Section 3.2.2.1, the data fidelity term for the 2D approach is composed of all the focused raw channel data corresponding to all emissions, having the dimension $M \times M \times N$.

3.2.3 Final image computation

As we will show in the results section, the method introduced in the Section 3.2.2 has a good ability to detect the strong reflectors and to provide a sparse version of the RF image. However, it does not preserve the speckle characteristics, that can contain clinical information, in the case when the examined medium is not sparse. For this reason, we propose to further combine our sparse RF image with the one that is classically beamformed with DAS or MV, as shown below. If the DAS RF image $\hat{\boldsymbol{S}}$ is

used (for strong reflector detection and final image combination), we call the resulted image USBIC. If the MV RF image $\tilde{\boldsymbol{S}}$ is used, we call it M-USBIC. Hence, the final USBIC beamformed image can be expressed as:

$$\boldsymbol{S}_{USBIC} = \gamma \cdot \hat{\boldsymbol{S}} + (1-\gamma) \cdot \boldsymbol{S}^{(P)}, \tag{3.8}$$

where $\boldsymbol{S}^{(P)}$ is the beamformed image obtained using our sparse strong reflector model and is defined in (3.1), γ is the parameter that control the level of speckle in the final image, and P is the number of the strong reflectors detected after the p iterations.

Similar, the M-USBIC has the following expression:

$$\boldsymbol{S}_{M-USBIC} = \gamma \cdot \tilde{\boldsymbol{S}} + (1-\gamma) \cdot \boldsymbol{S}^{(P)} \tag{3.9}$$

Note that $\boldsymbol{S}^{(P)}$ be obtained either by using the DAS beamformed image (in the case of USBIC, or starting from the MV beamformed image (in the case of M-USBIC).

3.3 Experiments

In order to evaluate the proposed USBIC and M-USBIC BF approaches, we have considered three different simulated examples using the Field II simulation program [Jensen and Svendsen, 1992] and one recorded ultrasound phantom data. The first simulated medium is based on a sparse assumption of the reflectors. The second one is based on simulated data from scenes of point-targets and scenes of cysts in speckle considering a phased array imaging technique. The third example represents the simulation of a cardiac image (the amplitudes of the scatterers were related to the grey levels of an Apical 4 Chambers (A4C) view image, as suggested in [Alessandrini et al., 2012]). The experimental data was acquired with an Ultrasonix MDP research platform. The simulation and experimental parameters are resumed in the Table 3.1.

For all the following examples, the improved version of MV BF was used, the one that gives the best results in [Asl and Mahloojifar, 2009], with spatial averaging with $L = M/2 = 32$, temporal averaging $T = 10$, and the diagonal loading factor $\Delta = 1/L$. The B-mode image computation was processed in a standard manner and in the same way for all the resulted images: Hilbert-based demodulation and logarithmic compression (see Section 1.2).

3.3.1 Simulated point reflectors

Table 3.1: Parameters of simulated and experimental images

Parameters	Point reflectors	Reflectors and cyst	Cardiac image	Experimental phantom
for simulation of:	**(Fig. 3.1)**	**(Fig. 3.3)**	**(Fig. 3.6)**	**(Fig. 3.8)**
Transducer				
Transducer type	Linear array	Phased array		Linear array
Transducer element pitch [μm]	475	132	231	118
Transducer element kerf [μm]	35	22	38.5	25
Transducer element height [mm]	5	5	14	4
Central frequency, f_0 [MHz]	3.5	7	4	7
Sampling frequency, f_s [MHz]	100	60	40	40
Speed of sound, c [m/s]			1540	
Wavelength [μm]	440	220	385	220
Excitation pulse			Two-cycle sinusoidal at f_0	
Synthetic Aperture Emission				
Receive Apodization			Hanning	
Number of transmitting elements	64	128	64	128
Number of receiving elements	64	128	64	128
Number of emissions	129	128	204	192

A scanned grid with 14 point reflectors was simulated, laterally aligned in pairs of two and separated by 4 mm. They are located at axial depths ranging from 40 to 80 mm, with a transmit focus at 50 mm and a dynamic receive focalisation.

3.3.2 Simulated point reflectors and cyst data

For this type of simulation the medium was scanned with a 7 MHz 128-element phased array transducer with $\lambda/2$, λ being the wavelength, spacing and Hanning apodization. A two-cycle sinusoidal was used as excitation and the transmit focus was set to 60 mm. We adopted a dynamically receive focalisation ranging from 5 to 150 mm. The images consist in 128 lines with 0.7 degrees between consecutive lines. The medium consists in several circular cysts: an anechoic one with radius 2 mm, a hyperechoic one with radius 3 mm, an echoic one with radius 2 mm and one hypo-echoic with radius 1.5 mm. It also contains nine point reflectors situated at different positions. The scatterers are uniformly random distributed within the phantom cyst, and the scatterer amplitudes are Gaussian distributed with a standard deviation determined by the scatterer map, with the amplitude of the scatterers mapped to the intensity given through a bitmap image.

3.3.3 Simulated cardiac apical view image

The Apical 4 Chambers (A4C) view is a well exploited perspective in echocardiography, containing information about the left ventricle (LV) and right ventricle (RV) of the heart. A 3.75 MHz 64-elements transducer sectorial probe was used to obtain the simulated data which holds information about the LV, the scatterers having uniform random positions. The sampling frequency is 40 MHz, the view angle 66°, the transmit focus point is set to 65 mm, and a pitch equal with half of one wavelength is used to avoid grating lobes effects. The final image is ultra-realistic, the amplitudes being related to an in-vivo cardiac image [Alessandrini et al., 2012]. For both point reflectors with cyst data (Section 3.3.2) and cardiac image simulations, the number of scatterers was sufficiently large to produce fully developed speckle.

3.3.4 Recorded phantom data

The phantom data was recorded using the Ultrasonix MDP research platform equipped with the parallel channel acquisition system SonixDaq and the linear L14-W/60 Prosonic©

(Korea) ultrasonic probe having 128 elements with height of 4 mm, sub-element width of 0.093 mm, and kerf of 0.025 mm. The central frequency is $f_0 = 7$ MHz and the sampling frequency is $f_s = 40$ MHz. The scanned medium is a general-purpose ultrasound phantom CIRS Model 054GS.

3.4 Results and discussion

This section presents the results of applying the proposed methods on both simulated and *in vivo* data. Three conventional image quality metrics were calculated: CR index, CNR, and SNR. Their definition is given in Section 1.2.3.

3.4.1 Sparsely located point reflectors

With this simulation we evaluated the potential of the proposed methods to precisely detect the strong reflectors in sparse mediums. The results prove that all the 14 sparsely located reflectors are detected at correct positions. The beamformed responses are illustrated in the Fig. 3.1. One can observe that using DAS BF with a Hanning apodisation window (Fig. 3.1(a)) produces results with poor lateral resolution and high sidelobes. Although MV offers better resolution, the sidelobes are still remarkable, Fig. 3.1(b). Clearly, Fig. 3.1(c) and Fig. 3.1(d) present superiority over DAS and MV BF in terms of lowering the sidelobes of the final image. These results validate that USBIC and M-USBIC beamformers correctly detect the strong reflectors in a sparse medium. For a sparse medium USBIC and M-USBIC give a good approximation of the reflectors' position. λ can range between 0.8 and 1 for a perfect detection of the number of reflectors. Since we are dealing with a sparse medium with no speckle, γ was set to 0 for this result.

Note that, even if the amplitude of the response of the reflectors obtained with DAS is decreasing with depth (see Fig. 3.1(a)), the proposed method is able to detect the 14 reflectors placed at different depths. Contrarily, a simple thresholding method would firstly select the positions corresponding to the sidelobes of the first reflected echoes before selecting the position corresponding to scatterers at higher depths.

In the Fig. 3.2 we reinforce the conclusions related to the capability of the strong reflector based approaches to eliminate the sidelobes by drawing the lateral variation of the beamformed responses at axial depth of 50 mm (Fig. 3.2(a)) and 70 mm (Fig. 3.2(b)).

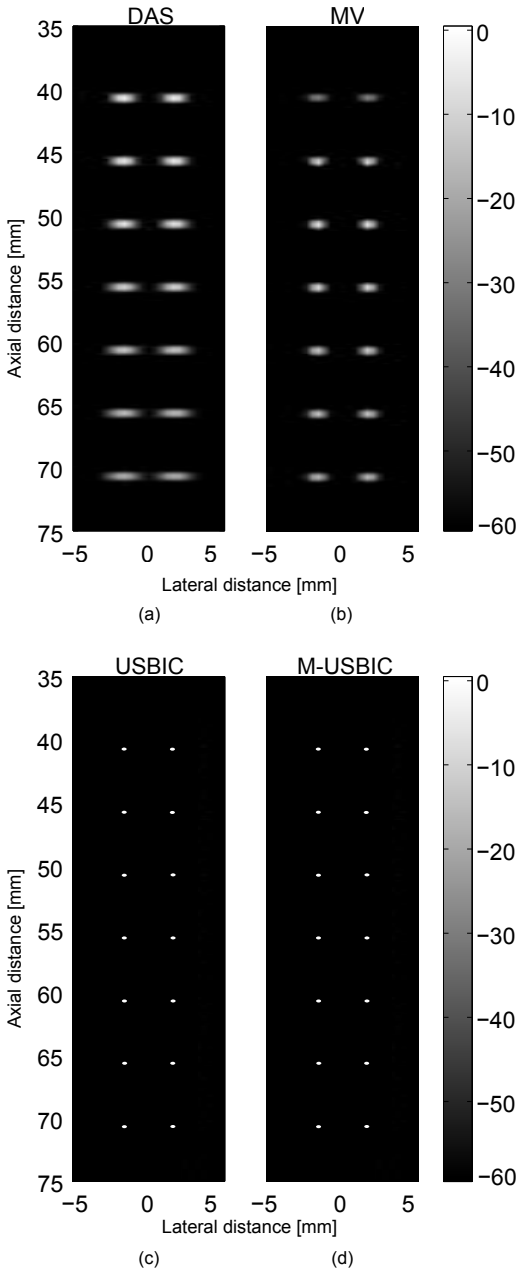

Figure 3.1: (a) DAS, (b) MV, (c) USBIC, and (d) M-USBIC BF results of 14 sparsely located reflectors.

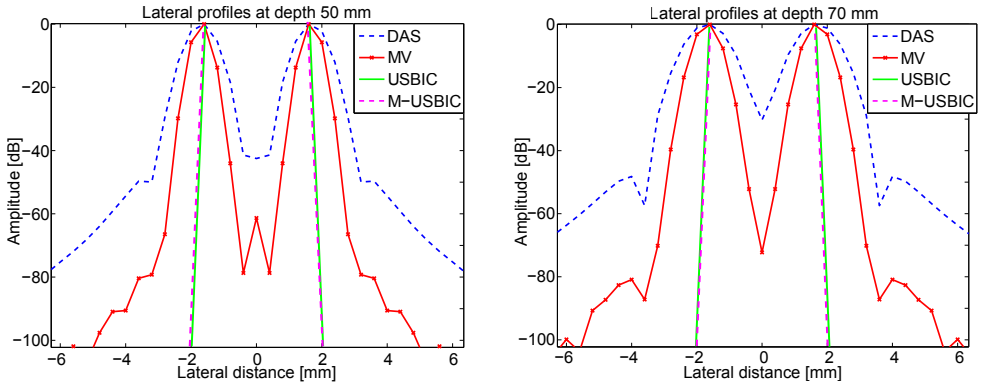

(a) (b)

Figure 3.2: Lateral variations of the images from the Fig. 3.1 at (a) depth 50 mm and (b) 70 mm.

We can clearly observe the ability of USBIC and M-USBIC to correctly detect the isolated scatterers, compared to the relatively large mainlobe and high sidelobes generated by standard beamforming techniques.

3.4.2 Point reflectors and cyst data

Fig. 3.3 presents the BF results of a simulated medium with the phased array imaging technique. The image quality metrics are detailed in the Table 3.2. We calculate CR and CNR on anechoic and hyperechoic cysts (in Fig. 3.3(a), they are delimited by white circles). For both cases the R_2 regions are the black circles situated at the same depth with the bounded cysts, as suggested in [Rindal et al., 2014]. For the calculation of the SNR, the ROIs are all the black encircled regions together with the gray surrounded region. The SNR was calculated for each region and the final value is the average of the three SNRs. As stated in [Rindal et al., 2014], while the ROIs of the cysts are chosen exactly at the limit of the cysts (Fig. 3.3(a)), we are not greatly enhancing the contrast by using MV (Fig. 3.3(b)), compared with DAS. On the other hand, by using USBIC or M-USBIC BF, it is normal to have a decrease in CR and CNR in comparison with DAS and MV when dealing with the anechoic cyst, since their aim is to remove speckle in the final image. Besides, evaluated for hyperechoic cyst and compared with DAS, M-USBIC has an improvement of more than 10 dB and of 1.6 in CR, respectively CNR, Table 3.2. With USBIC we can maintain a good CR even for

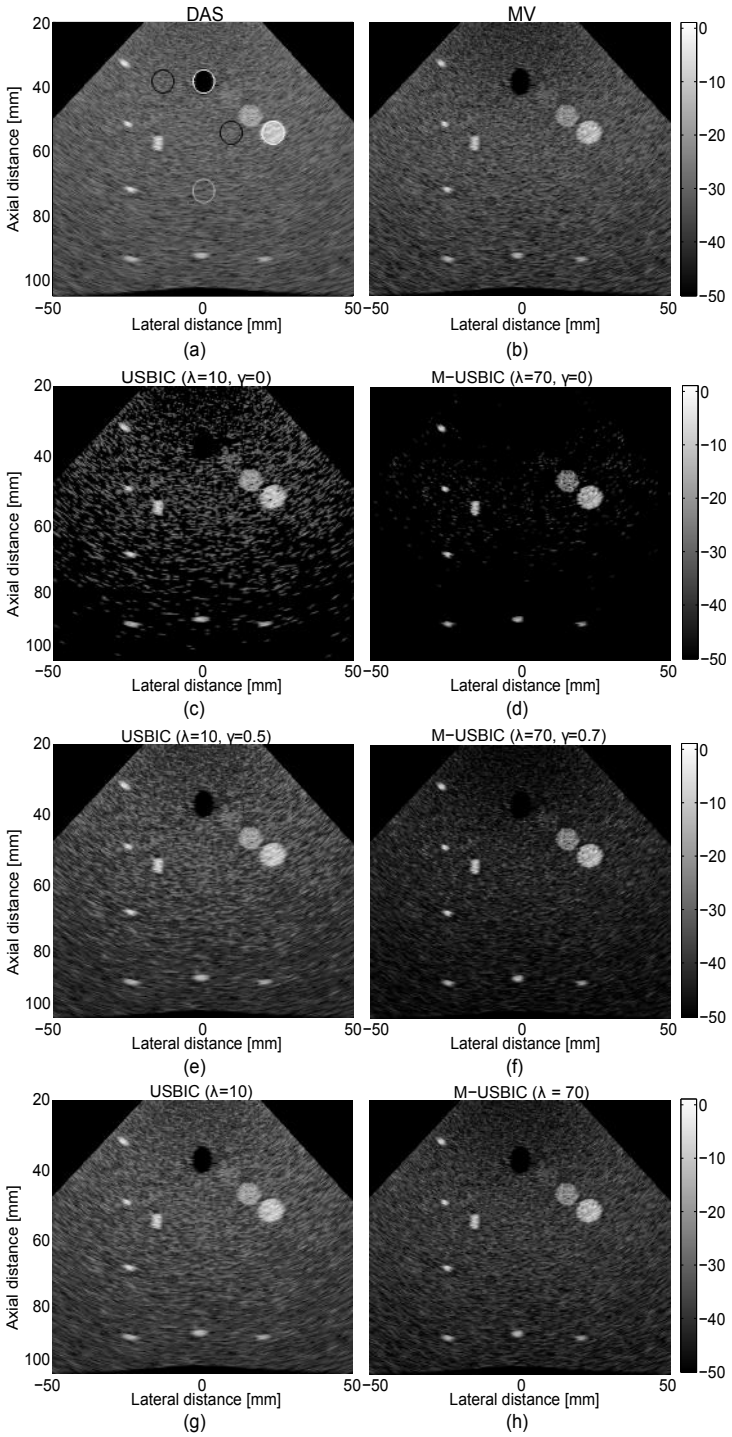

Figure 3.3: Results of (a) DAS, (b) MV, (c) USBIC with $\lambda = 10$, and $\gamma = 0$, (d) M-USBIC with $\lambda = 70$ and $\gamma = 0$, (e) USBIC with $\lambda = 10$, $\gamma = 0.5$, and (f) M-USBIC with $\lambda = 70$ and $\gamma = 0.7$, (g) USBIC with $\lambda = 10$, and (h) M-USBIC with $\lambda = 70$ on a simulated medium using the phased array imaging technique. The image quality metrics: CR, CNR, and SNR are given in the Table 3.2.

anechoic cyst, while increasing by more than 10 dB the CR of the hyperechoic cyst, Fig. 3.3(d). Moreover, the proposed methods provide a trade-off between increasing the contrast and maintaining the speckle in the beamformed images, producing a gain of 4 in SNR when using M-USBIC BF (Fig. 3.3(f)) and of 0.7 when using USBIC (Fig. 3.3(e)), in comparison with DAS. Varying the parameters λ and γ allows the control of the number of the strong reflectors and the speckle information in the final image. We need to precise that the results are not too sensitive to the choice of λ. A change with an order of 10 must be chosen in order to have some remarkable differences between the final results. However, the higher λ is, the more the speckle will be eliminated. This can highly affect the final result, while the speckle contains important information by delimiting the anechoic cyst. As solutions, we can decrease the value of λ, or increase the value of γ, that represents the percentage in the final image of the level of speckle present in DAS (in the case of USBIC) or MV (in the case of M-USBIC) results. For this example, USBIC BF with $\lambda = 10$ and $\gamma = 0.5$, and M-USBIC BF with $\lambda = 70$ and $\gamma = 0.7$ perform the best results in terms of preserving the speckle while increasing the contrast of the final image.

The main issue of using a low γ parameter is that the contrast of anechoic cysts tends to be attenuated with the decrease in γ. A simple way to overcome this issue is to choose $\gamma = \frac{1}{2}$ that is, to give the weight to each term in (3.8) and (3.9) which is a fair (and easy to achive) compromise. For example, by adding the images in Fig. 3.3(a) and Fig. 3.3(c) we obtain the result in Fig. 3.3(g). Similarly, by summing the images in Fig. 3.3(b) and Fig. 3.3(d) results into the image in Fig. 3.3(h). From Fig. 3.3(g) and Fig. 3.3(h) we can observe that the anechoic cyst is better defined compared with the results when the images obtained with USBIC and M-USBIC are weighted with γ. This observation is enforced by the results of CR, CNR and SNR from Table 3.2, where for USBIC ($\lambda = 10$) the values of CR and CNR for the anechoic cyst are very close to the ones for DAS image, while the SNR is improved. Moreover, the hyperechoic cyst has better contrast than DAS, but not so important as when using the weighting parameter γ for computing the final result. Similar remarks can be formulated for M-USBIC ($\lambda = 70$) that preserves the low echoic region in the beamformed image. Thus, even if the aim of the proposed methods are to detect the strong reflectors present in the medium, if there exist anechoic structures, they can be preserved, by adding the speckle

Table 3.2: CR, CNR and SNR values of the beamformed images using the simulated point reflectors and cyst data medium, Fig. 3.3

	Anechoic cyst		**Hyperechoic cyst**		**Black-circle**
BF method	**CR [dB]**	**CNR**	**CR [dB]**	**CNR**	**SNR**
DAS	**29.785**	5.120	33.703	2.621	3.061
MV	21.953	5.290	34.712	2.980	3.770
USBIC ($\lambda = 10, \gamma = 0$)	10.469	3.710	47.586	4.233	3.912
USBIC ($\lambda = 10, \gamma = 0.5$)	23.391	**5.315**	39.634	3.281	3.701
USBIC ($\lambda = 10$)	25.223	5.273	38.052	3.082	3.570
M-USBIC ($\lambda = 10, \gamma = 0$)	0.185	0.693	**54.320**	**5.557**	6.365
M-USBIC ($\lambda = 70, \gamma = 0.7$)	8.875	4.943	45.435	4.348	**7.042**
M-USBIC ($\lambda = 70$)	15.102	5.213	40.524	3.702	5.044

from the DAS or MV images to the USBIC, respectively M-USBIC results, without any weighting parameter γ.

The previous observations are enforced by Fig. 3.4, where the lateral profiles around the anechoic (Fig. 3.4(a)) and hyperechoic (Fig. 3.4(b)) cysts are drawn. For this figure we considered USBIC with $\lambda = 10$ and $\gamma = 0.5$ (Fig. 3.3(e)), and M-USBIC with $\lambda = 70$ and $\gamma = 0.7$ (Fig. 3.3(f)). We can observe that the lateral profile when using USBIC is comparable with MV, and has wider mainlobe than DAS in the case of anychoic cyst's profile (Fig. 3.4(a)), while its propose is to eliminate speckle around the cyst. M-USBIC is eliminating even more the speckle, so the hyperechoic cyst will be enlarged. However, for anechoic cysts M-USBIC provides the narrower mainlobe, the cyst appearing more well defined in the Fig. 3.3(f). The lateral profiles when using USBIC and M-USBIC have lower average in amplitude, due to the fact that only one fraction $(1 - \gamma)$ of the DAS and MV beamformed images are added to the image $\mathbf{S}$ (USBIC or M-USBIC), see (3.8) and (3.9). Thus, we may remark that the main advantage of our method is to improve the contrast of hyperechoic structures, based on the detection of strong reflectors. However, by adding speckle to the final images, despite a reduction of this contrast gain, we manage to maintain a contrast of hypoechoic structures close to the one provided by existing beamforming techniques.

For this example, USBIC with $\lambda = 10$ corresponding to the image in Fig. 3.3(c), required 8783 iterations, that is equivalent to the number of the detected reflectors,

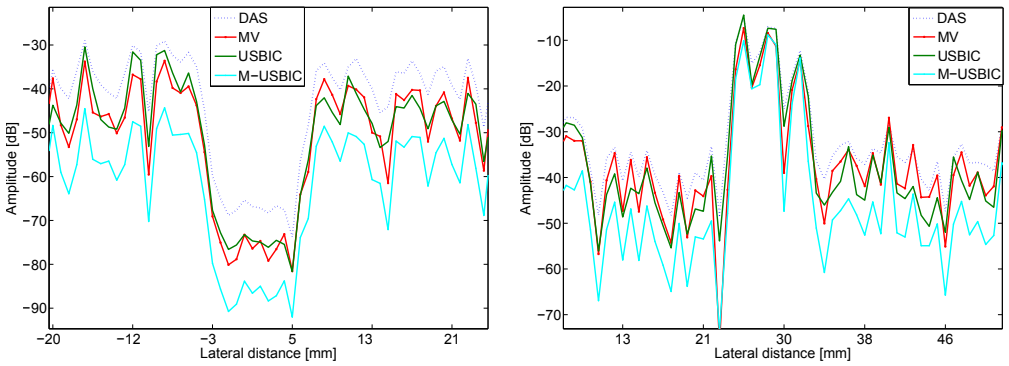

(a) (b)

Figure 3.4: Lateral profiles of the images from the Fig. 3.3. (a) The lateral profile at the axial depth of 40 mm, that intersects the anechoic cyst; (b) The lateral profile at the axial depth of 70 mm, that intersects the hyperchoic cyst. The lateral profiles were drawn considering USBIC with $\lambda = 10$ and $\gamma = 0.5$ (Fig. 3.3(e)), and M-USBIC with $\lambda = 70$ and $\gamma = 0.7$ (Fig. 3.3(f)).

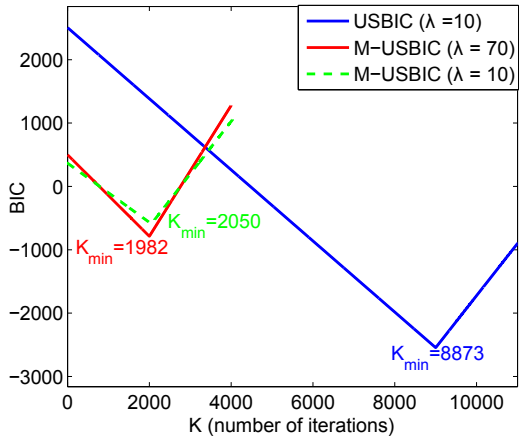

Figure 3.5: Values of BIC versus K for USBIC with $\lambda = 10$ and $\gamma = 0$ (Fig. 3.3(c)) and M-USBIC with $\lambda = 70$ and $\gamma = 0$ (Fig. 3.3(d)).

Table 3.3: CR, CNR and SNR values of the beamformed images using the simulated cardiac apical view medium, Fig. 3.6

BF method	CR[dB]	CNR	SNR
DAS	10.938	1.209	**1.285**
MV	10.366	0.663	0.609
USBIC ($\lambda = 50, \gamma = 0$)	**35.210**	**1.478**	0.321
USBIC ($\lambda = 50$, $\gamma = 0.5$)	14.975	1.475	1.055
M-USBIC ($\lambda = 25, \gamma = 0$)	33.110	1.092	0.272
M-USBIC ($\lambda = 25$, $\gamma = 0.5$)	12.283	0.733	0.569

while M-USBIC dissociated 1982 strong reflectors, when $\lambda = 70$ (corresponding to the result in Fig. 3.3(d)). The two plots corresponding to USBIC and M-USBIC for this case are drawn in the Fig. 3.5. We have also depicted the case when M-USBIC is used with $\lambda = 10$, for comparing the impact of keeping the same value of λ on the two methods. We can observe that for the same λ, M-USBIC tends to detect less strong reflectors (2050), dissociating better than USBIC the strong reflectors from the speckle. This is due to the increase in CR, CNR, and SNR of MV, compared with DAS. We also emphasize that the number of strong reflectors detected with M-USBIC only slightly decreases when λ changes from 10 to 70.

3.4.3 Cardiac apical view image

The results of beamforming on a simulated A4C view cardiac medium are illustrated in the Fig. 3.6. To compute CR and CNR, R_1 was defined as the region inside the white rectangle around the position 58 mm (axial) and -10 mm (lateral) from the Fig. 3.6(a) together with the R_2 (the region inside the white rectangle around 8 mm (axial), situated at the same depth as $R1$). For SNR, the regions surrounded by the black rectangles were chosen. The SNR was calculated according to (1.19) for each region and the average value was extracted. Table 3.3 lists the CR, CNR, and SNR values for each BF method.

In coherence with the conclusions stated in [Rindal et al., 2014], MV does not exhibit a higher contrast than DAS when selecting a small ROI, see Table 3.3. Contrarily, we obtain an improvement in CR of more than 20 dB with USBIC and M-USBIC, compared with DAS and MV, Fig. (3.6(c) and Fig. (3.6(d). Of course, in these situations, due to the elimination of the level of speckle, the SNR is much smaller than for DAS and

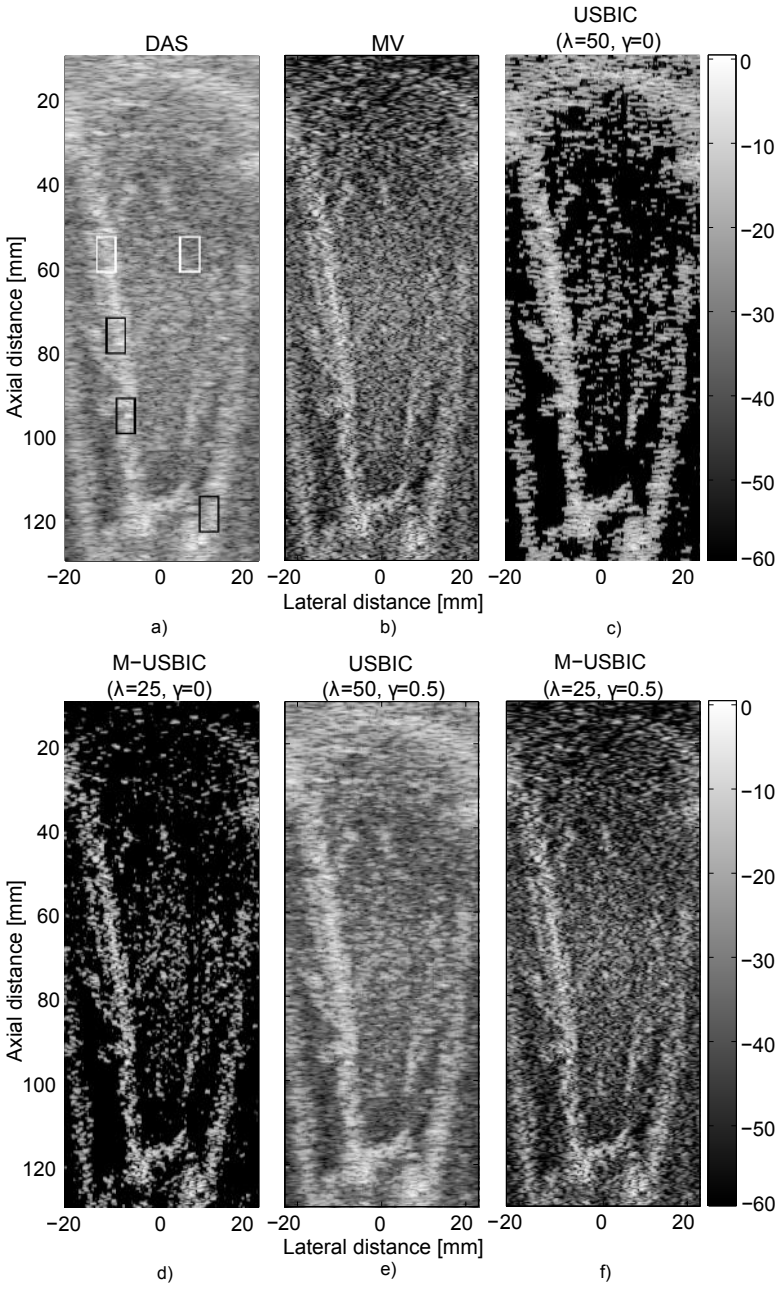

Figure 3.6: Results of (a) DAS, (b) MV, (c) USBIC with $\lambda = 50$, and $\gamma = 0$, (d) M-USBIC with $\lambda = 25$ and $\gamma = 0$, (e) USBIC with $\lambda = 50$, and $\gamma = 0.5$, and (f) M-USBIC with $\lambda = 25$ and $\gamma = 0.5$ on a simulated cardiac apical view image. The image quality metrics: CR, CNR, and SNR are given in the Table 3.3. In (a) we marked the regions used for the calculation of CR, CNR, and SNR.

MV. Our empirical experience shows that a value of $\lambda \approx 50$ is optimal in terms of contrast and visual perception of the resulted beamformed image when we use USBIC BF approach (Fig. (3.6(e)), and a value of $\lambda \approx 25$ for M-USBIC BF (Fig. (3.6(f)). When dealing with a non-sparse medium, γ is an important parameter that regulates the appearance of the final image, by controlling the level of speckle. A value of $\gamma = 0$ will result in an image with almost no speckle, Fig. 3.6(c) and Fig. 3.6(d). A small value of γ is sufficient for obtaining a trade-off between the contrast enhancement and retain of speckle information in final image. As γ increases, the contrast of the image is getting closer to the values of DAS, or MV beamformed images. For this simulated medium, the choice of the parameters was influenced on offering continuity of the ventricle structures, while increasing as much as possible the contrast of the final image. USBIC BF achieve the best results with $\lambda = 50$ and $\gamma = 0.5$, while for M-USBIC we obtained the best outcome with $\lambda = 25$ and $\gamma = 0.5$.

In practical situations, the choice of the hyperparameters λ and γ may be a difficult task. When dealing with optimization problems, the parameter λ is usually employed, to balance between the prior information of the strong reflectors and the data fidelity. We may remark that in most of the optimization problems such a hyperparameter is employed. See for example the well-known Least Absolute Shrinkage and Selection Operator (LASSO) problem [Tibshirani, 1996], where such a parameter balances between the ℓ_1 and ℓ_2 norms or algorithms such as Orthogonal Matching Pursuit (OMP) [Tropp and Gilbert, 2007] (similar to our approach in the sense of the idea of minimizing a ℓ_0 pseudo norm) where the stop criterion is either the predefined number of atoms or the value of the residuals.

On the other hand, the choice of γ may depend on the application and on the necessity of visualizing the speckle noise in homogeneous regions or not. Its values are in the range [0, 1], where for 0, no influence of the beamformed data is added to the final result, while for 1 all the speckle information from the beamformed data is added to the final result. Fig. 3.7 shows how the parameters λ and γ influence the values of CNR and SNR of the beamformed image in the case of USBIC (Fig. 3.7(a) and Fig. 3.7(b)) and M-USBIC (Fig. 3.7(c) and Fig. 3.7(d)). As expected, we can observe that γ has a great influence on SNR, that is increasing with the value of γ. This is related to the fact that γ is influencing the level of speckle in the final image, by adding to the USBIC or M-USBIC beamformed image a percentage of the DAS or MV beamformed

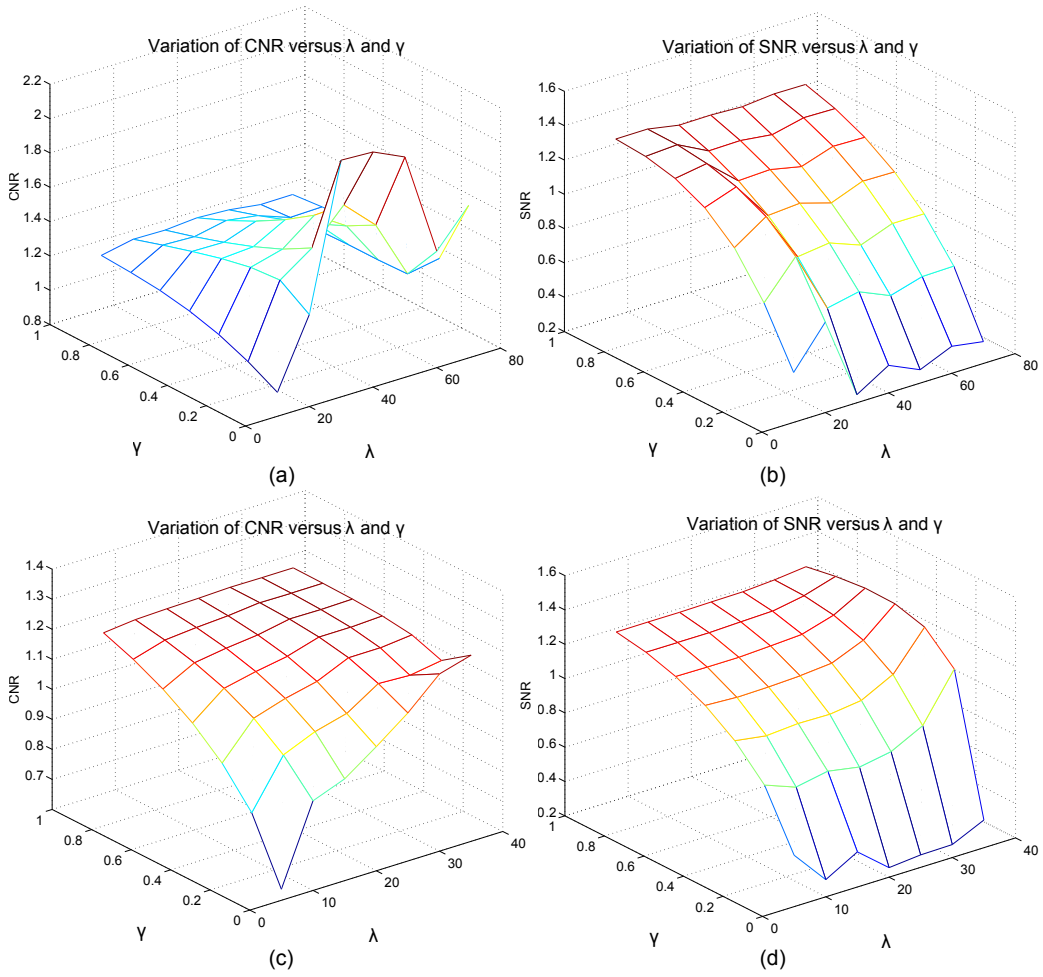

Figure 3.7: The variation of the CNR and SNR versus the parameters λ and γ when USBIC BF method ((a) and (b)), and M-USBIC BF method ((c) and (d)) are applied to the cardiac view simulation detailed in the Section 3.3.3

.

image, as discussed in the Section 3.2.3. One can observe that the value of speckle is on one hand influenced by the l_2-norm data fidelity term and on the other hand, by the hyperparameters λ and γ. However, the parameter λ has further impact on the value of CNR. For example, when applying USBIC BF, a value of $\lambda = 50$ and a low γ results in a maximum of CNR, while for the other values of λ, the CNR degrades, see Fig. 3.7(a). This is not true in the case of M-USBIC, where the influence of γ is more important that the one of λ, Fig. 3.7(c). This is due to initial decrease of the level of speckle when applying MV BF.

3.4.4 Recorded experimental data

Applied on experimental data, the results of the aforementioned BF methods are illustrated in Fig. 3.8. To calculate CR and CNR, R_1 is represented in the region surrounded by the white ellipse in the Fig. 3.8(a) and R_2 is inside the black ellipse situated at the same depth as R_1. The three black ellipses from Fig. 3.8(a) indicate the regions used to calculate the SNR. For each ellipse its corresponding SNR is calculated, the final SNR value being calculated as the average of the three values of SNR. The values of CNR and SNR for this example are resumed in the Table 3.4. Indeed, the small contrast improvement (of 0.1 dB, compared with DAS) in the case of MV may be due to the gain in resolution as stated in [Rindal et al., 2014], the level of speckle, measured by SNR, decrease. On the other hand, when using MV BF (Fig. 3.8(b)) the point-like structures are much well defined. We can observe that the tendency of the proposed method on the experimental data is to eliminate the speckle from higher depths, (Fig. 3.8(c) and Fig. 3.8(d)). As consequence, we need a relatively high value of γ in order to ensure continuity in the final image ($\gamma = 0.7$), as in the Fig. 3.8(e) and Fig. 3.8(f). Moreover, by increasing λ we can achieve better SNR while preserving a good contrast. In the case of USBIC, the beamformed image with the best trade-off between contrast and speckle preservation was obtained with $\lambda = 10$ and $\gamma = 0.7$, while M-USBIC performed better when $\lambda = 5$ and $\gamma = 0.7$.

For enforcing the previous observations, the lateral profiles are provided in the Fig. 3.9. We considered the case of USBIC with $\lambda = 10$ and $\gamma = 0.7$ (Fig. 3.8(e)), and of M-USBIC with $\lambda = 5$ and $\gamma = 0.7$ (Fig. 3.8(f)). In the case of the lateral profile that intersects the point-like reflectors, Fig. 3.9(a), we can observe that for MV and M-USBIC the scatterers are well separated, M-USBIC eliminating as much as possible

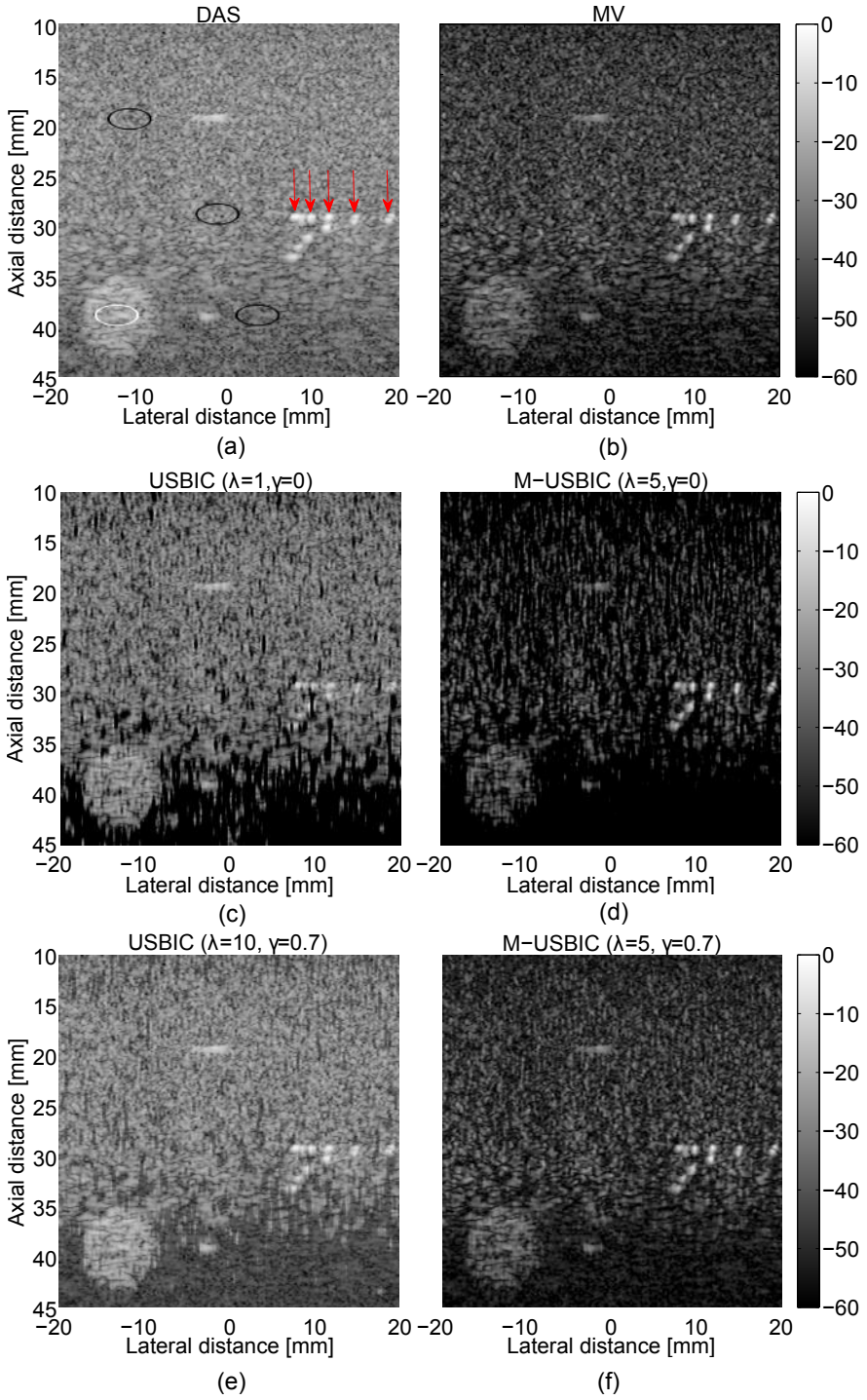

Figure 3.8: Results of (a) DAS, (b) MV, (c) USBIC with $\lambda = 1$, and $\gamma = 0$, (d) M-USBIC with $\lambda = 5$ and $\gamma = 0$, (e) USBIC with $\lambda = 10$, and $\gamma = 0.7$, and (f) M-USBIC with $\lambda = 5$ and $\gamma = 0.7$ on recorded experimental data. The image quality metrics: CR, CNR and SNR are given in the Table 3.4. In (a) we marked the regions used for the calculation of CR, CNR and SNR.

Table 3.4: CR, CNR and SNR values of the beamformed images by using the recorded experimental data, Fig. 3.8

BF method	CR [dB]	CNR	SNR
DAS	3.532	1.602	**9.745**
MV	3.641	1.085	6.443
USBIC ($\lambda = 1, \gamma = 0$)	**6.448**	1.943	7.258
USBIC ($\lambda = 10$, $\gamma = 0.7$)	5.034	**1.952**	8.702
M-USBIC ($\lambda = 5, \gamma = 0$)	4.013	1	5.408
M-USBIC ($\lambda = 5$, $\gamma = 0.7$)	4.105	1.745	9.434

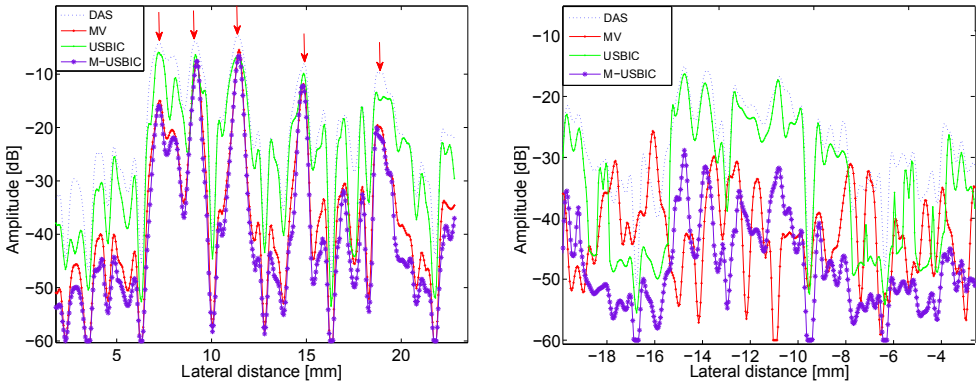

(a) (b)

Figure 3.9: Lateral profiles of the images from the Fig. 3.8. (a) The lateral profile at the axial depth of 28 mm, that intersects the point reflectors. The red arrows correspond to the point-like reflectors indicated in the Fig. 3.8(a) by red arrows. (b) The lateral profile at the axial depth of 40 mm, that intersects the massive cyst. We considered the case of USBIC with $\lambda = 10$ and $\gamma = 0.7$ (Fig. 3.8(e)), and of M-USBIC with $\lambda = 5$ and $\gamma = 0.7$ (Fig. 3.8(f)).

Table 3.5: Computational time required to beamform the images in the Fig. 3.1 and Fig. 3.8

	Computational time [min]	
BF method	**Fig. 3.1**	**Fig. 3.8**
DAS	**0.075**	**0.215**
MV	5.124	10.272
1D initialization	-	72.763
USBIC	1.725	13.532

the speckle around them. By using the proposed BF method it is possible to distinguish five point-reflectors (indicated by red arrows), while this is less evident in the case of DAS and USBIC. In the Fig. 3.9(b), the profile related to the massive cyst is more narrow than for DAS, MV and USBIC, so just the strongest reflectors inside the cyst are kept.

Even if we are able to highly improve the contrast of the final image by reinforcing the strong reflectors, the main advantage of DAS and MV over USBIC and M-USBIC is the computational time in the case when the scanned medium is not sparse, since the number of the iterations of the proposed methods increases directly with the number of the strong reflectors inside the medium. For example, to obtain the beamformed images from the Fig. 3.1, we directly applied the 2D refinement process (USBIC) to the beamformed DAS image, as described in the Section 3.2.2.2, and we obtained a computational time roughly two times lower than MV BF. The obtained values are given in the Table 3.5. However, when more complex mediums are scanned, the 1D initialization process, that is detecting the strong reflectors RF line by RF line, needs to be added to speed up the 2D refinement step. The 1D initialization, described in the Section 3.2.2.1, can be even 10 times longer than MV. However, since it is processed line by line, standard parallel computing methods could highly reduce the computational complexity. The 2D refinement method is comparable in time of computation with the MV BF. The computational time values for obtaining the beamformed images from the Fig. 3.8 are given in the Table 3.5, for the case of USBIC beamformer, and are obtained without using any parallel computing. All the discussed methods were implemented

with Matlab R2013b, on an Intel i7 2600 CPU working at 3.40GHz.

3.5 Conclusions

As first contribution, we proposed a beamforming approach based on the detection of the strong reflectors in US imaging. We validate the precision of the detection of the number and the position of the reflectors in a sparse medium, and we evaluate the proposed methods (USBIC and M-USBIC) on different types of simulated data and on experimental data. For a less sparse medium, the λ parameter is deciding the sparsity level in the final beamformed image. Our empirical experience suggests that it can be set between large intervals in a non-sparse medium. For example, by increasing the value of λ by a factor of 5, we favor the sparsity in the resulted image. After deciding the best λ in function of the desired experiment, the other parameter, γ will set the level the speckle in the final image. For non-sparse mediums, a value of γ in the interval $0.5 - 0.8$ offers the most coherent results, while enhancing the detected reflectors in the final image. Hence, the strong reflector based BF methods allow region differentiation (for example blood vessels, or cysts), while preserving speckle statistics that often contain important clinical information. The main disadvantage of the proposed methods is the high computational cost when dealing with highly non-sparse scanning mediums. We should remark that the most computational expensive step is the 1D detection of the strong reflectors. However, this step may be largely fasten by parallelly processing the RF lines. The automatic choice of the hyperparamters such as the one balancing between the data fidelity term and the sparsity of the strong reflectors, based for example on existing cross-validation techniques such as [Galatsanos and Katsaggelos, 1992] or [Ramani et al., 2012], is also a very interesting research track. Finally, the proposed approach may be improved by the use of sparse prior in appropriate bases, other than the direct strong reflection domain.

In Chapter 4 we proposed an improvement of this contribution, by modeling the raw channel data as an inverse problem, but laterally, taking into account the position of the elements of the US probe and the steering directions. This formulation allowed us to formulate a beamforming framework where the sparsity constraint term in (3.5) is modeled using some regularization techniques that take into account priors about the statistical properties of the RF signals (based on the Gaussianity assumption).

4

Beamforming through regularized inverse problems in medical ultrasound imaging

This chapter is based on the journal paper [Szasz et al., 2016b]. Part of this chapter was published in [Szasz et al., 2016d].

Contents

4.1 Introduction

With the second contribution, we proposed to perform beamforming in ultrasound imaging through a regularized inverse problem based on a linear model relating the reflected echoes to the signal to be recovered.

The work presented here uses a similar idea with multi-beam Capon (2.7.1) and IAA (2.8) of beamforming range by range. However, inspired from the source localization problems, we represent, for each range, the BF as a linear direct model relating the raw samples to the desired lateral profile of the RF image to be beamformed. This formalism allows us to invert the problem by imposing standard regularizations such as the ℓ_1 or ℓ_2-norms. These choices are motivated by the existing works in US image enhancement, that are typically based on Laplacian (e.g., [Michailovich and Tannenbaum, 2007]) or Gaussian (e.g., [Jirik and Taxt, 2008]) priors. Thus, the major contribution of this chapter is the improvement of the existing beamforming techniques by combining the proposed direct model formulated in the lateral direction of the images with a regularized inversion approach. Moreover, we incorporated the proposed method with a beamspace processing technique, in order to highly reduce the number of the required US emissions.

Firstly, Laplacian and Gaussian statistics, two of the most common regularizations in such imaging problems (including US imaging applications such as deconvolution), are considered herein, allowing the reader to observe their influence on the results. Secondly, we also applied to our framework one complex regularization method, proposed by Zou *et al.* called elastic-net regularization [Zou and Hastie, 2005]. Furthermore, our method opens new tracks for more complex regularization terms (e.g., [Chen et al., 2016a, Michailovich and Rathi, 2015]) to further improve the results. Finally, the proposed approaches, generically named Basis Pursuit beamforming (BP BF), Least Squares beamforming (LS BF), and elastic-net beamforming (EN BF) in this chapter, were evaluated using different Field II simulated data and *in vivo* carotid and thyroid experimental data. Finally we compared our BF techniques with four existing beamformers: the conventional DAS, MV, multi-beam Capon, and IAA.

Our approach presents three major advantages:

- **Flexibility**: in the choice of statistical assumptions on the signal to be beamformed (Laplacian, Gaussian, and combination of these two statistics are tested herein)

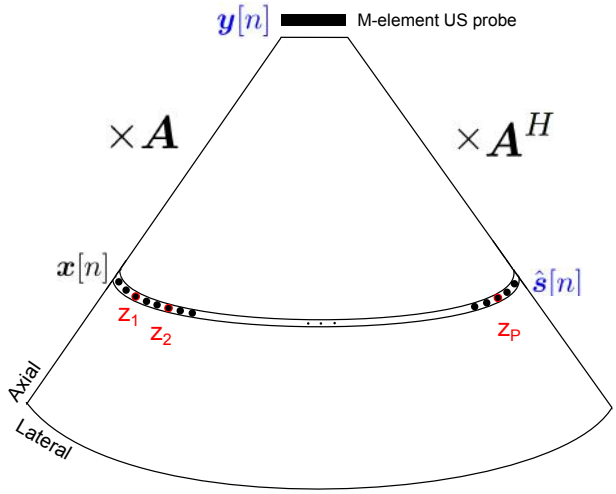

Figure 4.1: The elements used to form the proposed model.

- **Robustness**: to a reduced number of pulse emissions.
- **Robustness**: to correlation of the sources.

Thus, the proposed framework is flexible and allows for choosing the right trade-off between noise suppression and sharpness of the resulted image.

4.2 Beamforming through regularized inverse problems

4.2.1 Model formulation

The main elements used to model the proposed method are depicted in the Fig. 4.1. For sake of simplicity, let us focus our problem at a time-sample (range) n. The proposed BF method is sequentially applied in the same manner to each range. If $\boldsymbol{y}_k[n] \in \mathbb{C}^{M\times 1}$ is the raw channel data after the compensation of the time-of-flight for the k-th steering direction θ_k, we can form the steering vectors as in (2.26). Let $\boldsymbol{A}$ be the $M \times K$ steering matrix containing the steering vectors in (2.26) for all θ_k directions, $k = 1, \cdots, K$:

$$\boldsymbol{A} = [\boldsymbol{a}_{\theta_1}, \boldsymbol{a}_{\theta_2}, \cdots, \boldsymbol{a}_{\theta_K}]. \tag{4.1}$$

Note that $\boldsymbol{A}$ is known and depends on the positions of the probe elements and on the locations to beamform. Thus, it is independent on the actual positions of the reflectors.

For each range n, we want to estimate the signal corresponding to a reflector as a function of its location, that will contain dominant peaks at reflector positions. Thus, the main difference from the multi-beam Capon beamforming method is that instead of calculating the values of the weights $\boldsymbol{w}_{\theta,n}$ as in (2.28), that are further used to calculate the reflector's signal, we are directly estimating the corresponding signal by considering the raw channel data $\boldsymbol{y}_k[n]$ as observations. In other words, we want to obtain an estimate of the reflected echo $\boldsymbol{x}[n] \in \mathbb{C}^{K\times 1}$ through the observations $\boldsymbol{y}_k[n]$. Unfortunately one difficulty arises: since $\boldsymbol{y}_k[n]$ is corresponding to only one emission, modeling our problem using raw channel data as observations to estimate the reflectors, requires high computational cost, since we are dealing with multiple directions. We recall that the size of raw channel data in our problem at a range n, is $M \times K$. To overcome this issue, motivated by the results in [Malioutov et al., 2005] and [Fuchs, 1996], we propose to use the DAS beamformed data instead of the original raw channel data. In addition to data dimensionality reduction, it was shown in [Malioutov et al., 2005] and [Fuchs, 1996] that more accurate results may be achieved by proceeding in this way. Thus, we can formulate our model as follows:

$$\hat{\boldsymbol{s}}[n] = (\boldsymbol{A}^H \boldsymbol{A})\boldsymbol{x}[n] + \boldsymbol{g}[n], \tag{4.2}$$

where $\hat{\boldsymbol{s}}[n] \in \mathbb{C}^{K\times 1}$ is a lateral scanline of the DAS beamformed image formed as discussed in the Section 2.3, $\boldsymbol{A}$ is the steering matrix formed with (4.1), and $\boldsymbol{g}[n]$ an additive white Gaussian noise. If we denote by $\hat{\boldsymbol{S}}$ the DAS beamformed image of size $K \times N$, formed by juxtaposing the DAS RF lines $\hat{\boldsymbol{s}}_k$ expressed in (2.9) for all K directions, we consider $\hat{\boldsymbol{s}}[n]$ the lateral scanline from $\hat{\boldsymbol{S}}$ taken at the time-sample (range) n. Note that, since the transducers are emitting the same pulse, we assumed that $\boldsymbol{x}[n]$ which is the unknown signal, is the same for all K emissions, and for all transmitters (see, e.g., [Du et al., 2008]).

The role of the multiplication of the steering matrix $\boldsymbol{A}$ with its conjugate transpose $\boldsymbol{A}^H$ in (4.2) is to relate the position of the elements with the position of all K reflectors on a scanline. This relation is a result of considering on the one hand that the elements are impinging to the reflectors situated on the lateral scanline (the multiplication of $\boldsymbol{A}$ with $\boldsymbol{x}[n]$), while on the other hand the reflectors are impinging to the elements through their reflected pulses (the multiplication with $\boldsymbol{A}^H$). Hence, the result of the DAS beamformed scanline $\hat{\boldsymbol{s}}[n]$ is related to the unknown signal $\boldsymbol{x}[n]$ through a direct

linear model. Fig. 4.1 offers a schematic representation of our model in (4.2). Thus, after the compensation of the time-of-flight, the received raw channel data, $\boldsymbol{y}[n]$ at a range n is formed by multiplying the steering matrix $\boldsymbol{A}$ with the desired signal $\boldsymbol{x}[n]$, $\boldsymbol{y}[n] = \boldsymbol{A}\boldsymbol{x}[n]$. This multiplication could be sufficient for describing the proposed model if we are considering the raw channel data $\boldsymbol{y}[n]$, as observations. However, since we are using the DAS beamformed data instead of the original raw channel data, we further take into account the geometrical relationship between the potential sources and the elements of the probe (through the multiplication with $\boldsymbol{A}^H$).

4.2.2 Beamspace processing

In order to solve (4.2), we firstly apply beamspace processing, a common tool used in source localization approaches that reduces the computational complexity, while improving the resolution, and reducing the sensitivity to the position of the sensor (see, e.g., [Fuchs, 1996, Tian and Van Trees, 2001]). Its main purpose in US is to reduce the number of the US emissions, thus reducing the acquisition time and the computational load required by the BF process. We should note that our method of transforming the data into beamspace domain is totally different from the technique resumed in Section 2.7. The main reason is that, by using the beamspace processing presented in [Nilsen and Hafizovic, 2009], we need all the acquired raw channel data for applying beamspace processing as described in (2.22). Hence, even if on one hand, the computational complexity required by the estimated covariance matrix inversion is reduced, on the other hand, it is increased by the operations required to transform the entire set of the raw channel data into its beamspaced correspondents.

To overcome this, we based our idea on the beamspace processing techniques proposed in array processing (notably in source localization). More specifically, Malioutov *et al.* [Malioutov et al., 2005] used a method that maps the data from full dimension space of the directions (DS) into a lower dimension beamspace (BS) through a linear transform prior to source localization processing. In our case, for each range n we project the data resulted by applying DAS BF, $\hat{\boldsymbol{s}}[n]$, in BS before beamforming it through regularized inverse problems. To emphasize, $\hat{\boldsymbol{s}}[n] \in \mathbb{C}^{K\times 1}$ is projected on a lateral sampled grid of $P << K$ locations. In other words, the proposed BF method, contrarily to all the other discussed BF methods, uses only P focused emitted beams among all the K transmissions to beamform a particular lateral scanline of K samples.

Thus, the number of emissions is reduced by a factor of $\frac{K}{P}$. This will result in a reduced dimensionality of the data compared with the other BF methods, and an improved computational complexity compared with MV, multi-beam Capon, and IAA.

Let $\boldsymbol{z}[n] \in \mathbb{C}^{P\times 1}$ be the beamspace transformed vector formed by sampling the DAS beamformed lateral scanline $\hat{\boldsymbol{s}}[n]$ on a grid of P locations, see Fig. 4.1:

$$\boldsymbol{z}[n] = \boldsymbol{D}^H \hat{\boldsymbol{s}}[n], \tag{4.3}$$

where $\boldsymbol{D}$ of size $K \times P$ is the beamspace decimation matrix, that will reduce the dimensionality of a vector from $K \times 1$ to $P \times 1$. Hence, since the decimation factor is $\frac{K}{P}$, $\boldsymbol{D}$ has all elements zero, except the elements $d_{i,j}$ with $j = \frac{K}{P}i$, that will get the value 1. Similarly, the beamspaced steering matrix $\boldsymbol{A}_{BS}^H$ of size $P \times M$ is formed, composed of the P beamspaced steering vectors:

$$\boldsymbol{A}_{BS}^H = \boldsymbol{D}^H \boldsymbol{A}^H \tag{4.4}$$

Concretely, we form $\boldsymbol{A}_{BS} \in \mathbb{C}^{M\times P}$ by taking from $\boldsymbol{A}^H$ each $\frac{K}{P}$-th steering vector. So, the model formed by (4.2) after applying beamspace processing, becomes:

$$\boldsymbol{z}[n] = \boldsymbol{D}^H \hat{\boldsymbol{s}}[n] = (\boldsymbol{A}_{BS}^H \boldsymbol{A})\boldsymbol{x}[n] + \boldsymbol{D}^H \boldsymbol{g}[n], \tag{4.5}$$

where $\boldsymbol{x}[n]$ of size $K \times 1$ is the lateral profile at range n to be estimated. Thus, we can see (4.5) as an inverse problem, where $\boldsymbol{z}[n]$ is the DAS beamformed data corresponding to $P < K$ emissions, and considered as the observation data.

4.2.3 Beamforming through regularized inverse problems

Given the ill-posedness of the direct model in (4.5), we propose hereafter to invert it using standard regularization techniques. For achieving this, a cost function, denoted by $J(\boldsymbol{x}[n])$, consisting into the linear combination of two terms is considered. The first term, denoted by $J_1(\boldsymbol{x}[n])$, represents the data attachment, while the second, denoted by $J_2(\boldsymbol{x}[n])$, is the regularization prior:

$$J(\boldsymbol{x}[n]) = J_1(\boldsymbol{x}[n]) + \lambda J_2(\boldsymbol{x}[n]), \tag{4.6}$$

where λ is a scalar, called regularization parameter, that adjusts the trade-off between the fidelity to the data and the regularization term. A large λ will strongly favor the a

priori about $\boldsymbol{x}[n]$, while a small λ gives a high confidence to the observations. Keeping in mind that the additional noise in (4.5) is Gaussian, the data attachment term is expressed by an ℓ_2-norm, giving the following cost function:

$$J(\boldsymbol{x}[n]) = ||\boldsymbol{z}[n] - (\boldsymbol{A}_{BS}^H \boldsymbol{A})\boldsymbol{x}[n]||_2^2 + \lambda J_2(\boldsymbol{x}[n]). \tag{4.7}$$

In this work, the choice of the regularization term $J_2(\boldsymbol{x}[n])$ is guided by the existing literature on statistical modelling of US images, previously applied to various applications such as image deconvolution (e.g., [Michailovich and Tannenbaum, 2007, Yu et al., 2012]). It has thus been shown that Laplacian and Gaussian statistics are well adapted to model US images. For this reason, we give in the two following paragraphs the mathematical derivations and beamforming results using ℓ_1-norm (the sum of absolute difference) and ℓ_2-norm (or the Euclidean norm, that is the sum of squared difference) regularization terms. We should note that while the first will promote sparse solutions, the latter will promote smoother results.

The choice of a quadratic data fidelity term is related to the additive zero-mean Gaussian assumption on the noise. We emphasize that the noise considered in this work is different from the multiplicative speckle noise generally assumed to affect envelope images in ultrasound imaging. Instead, the additive noise considered in this work affects the RF data and is caused by the acquisition process. The same model has been previously used by several authors (e.g., [Michailovich and Tannenbaum, 2007] and [Du et al., 2008]).

4.2.3.1 Laplacian statistics through Basis Pursuit (BP)

Considering that the signal $\boldsymbol{x}[n]$ to be beamformed follows Laplacian statistics, the minimization of the cost function in (4.7) turns into the optimzation procedure in (4.8), usually called Basis Pursuit (BP) in the literature [Chen et al., 1998].

$$\boldsymbol{x}_{BP}[n] = \underset{\boldsymbol{x}[n]}{\operatorname{argmin}}(||\boldsymbol{z}[n] - (\boldsymbol{A}_{BS}^H \boldsymbol{A})\boldsymbol{x}[n]||_2^2 + \lambda||\boldsymbol{x}[n]||_1), \tag{4.8}$$

where $||\cdot||_1$ denotes the ℓ_1-norm. The minimization problem (4.8) is convex, hence continuous, and has one global minima for any $\lambda > 0$.

Herein, we used the well-known YALL1 to solve (4.8) [Zhang, 2009], a software package that contains implementation of alternating direction method (ADM), that

solves also BP. A comparison of the six most used BP implementations is done in [Lorenz et al., 2015] and three of them were also compared in [Huang et al., 2010] with application in underwater acoustics, where is shown that YALL1 gives best performances for real-time applications.

4.2.3.2 Gaussian statistics through Least Squares (LS)

To achieve smooth solutions of the proposed BF method, we modeled our problem with an ℓ_2-norm based minimization function, and we used the Tikhonov regularized least-squared method (or rigid regression) for solving it [Tikhonov, 1963]. The cost function is of the form:

$$\boldsymbol{x}_{LS}[n] = \underset{\boldsymbol{x}[n]}{\operatorname{argmin}}(||\boldsymbol{z}[n] - (\boldsymbol{A}_{BS}^H \boldsymbol{A})\boldsymbol{x}[n]||_2^2 + \lambda||\boldsymbol{x}[n]||_2^2), \tag{4.9}$$

where $||\cdot||_2$ denotes the ℓ_2-norm. For solving (4.9) we used its analytical solution:

$$\boldsymbol{x}_{LS}[n] = ((\boldsymbol{A}_{BS}^H \boldsymbol{A})^H (\boldsymbol{A}_{BS}^H \boldsymbol{A}) + \lambda \boldsymbol{I}_{K\times K})^{-1} (\boldsymbol{A}_{BS}^H \boldsymbol{A})^H \boldsymbol{z}[n], \tag{4.10}$$

where $\boldsymbol{I}_{K\times K}$ denotes the identity matrix of size $K \times K$.

In order to obtain the BP and LS beamformed images, for each time sample n, with $n \in \{1, \ldots, N\}$, we estimate its corresponding lateral scanline $\boldsymbol{x}_{BP}[n]$ (using BP BF method) or $\boldsymbol{x}_{LS}[n]$ (using LS BF method), and we are juxtaposing all the obtained scanlines, in the axial direction of the image.

4.2.3.3 Elastic-net (EN) regularization

In the following, we propose to solve the ill-posed inverse problem in (4.7) using the following regularization referred to as elastic-net (EN) regularization:

$$\begin{aligned} \boldsymbol{x}_{EN}[n] = \underset{\boldsymbol{x}[n]}{\operatorname{argmin}}(&||\boldsymbol{z}[n] - (\boldsymbol{A}_{BS}^T \boldsymbol{A})\boldsymbol{x}[n]||_2^2 \\ &+ \gamma(||\boldsymbol{x}[n]||_2^2 + \epsilon||\boldsymbol{x}[n]||_1)), \end{aligned} \tag{4.11}$$

where $||\cdot||_1$ and $||\cdot||_2^2$ denote the ℓ_1, respectively ℓ_2-norms. In our experiments, in order to decrease the number of hyperparameters to tune, we considered $\gamma\epsilon = (1-\gamma)$, turning the regularization term in (4.11) into:

$$pen(\boldsymbol{x}[n]) = \gamma||\boldsymbol{x}[n]||_2^2 + (1-\gamma)||\boldsymbol{x}[n]||_1, \tag{4.12}$$

where $pen(\boldsymbol{x}[n])$ is the penalization term that influences the sparsity of the result. Thus, for $\gamma = 0$ the problem turns into a basis pursuit algorithm, while when $\gamma = 1$ we obtain the Tikhonov regularization. In the following, let us denote by $\boldsymbol{\Psi} \in \mathbb{C}^{P \times K}$ the measurement matrix formed as $\boldsymbol{\Psi} = \boldsymbol{A}_{BS}^T \boldsymbol{A}$. Moreover, we define by S_γ the soft thresholding operator, having the following function for any $\gamma > 0$:

$$S_\gamma(t) = \begin{cases} t - \frac{\gamma}{2}, & \text{if t} < \frac{\gamma}{2} \\ 0, & \text{if } \mid t \mid \leq \frac{\gamma}{2} \\ t + \frac{\gamma}{2}, & \text{if t} < -\frac{\gamma}{2} \end{cases} \tag{4.13}$$

Algorithm 2, based on [Mosci and Rosasco, 2010], describes the main steps used to minimize the function in (4.11). We remind that this optimization is done independently, range by range, resulting into the consecutive lateral profiles of the final beamformed image.

Input: γ, $\boldsymbol{z}[n]$,$\boldsymbol{\Psi}$
Output: $\boldsymbol{x}^p[n]$
initialization: $\boldsymbol{x}^0[n] = \mathbf{0}$
// damping factor:
$\tau = \frac{1}{2-\gamma}$
// fix the step size using the matrix 2-norm of $\boldsymbol{\Psi}\boldsymbol{\Psi}^T$:
$\delta = \frac{1}{\text{normest}(\boldsymbol{\Psi}\boldsymbol{\Psi}^T) \times 1.1}$
while *convergence not reached* **do**
  $p := p + 1$;
  $\boldsymbol{x}^p[n] = \tau S_{\gamma K \delta}(\boldsymbol{x}^{p-1}[n] + \delta \boldsymbol{\Psi}^T(\boldsymbol{z}[n] - \boldsymbol{\Psi}\boldsymbol{x}^{p-1}[n]))$;
end

Algorithm 2: Elastic-net beamforming of one lateral profile via Iterative Soft Thresholding.

4.3 Experiments

Table 4.1: Parameters of simulated and experimental images

Parameters for simulation of:	Scatterers **Fig. 4.2**	Scatterers **Fig. 4.4**	Cyst **Fig. 4.6**	Cardiac image **Fig. 4.9**	Carotid **Fig. 4.10**	Thyroid **Fig. 4.12**
Transducer						
Transducer type			Linear array			
Transducer element pitch [μm]	256	231	256	192.5	110	120
Transducer element kerf [μm]	20	38.5	20	38.5	25	
Transducer element height [mm]	5	14	5	14	4	
Central frequency, f_0 [MHz]	3	4	3	4	7	7.2
Sampling frequency, f_s [MHz]	100	100	40	40	40	
Speed of sound, c [m/s]				1540		
Wavelength [μm]	513.3	385	513.3	385	220	
Excitation pulse				Two-cycle sinusoidal at f_0		
Synthetic Aperture Emission						
Receive Apodization				Hanning		
Number of transmitting elements	64	64	64	64	128	128
Number of receiving elements	64	64	64	64	128	128
Number of emissions (K)	260	260	260	204	192	312
The values of λ (in the case of BP and LS BF)						
BP	0.5	-	0.5	0.2	0.5	5
LS	0.7	-	1	0.5	1	1

For evaluating the proposed BP BF and LS BF approaches, we considered different types of simulated and experimental data. We compared our BF results with DAS (Section 2.3), MV (Section 2.4.1), multi-beam Capon (Section 2.7.1), and IAA (Section 2.8) BF methods. The simulations were made using the Field II program (see e.g., [Jensen and Svendsen, 1992] and [Jensen, 2004]). The first simulation include a sparse medium, the second one contains a circular hypoechoic cyst in a medium with speckle, and the third one contains in a simulation of the Short Axis (SAx) view of a cardiac image, as suggested in [Alessandrini et al., 2012]. The first experimental data consists in a carotid that was recorded with an Ultrasonix MDP research platform. Finally, the second experimental data contains a thyroid medium with a malignant tumor. The thyroid data was recorded with the Sonoline Elegra clinical scanner, modified for research purpose. The parameters of the simulated and experimental data are presented in the Table 4.1. Note that for MV and multi-beam Capon beamformers, spatial and temporal averaging, as well as diagonal loading technique are used for the estimation of the covariance matrix, as discussed in the Section 2.4.1.

To evaluate the EN method, we considered two cases: one that contains simulated data of point reflectors and an experiment that uses *in vivo* data of the healthy thyroid. We compared our method with DAS, MV, BP and LS in the case of sparse medium, and with DAS, BP, and LS in the case of *in vivo* data. The aim of this simulation is to accentuate the differences with the BP and LS beamformers.

An important aspect is that, when applying BP, LS, and BF methods, five times ($\frac{K}{P} = 5$) less emissions were used in the beamforming process, by applying the beamspace processing presented in the Section 4.2.2. This hangs on for all the examples we are presenting in this chapter. For these examples, reducing five times the US transmissions is optimal in terms of gain in resolution, while reducing computational time.

The values of the regularization parameter λ for all the presented examples when using BP and LS are grouped in the Table 4.1. The optimal value of λ was chosen manually. We emphasize that this was the case for all hyperparameters of all comparative methods. Several studies exist in the literature for automatic estimation of the regularization hyperparameter (e.g., [Chen et al., 2015, Galatsanos and Katsaggelos, 1992, Ramani et al., 2012]) that can improve the robustness of the proposed methods, at increased computational cost. Nonetheless, their implementation is beyond the scope of this chapter.

4.3.1 Parameters for the comparative methods

The results of MV beamforming were obtained by using the implementation described in [Asl and Mahloojifar, 2009]. The length of the spatial averaging window, L was defined as half of the number of the probe's elements, i.e. $L = \frac{M}{8}$. A temporal window of 10 samples was used in our examples and the diagonal loading parameter was fixed to $\Delta = \frac{1}{10L}$. The adaptive coherence method was applied to the MV BF method.

The results of multibeam-Capon were obtained by using the multi-beam approach suggested in [Jensen and Austeng, 2012]. The K emissions were uniformly distributed between $\pm 30°$. The beamspace transform down to 33 dimensions was applied, able to retain the variance for incoming narrowband far-field signals. The diagonal loading factor was set to 0.01.

Finally, for IAA implementation we used the source code provided by the authors in [Jensen and Austeng, 2014]. The number of iterations was set to 15 for our examples.

Note that for all the comparative methods, several parameters need to be carefully tuned in order to obtain acceptable results. However, using the proposed approach, only the regularization hyperparameter λ needs to be set.

4.3.2 Simulated point reflectors

The medium for evaluation of BP and LS BF methods contains 5 point reflectors, 4 of them aligned in pairs of 2 and separated by 4 mm, and the other laterally centered at 0 mm. They are located at axial depths ranging from 63 to 68 mm, with a transmit focus at 65 mm and a dynamic receive focalisation.

The medium for evaluation of EN BF method contains 8 point reflectors arranged between 35 mm and 55 mm in depth. Two of them are laterally centered at 0 mm, with axial position at 40, respectively 45 mm. Three others are vertically aligned at -5 mm, with axial positions at 35 mm, 45 mm, respectively 55 mm. Finally, the last three point reflectors are vertically aligned at lateral position 5 mm, with axial positions of 35 mm, 45 mm, respectively 55 mm.

4.3.3 Simulated phantom data

To evaluate the accuracy, contrast and resolution of the aforementioned beamformers, a hypoechoic cyst of radius 5 mm, located at the depth 80 mm, in a speckle pattern. The

speckle pattern contains 50000 randomly placed scatterers, with Gaussian distributed amplitudes. This example was inspired from the simulation of a synthetic kidney example included in Field II software. The attenuation was not taken into account.

4.3.4 Simulated cardiac image

The SAx view is the cross-sectional view of the heart and is a well exploited perspective in echocardiography, containing information about the left ventricle (LV) and right ventricle (RV). In our simulation we visualize the LV. The transmit focus point is set at 65 mm. The final image is ultra-realistic, the amplitudes being related to an *in vivo* cardiac image [Alessandrini et al., 2012]. The number of scatterers was sufficiently large to produce fully developed speckle.

4.3.5 *In vivo* data: carotid

The carotid ultrasound is a common procedure used to detect strokes or the risk of strokes due to the narrowing of the carotid arteries. The data was acquired from a healthy subject, with the Ultrasonix MDP research platform, attached with the parallel channel acquisition system, SonixDAQ. The linear ultrasonic probe L14-W/60 Prosonic© (Korea) of 128 elements was used.

4.3.6 *In vivo* data: thyroid

The thyroid ultrasound is done to visualize the thyroid gland to detect possible tumors or deformations. Two sets of data were acquired: first one, from a subject with a tumor and the other one from a healthy subject. For both acquisitions we used the clinical Sonoline Elegra ultrasound system modified for research purposes, and a 7.5L40 P/N 5260281-L0850 linear array transducer of Siemens Medical Systems, having the characteristics described in Table 4.1.

4.4 Results and Discussion

This section presents the results of applying the proposed methods on both simulated and *in vivo* data. Three conventional image quality metrics were calculated: CNR, SNR, and RG. They were computed based on the envelope-detected signals independent of image display range. Their definition is given in Section 1.2.3.

4.4.1 Individual point reflectors

With this simulation we evaluate the potential of the proposed methods in sparse mediums. The resulted beamformed images are illustrated in the Fig. 4.2. The result of DAS BF is shown in Fig. 4.2(a). Using the MV BF, the lateral resolution is improved compared with DAS, IAA, and LS BF (see Fig. 4.2(b)), and it is comparable with the result of multi-beam Capon BF, Fig. 4.2(c). Concerning the IAA beamformed result, as stated in [Jensen and Austeng, 2014], it gives better point-target resolvability than DAS, Fig. 4.2(d). The proposed BP BF have the best resolution of the point-like reflectors, being able to perfectly detect the 5 reflectors, by obtaining the most narrower mainlobes, due to the fact that BP results in a sparse representation of the beamformed signals, Fig. 4.2(e). As expected, LS beamformer results in solutions that tend to be smooth and regular, as in the Fig. 4.2(f).

Fig. 4.3 presents the lateral profiles of the compared BF methods at 65 mm. We can observe that multi-beam Capon and MV are comparable in terms of lateral profiles, but MV offers better delimitation of the two points. As observed, BP BF outperforms the other BF methods, being able to perfectly resolve the two points, suppressing also the sidelobes. Finally, LS BF gives the smoothest result.

The beamformed images for evaluating EN beamformer are depicted in the Fig. 4.4. DAS BF (Fig. 4.4(a)) results in low lateral resolution, further improved by MV BF (Fig. 4.4(b)). However, the best resolution of the target points is offered by the BP BF (Fig. 4.4(c)) that perfectly detects the 8 reflectors. This observation is in coherence with the fact that BP privileges sparsity in the results, through the Laplacian statistics. LS BF (Fig. 4.4(d)) results in smoother solutions compared with BP BF, but with better lateral resolution than MV. As expected, EN with $\gamma = 0.8$ (Fig. 4.4(e)) produces results similar with LS BF, since the hyperparameter γ decides the level of smoothness of the solutions, weighting the term related to ℓ_2-norm. Contrarily, EN with $\gamma = 0.2$ (Fig. 4.4(e)) tends to the solution of BP BF. Note that for each simulation, γ has been set empirically to its best value.

The remarks above are confirmed by the Fig. 4.5 showing the lateral variation of the beamformed responses at depth 45 mm. BP BF have the narrower mainlobes, offering the best delimitation of the points. However, the two cases of EN BF are presenting

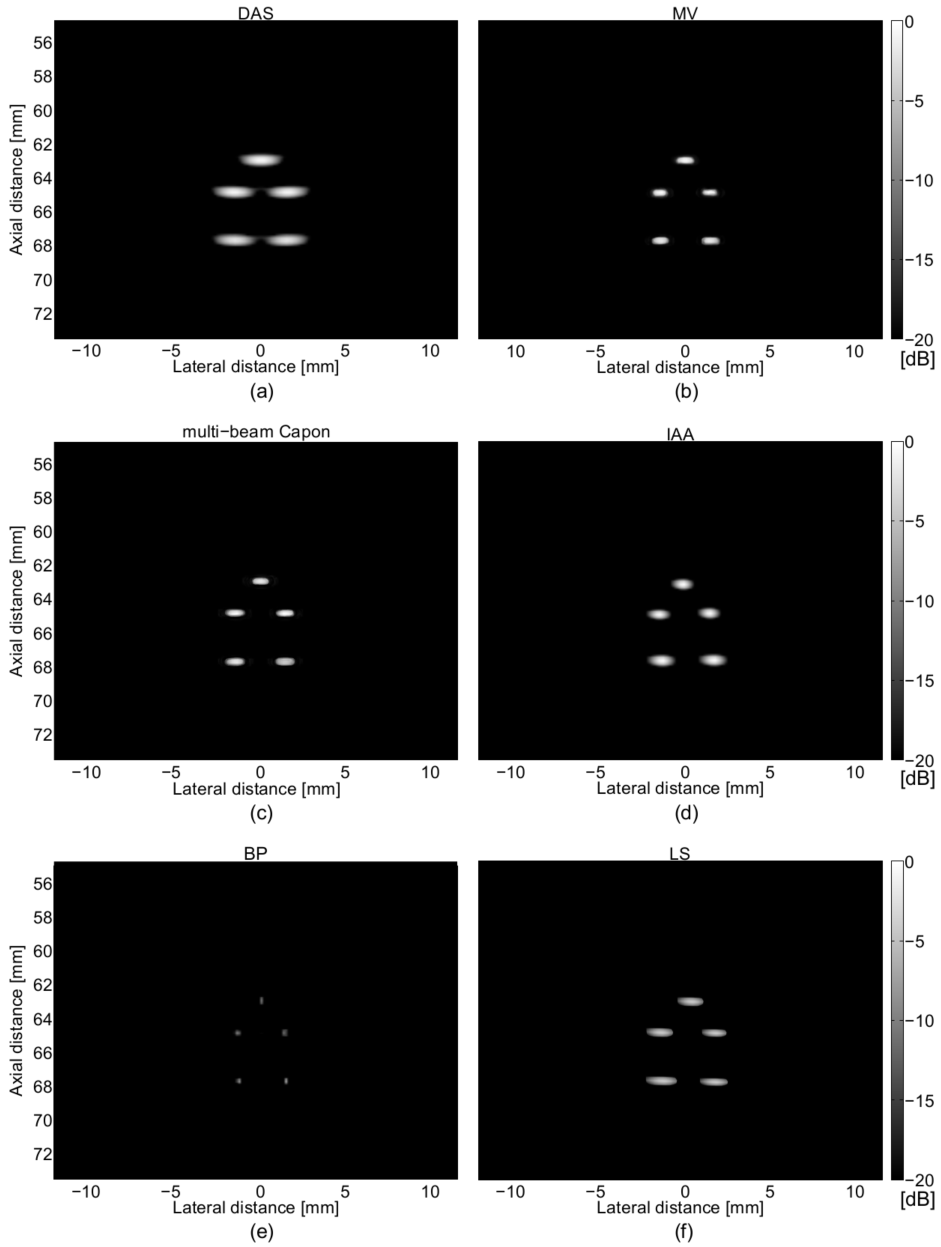

Figure 4.2: (a) DAS, (b) MV, (c) multi-beam Capon, (d) IAA, (e) BP, and (f) LS BF results of the simulation of individual point scatterers.

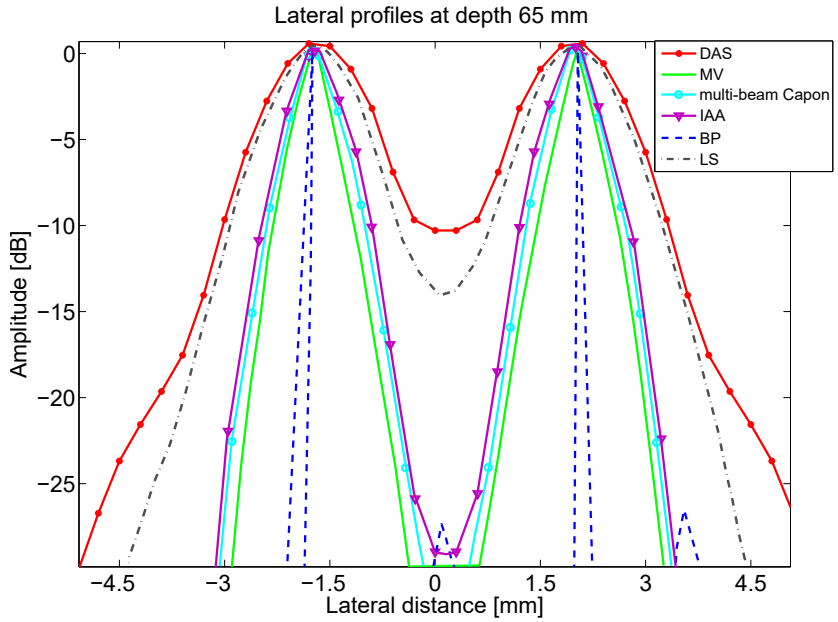

Figure 4.3: Lateral profiles at 65 mm depth of the point reflectors represented in Fig. 4.2.

results that are varying between BP and LS, but with better spatial resolution of the target points than DAS and MV.

4.4.2 Simulated hypoechoic cyst

The BF results of a hypoechoic cyst in a speckle pattern are shown in the Fig. 4.6. We have highlighted with white circle the true borders of the cyst, in order to show the accuracy of the proposed methods regarding the dimensionality of the scanned structures.

The image quality metrics are detailed in Table 4.2. To calculate the CNR, we have considered the region R_2 inside the hypoechoic cyst (the black region), and the region R_1 inside the homogeneous speckle, at the same depth and with same dimension as the region R_2, as suggested in [Rindal et al., 2014]. The SNR was computed for R_1. For calculating RG, the whole image was considered. As expected, with DAS the cyst appears more narrow due to the low resolution and its low capability of resolving cyst-like structures inside the speckle pattern, Fig. 4.6(a). By using MV, we slightly increase the contrast and the resolution in the final image compared with DAS, the dimension of the cyst being closer to its real dimension, as shown in Fig. 4.6(b). Better

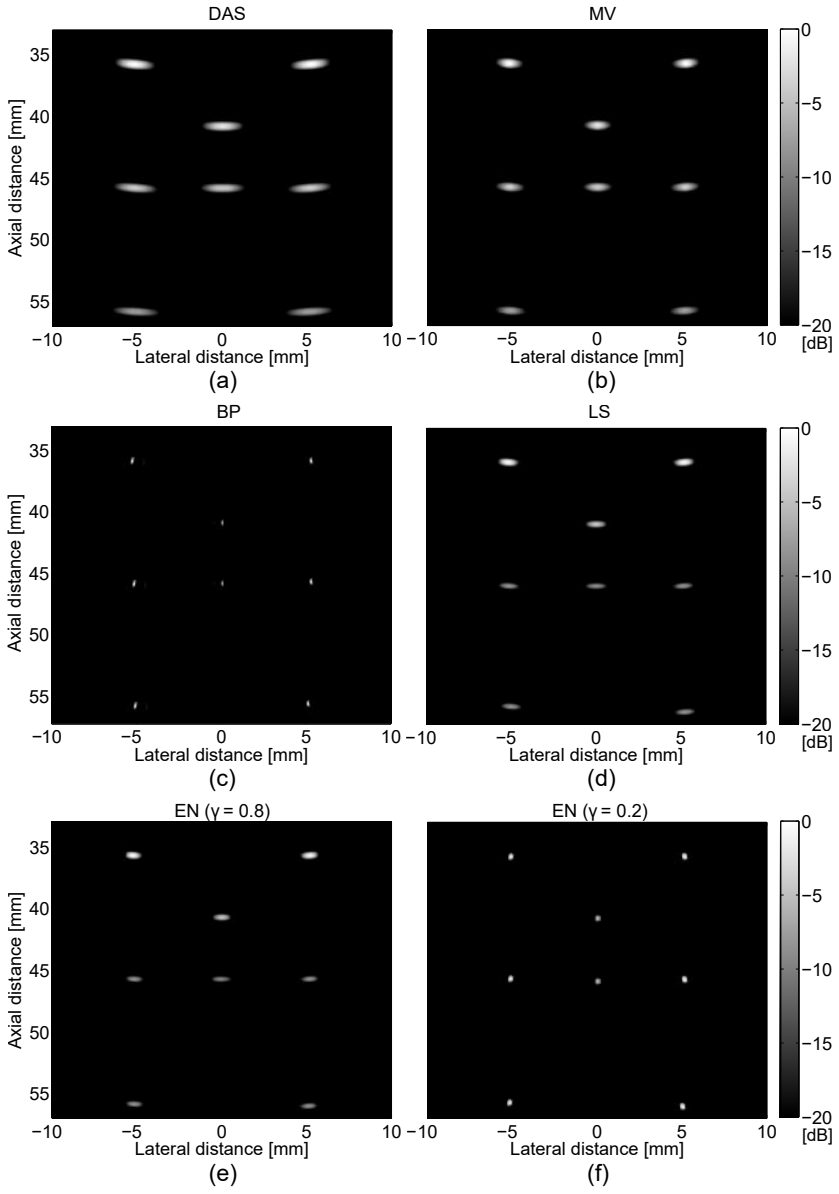

Figure 4.4: (a) DAS, (b) MV, (c) BP, (d) LS, (e) EN ($\gamma = 0.8$), and (f) EN ($\gamma = 0.2$) BF results of a sparse medium.

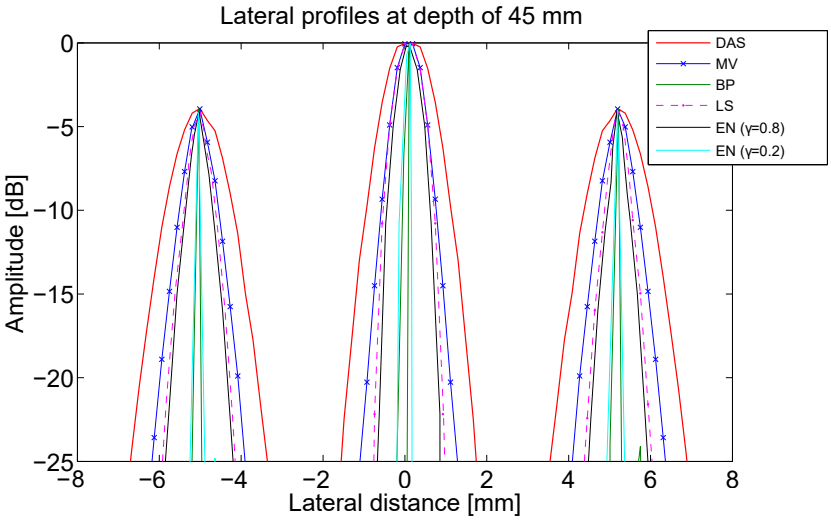

Figure 4.5: Lateral profiles of Fig. 4.4 at depth 45 mm.

Table 4.2: CNR, SNR, and RG values for the simulated phantom in Fig. 4.6

BF Method	**CNR**	**SNR**	**RG**
DAS	4.8	0.4	1
MV	5.3	0.61	3.64
multi-beam Capon	5.4	0.58	4.87
IAA	3.5	0.63	3.57
BP	6.5	0.62	**8.72**
LS	**7.4**	**0.68**	2.65

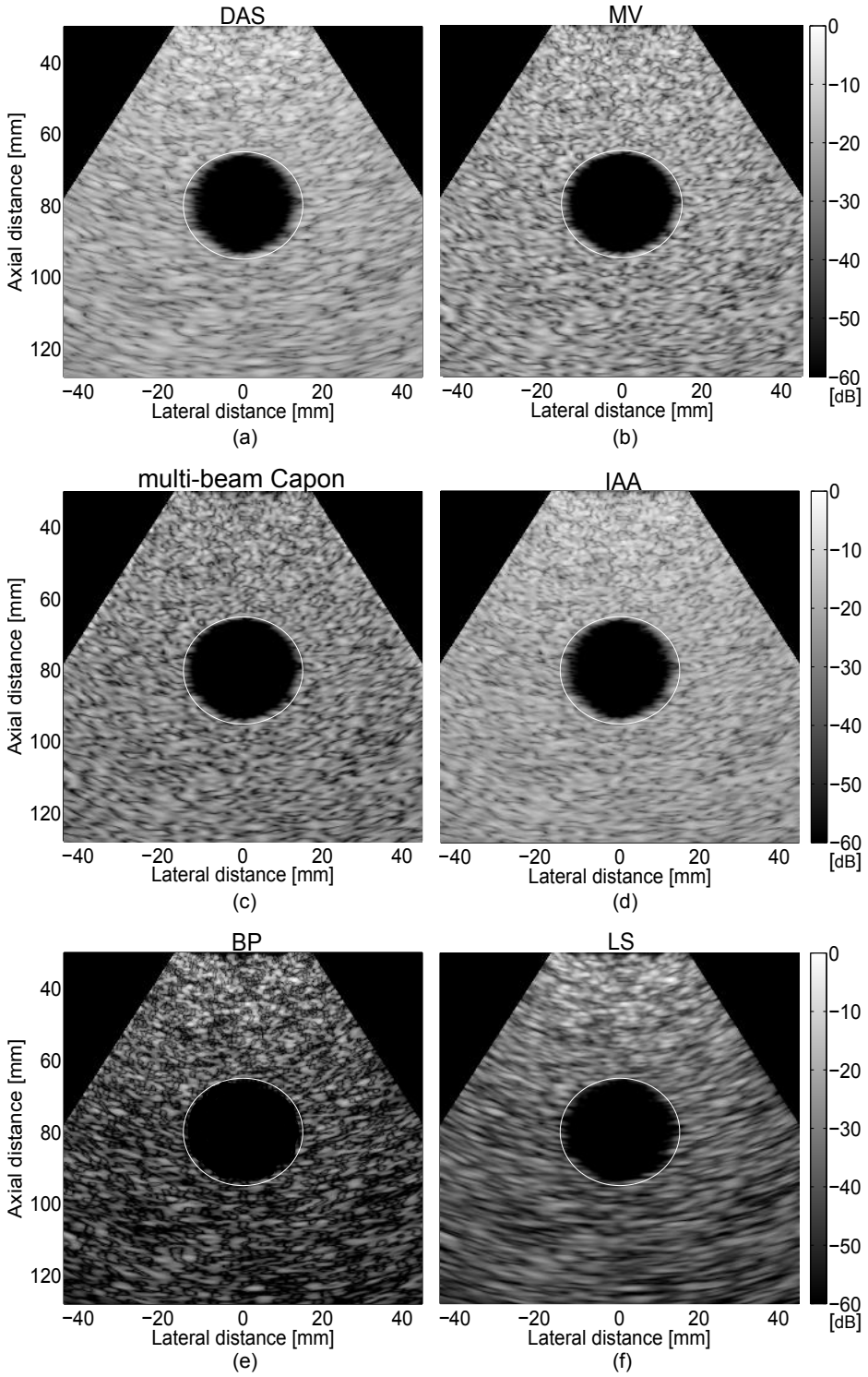

Figure 4.6: (a) DAS, (b) MV, (c) multi-beam Capon, (d) IAA, (e) BP, and (f) LS BF results of the hypoechoic cyst simulation.

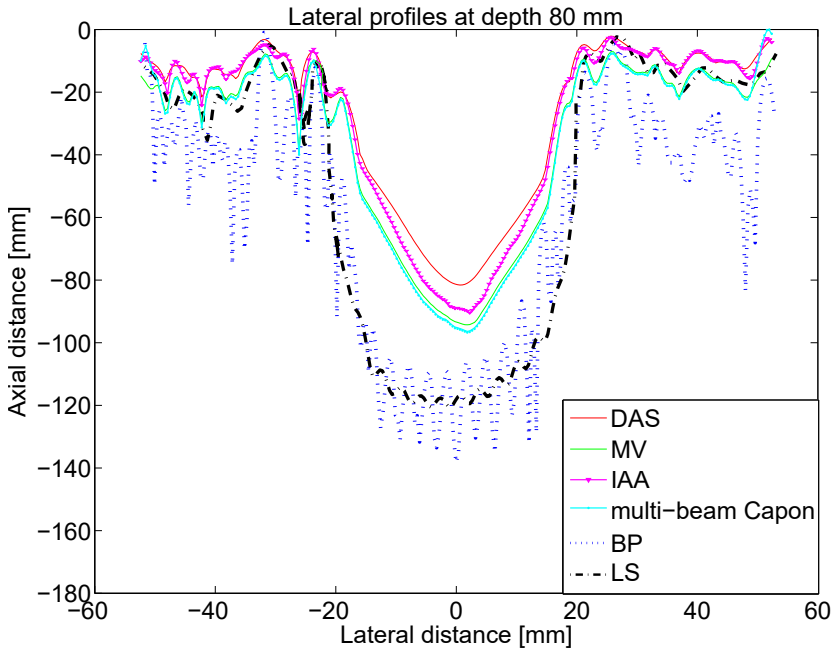

Figure 4.7: Lateral profiles at 80 mm depth of the cyst phantom represented in Fig. 4.2.

resolution is obtained when the multi-beam Capon is used, the RG being increased by a factor of almost 1.4. The improve in resolution can be observed also in the delimitation of the cyst region compared with the white circle that represents the real dimension of the cyst, see Fig. 4.6(c). Compared with DAS, IAA increases the resolution of the beamformed image, but not as much as MV or multi-beam Capon, Fig. 4.6(d). However, a contrast degradation can be observed from Table 4.2. Finally, the proposed methods are reflecting more correctly the real dimension of the cyst, especially when using the BP BF, Fig. 4.6(e), this being in concordance with the high increase in resolution (with a factor of 2 compared with MV) and contrast. As expected, LS tends to favor continuity and smoothness, especially when dealing with the speckle pattern (see Fig. 4.6(f)), the gain in resolution being less important. However, even so, it is more precise in reflecting the dimensionality of the cyst. Note that in terms of SNR, in comparison with DAS, all the other beamformers give better SNR, the best improvement being obtained with LS BF which is also outperforming the other beamformers in terms of contrast.

Fig. 4.7 presents the lateral profiles of the results presented in the Fig. 4.6, where the previous observations are confirmed. The curves in Fig. 4.7 are computed by averaging

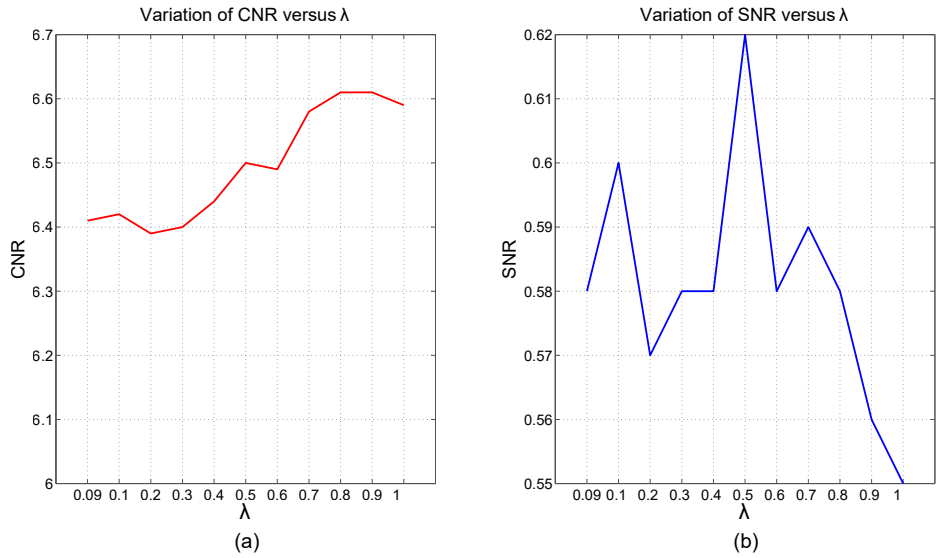

Figure 4.8: The variation of (a) CNR and (b) SNR versus λ when BP method was applied to the hypoechoic cyst simulation.

15 lateral profiles around depth 80 mm. The proposed methods, BP and LS, have larger mainlobes than the other BF methods, that correspond to the true dimension of the hypoechoic cyst. We can also confirm the increase in contrast presented in the Table 4.2 in case of BP and LS BF approaches.

Fig. 4.8 presents the variation of CNR and SNR parameters function of λ hyper-parameter. We can observe that a favorable compromise between CNR and SNR is reached when $\lambda = 0.5$. The value of CNR can be improved by increasing the value of λ. For example, when $\lambda = 0.9$, CNR= 6.61, but the value of SNR is reduced, SNR= 0.55. Similarly, decreasing the value of λ will increase the value of SNR, while losing in CNR.

4.4.3 Simulated cardiac image

The results of beamforming the cardiac medium are shown in the Fig. 4.9. With this example, we are interested in visualizing the LV region (hypoechoic), which is surrounded by the hyperechoic regions containing the anterior and posterior walls of the heart as well as the septum. The small echoic regions inside the LV region are the papillary muscles, that due to the low contrast and resolution of the DAS beamformed image are hard to be distinguished, Fig. 4.9(a). A better visualization of the walls is obtained with MV (Fig. 4.9(b)) and multi-beam Capon (Fig. 4.9(c)), resulting also in an improved

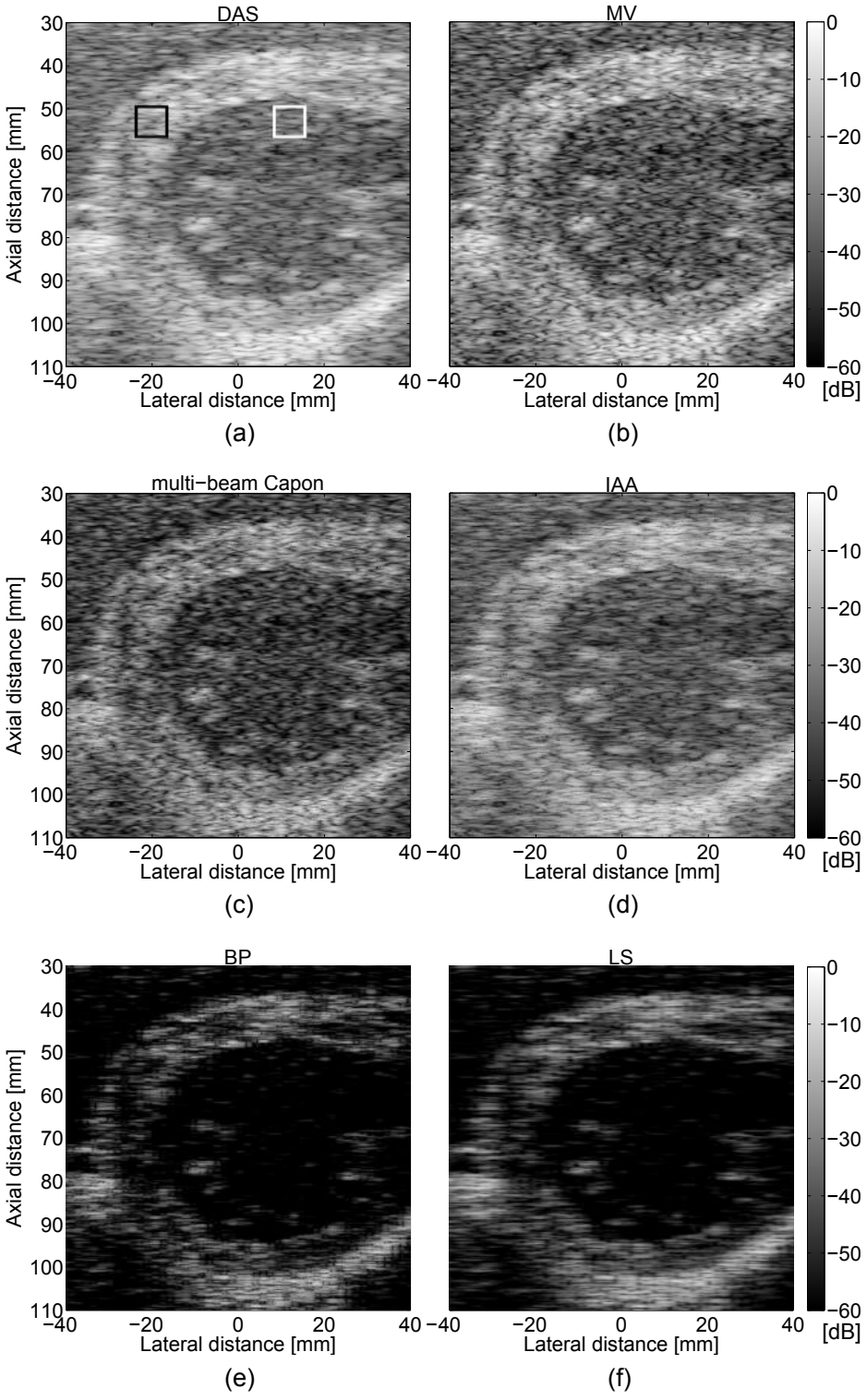

Figure 4.9: (a) DAS, (b) MV, (c) multi-beam Capon, (d) IAA, (e) BP, and (f) LS BF results of the ultrarealistic simulation of a cardiac image.

Table 4.3: CNR, SNR, and RG values for the simulated US cardiac beamformed images in Fig. 4.9

BF Method	**CNR**	**SNR**	**RG**
DAS	1.12	0.47	1
MV	0.90	0.56	3.56
multi-beam Capon	0.61	0.54	4.23
IAA	1.30	0.62	5.3
BP	1.45	1.75	**9.89**
LS	**1.55**	**1.88**	2.06

resolution, confirmed with a higher RG value (see Table 4.3). For the calculation of the CNR, we considered R_1 the region inside the white square, situated at approximately 18 mm (laterally) and around 55 mm (axially), while R_2 is delimited by the black square, around -20 mm (laterally) and 55 mm (axially). To compute SNR, the R_1 region was considered.

An interesting observation is that the value of the CNR in the case of MV and multi-beam Capon is not improved compared with DAS. This is explained by the results in [Rindal et al., 2014], where it has been shown that the improvement of the contrast directly depends on the high definition of the regions (the LV, the septum, and the walls in our example). Since the amplitude of the reflectors from the walls and septum are not so high compared with the region of LV that contains speckle, the contrast of the final image is affected. However, IAA improve both the contrast and the resolution of the image, presenting more defined regions, as shown in Fig. 4.9(d). Yet, the best improvement of the resolution is obtained when we promote Laplacian BF solutions, with BP BF, see Fig. 4.9(e), resulting in an improvement by a factor of 2 in RG compared with MV and multi-beam Capon, and by a factor of almost 10 compared with DAS. Of course, as expected, LS BF is highly improving the contrast and the SNR of the resulted image, while the RG is lower than when using the other BF approaches, Fig. 4.9(f).

4.4.4 *In vivo* data: carotid

Fig. 4.10 presents the BF results of the studied beamformers, and in the Table 4.4 we calculated their corresponding CNR, SNR, RG, and computational time values. In this

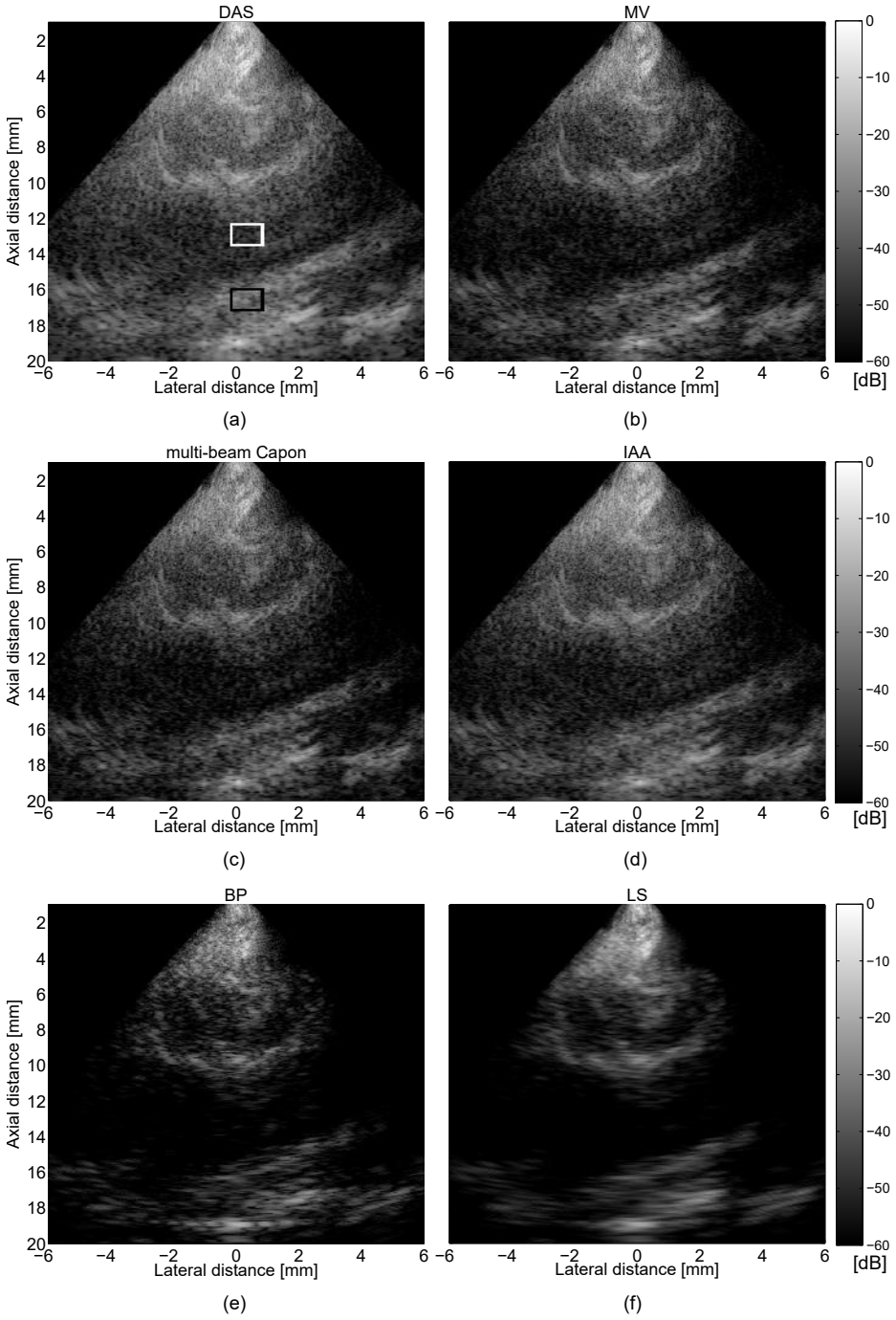

Figure 4.10: (a) DAS, (b) MV, (c) multi-beam Capon, (d) IAA, (e) BP, and (f) LS BF results of experimental carotid data.

Table 4.4: CNR, SNR, RG, and computational time values for the experimental carotid beamformed images from Fig. 4.10

BF Method	**CNR**	**SNR**	**RG**	Computation time [s]
DAS	1.84	1.46	1	**4.5552**
MV	2.24	1.43	1.25	122
multi-beam Capon	1.32	1.49	1.25	368
IAA	1.48	1.47	1.34	8.9266
BP	1.85	1.49	1.48	60.4320
LS	**1.94**	**1.55**	1.17	8.8692

example, the carotid is placed between 8 and 15 mm in the axial direction. In this region, the interior of the carotid artery is the hypo-echoic structure surrounded by the arterial walls (which are hyper-echoic). To calculate the CNR, we have considered region R_2 inside the carotide (the white rectangle positioned at 0 mm laterally), and the region R_1 inside the region of speckle (the black rectangle positioned at 0 mm laterally). The SNR for R_1 was computed.

As observed, by using DAS BF is hard to distinguish between the interior of the carotid and its walls, Fig. 4.10(a). This can be also explained by the fact that DAS BF result represents the lower RG. A better visualization of the structures of interest are obtained with MV and multi-beam Capon, that have similar RG values. However, the contrast of the MV beamformed image is better, increasing the value of CNR by a factor of ≈ 1 compared to multi-beam Capon. We can observe that multi-beam Capon is clearly defining the region inside the carotid, by reducing the level of speckle inside it, cf. Fig. 4.10(c). The IAA beamformed image is comparable with the one of multi-beam Capon, but it conserves better the speckle inside the carotid, offering a better resolution and a better contrast of the image. With the proposed approaches, however we are able to better distinguish the interior of the carotid artery, as well as its walls, with a high gain in contrast and resolution resulted by applying BP BF. A loss in resolution can be observed when using LS, compared with BP, due to the use of the ℓ_2-norm regularization. Note that, due to the formulation of the proposed direct model (4.2) that includes an additive noise, the proposed method is intrinsically denoising the signal (e.g., the noise inside the carotid is reduced) through the inversion process (see

Table 4.4). The denoising effect obtained by our BF approach does not suffer from any spatial resolution loss, as it could be the case if the raw channel data or the beamformed images were low-pass filtered.

Regarding the computational time, note that it is highly dependent on the length of the acquired raw channel data. For this case, the number of ranges was around $N = 2500$, and the proposed approaches were applied without a previous decimation of the raw channel data. Of course, the standard parallel computing methods could additionally improve the computational complexity, since the BF process is done for each lateral scanline. All the discussed methods were implemented with Matlab R2013b, on an Intel i7 2600 CPU working at 3.40GHz. Note that even so, LS BF is approaching the time capabilities of DAS, being just twice slower than DAS. Moreover, BP is also faster than MV. Thus, by using the discussed techniques for improving the computational expense, makes the two proposed methods good candidates for real-time applications.

4.4.5 *In vivo* data: healthy thyroid

Fig. 4.11 presents the beamforming results of healthy thyroid data. The thyroid (echoic region) is situated between the trachea and the carotid artery (laterally, between -20 mm and 30 mm approximately). Fig. 4.11 (a) illustrates the result obtained with DAS BF. As expected, the contrast of the image is low and it is hard to distinguish the thyroid structure from the trachea, especially in the upper-left part of the thyroid. However, when BP (Fig. 4.11 (b)) and LS Fig. 4.11 (c) are used, the thyroid region is easy to be identified, and the contrast of the image is increased. The best resolution of the beamformed image while maintaining a relatively high level of SNR and CNR is obtained with EN BF, see Fig. 4.11(d).

The values of CNR, SNR, and RG are depicted in the Table 4.5. To compute CNR we considered region R_2 inside the thyroid (the black circle positioned at approximately -10 mm laterally), and the region R_1 inside trachea (the white circle positioned at approximately -40 mm laterally). The SNR for R_1 was computed. We can observe that the best values of the CNR and SNR are obtained when LS method was applied, the thyroid region being obvious to be discerned. The boundaries of the carotid artery are also well defined, Fig. 4.11 (c).

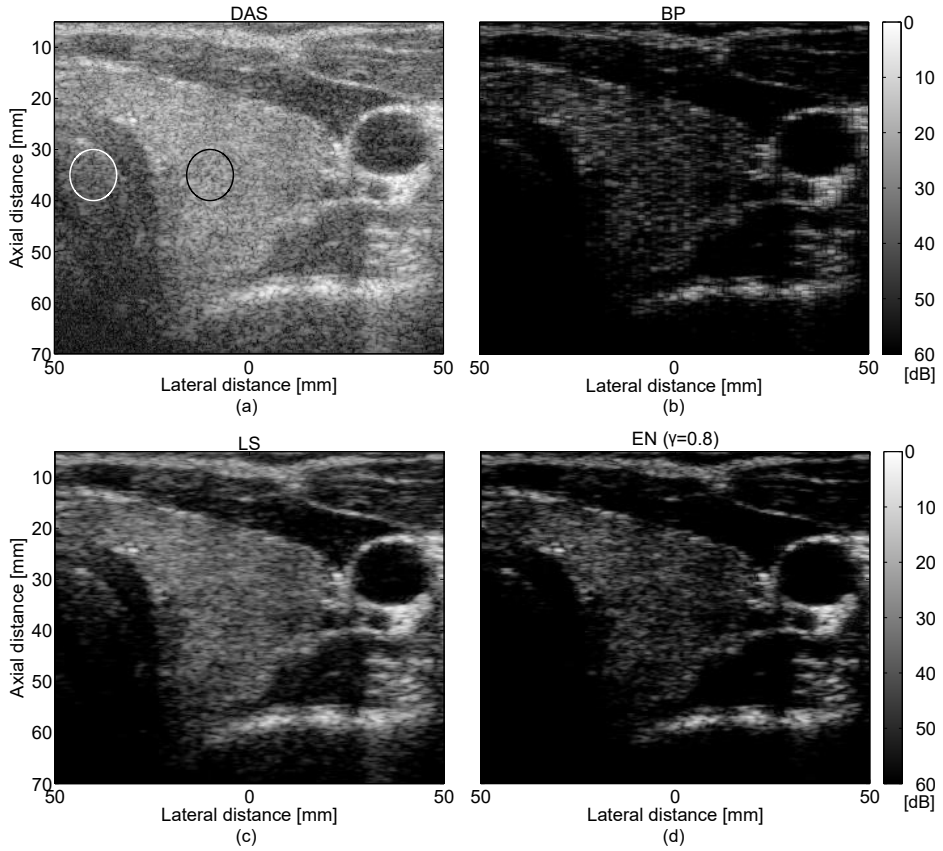

Figure 4.11: (a) DAS, (b) BP, (c) LS, and (d) EN ($\gamma = 0.8$) BF results of healthy thyroid *in vivo* data.

Table 4.5: CR, CNR, and SNR values for the *in vivo* healthy thyroid beamformed images in Fig. 4.11

BF Method	**CNR**	**SNR**	**RG**
DAS	0.55	0.22	1
BP	1.13	0.32	3
LS	**1.56**	**0.64**	2.5
EN ($\gamma = 0.8$)	1.48	0.46	**2.7**

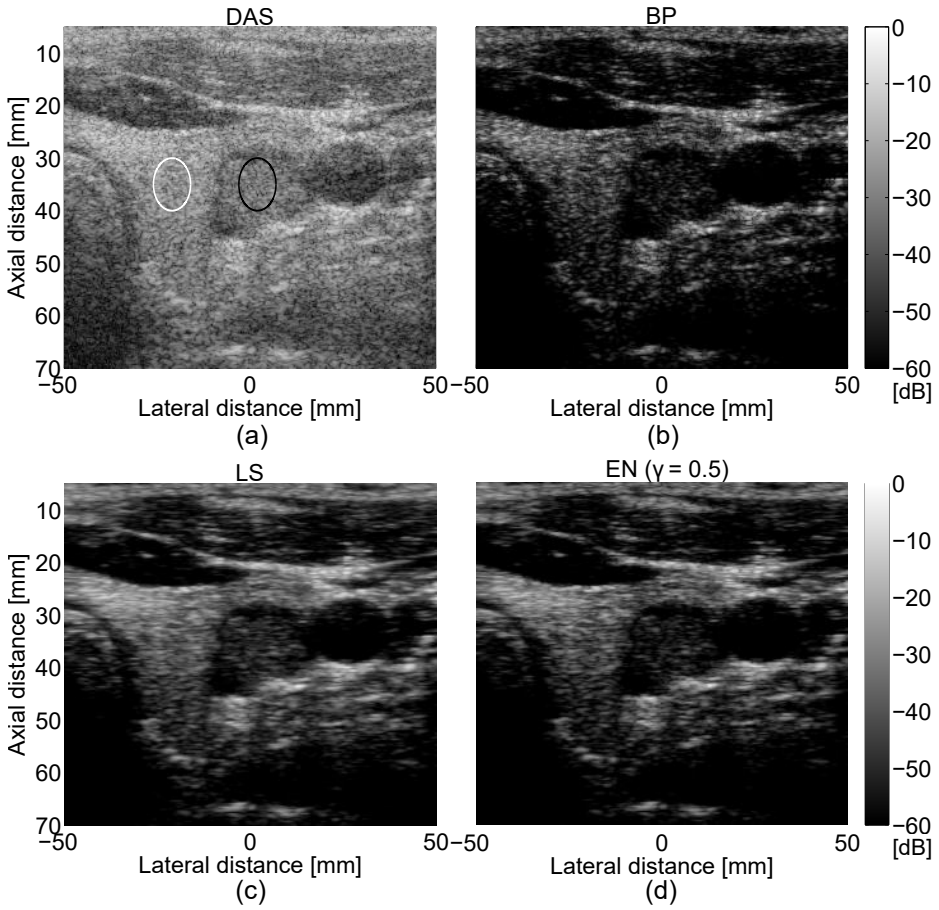

Figure 4.12: (a) DAS, (b) BP, (c) LS, and (d) EN ($\gamma = 0.8$) BF results of *in vivo* thyroid data with tumor.

Table 4.6: CNR, SNR, and RG values for the *in vivo* thyroidal beamformed images from Fig. 4.12

BF Method	CNR	SNR	RG
DAS	0.71	0.62	1
BP	1.16	0.79	2.9
LS	**1.32**	**0.86**	1.5
EN	1.2	0.76	**1.7**

4.4.6 *In vivo* data: thyroid with tumor

The beamformed results of the thyroid data with tumor are presented in the Fig. 4.12. The malignant tumor with an irregular structure can be seen between the left lobe of the thyroid (the hyper-echoic structure situated near the trachea) and the carotid artery (the hypo-echoic circular structure with the center at approximately 33 mm (axially) and 40 mm (laterally). We can observe that, contrarily to DAS beamformed image, where the tumor is hard to be distinguished (see Fig. 4.12 (a)), the proposed methods improve the visualization of the main structures, enhancing the edges of the tumor. The values of CNR, SNR, and RG are depicted in the Table 4.6, where a gain in resolution with a factor of almost 3 can be observed when using BP, compared with DAS, while with LS we obtain a higher improvement in contrast and SNR than with BP BF. CNR was computed by considering region R_2 inside the tumor (the black circle positioned at 0 mm laterally), and the region R_1 inside the left lobe of the thyroid (the white circle positioned at approximately -20 mm laterally). The SNR for R_1 was computed. The best value of RG is obtained by using RG BF (Fig. 4.12 (d)).

Note that the proposed framework was also tested on plane-wave imaging (see Section 1.1.5). The results and the details about the used datasets are presented in the Appendix A.

4.5 Conclusion

In this chapter, we have presented a new BF approach in US medical imaging, that solves a regularized inverse problem based on a linear model relating, for each depth, the US reflected data to the signal of interest. Contrarily to existing techniques that use adaptive or non-adaptive weights to average the raw channel data in order to form RF lines, we directly recover, for each depth, the desired signals using Laplacian, Gaussian, and elastic-net statistical assumptions. The proposed regularization-based BF allows us to take advantage of the beamspace processing that enables to highly reduce the number of US transmissions (by a factor of five in our examples), while improving the quality of the beamformed images compared to four existing beamformers. Multiple simulated and experimental examples were presented, that compare our approach with DAS, MV, multi-beam Capon, and IAA beamformers. We showed that our BF approaches, based on Laplacian and Gaussian prior information, although based on the same model, are

complementary in terms of result quality. Thus, Laplacian statistics are favoring sparse results while the Gaussian law is offering more regular and smooth images. Moreover, we showed that the elastic-net regularization takes advantages of both Laplacian and Gaussian distributions, resulting in the best RG factor of the beamformed images. We also proved through resolution gain, CNR and SNR image quality metrics, that we obtained an important gain in spatial resolution and/or in contrast, while maintaining a reasonable computational time compared to other existing techniques. In the next chapter, we will consider other statistical assumptions, such as the generalized Gaussian distribution, resulting in ℓ_p-norm minimization with the parameter p between 0 and 2. Following the choice of p, this should guarantee a better compromise between the gain in contrast and the improve of the spatial resolution (e.g., [Alessandrini et al., 2011], [Zhao et al., 2014], and [Chen et al., 2016a]).

In Chapter 5 we model beamforming by assuming the non-Gaussianity of the RF signals. Such formulations increase the robustness of the model proposed in this chapter, while increasing the contrast and the resolution of the resulting images compared with the existing BF methods in medical US imaging.

5

Beamforming of stable distributed ultrasound images

Part of this chapter was published in [Szasz et al., 2016a].

Contents

In this chapter we present a new beamforming method for ultrasound medical imaging based upon the statistical characterization of the ultrasound signals by α-stable distributions.

In the Chapter 4 we have reformulated BF in US imaging as a linear inverse problem, associating the raw channel data to the RF signals to be recovered. Numerical optimization routines have been employed to invert the resulting linear model based on standard regularization terms such as ℓ_1-norm, ℓ_2-norm, and elastic net. While US signal processing has widely relied for many years on the assumption of Gaussianity [Wagner et al., 1987], the authors in [Kutay et al., 2001] showed that RF echoes can be more accurately modelled by a power-law shot noise model. Later, this result has been confirmed by other research groups. For example, the statistical properties of the RF signals were related, based on the generalized central limit theorem, to α-stable distributions [Pereyra and Batatia, 2012].

The main contribution presented in this chapter is the use of non-Gaussianity properties of the RF signals in the beamforming process (e.g., [Pereyra and Batatia, 2012], [Alessandrini et al., 2011], and [Zhao et al., 2016b]). To the best of our knowledge, this is the first attempt of specifically considering an α-stable distribution while beamforming the received echoes in US imaging. Thus, the direct linear model presented in the Chapter 4 is herein inverted using a more general ℓ_p pseudo norm regularization, with p automatically related to the parameter α estimated from the data [Achim et al., 2015]. Contrarily to [Achim et al., 2015], the proposed direct model and the application (beamforming instead of compressive sampling) are different. Moreover, in this work p is automatically tuned for each depth, while it was fixed for the entire image in [Achim et al., 2015]. Given that p may take values smaller than 1, the resulting non-convex objective function was minimized by the half-quadratic optimization algorithm [Cetin and Karl, 2001] in this work.

The proposed method was evaluated on ultrasound simulated and *in vivo* thyroid data.

5.1 Acquisition setup

Fig. 5.1 presents the main elements used to derive the direct model on which is based the proposed beamforming method.

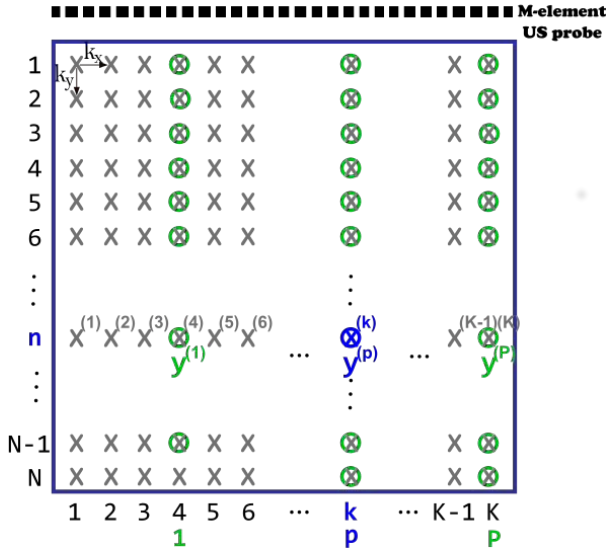

Figure 5.1: Main elements used to describe the proposed BF model.

We consider, without loss of generality, an M-element US probe that is sequentially transmitting P US beams. The beams can be focused, divergent, or plane waves [Tanter and Fink, 2014]. The reflected echoes are recorded with the same US probe and are time-delayed, so that time-of-flight differences are compensated. Depending on the exploration depth and on the sampling frequency, each recorded signal, after delay compensation (i.e., focalization), has N time samples. Henceforth, unless otherwise specified, all the developments are done for a given depth n (or sample n of the received signal, see Fig. 5.1), with $n = 1, \cdots, N$. For each emission $p = 1, \cdots, P$, we consider that M_p elements ($1 \leq M_p \leq M$) are receiving the echoes. Note that in the case when all elements of the US probe are active in reception, $M_1 = M_2 = \cdots = M_p = M$. Let us denote by $\boldsymbol{y}_p \in \mathbb{C}^{M_p \times 1}$ the raw channel data received by the M_p sensors, corresponding to depth n. In this situation, the classical DAS BF can be expressed as:

$$\boldsymbol{y}^{(p)} = \frac{\sum_{i=1}^{M_p} w_i y_p^{(i)}}{\sum_{i=1}^{M_p} w_i}, \tag{5.1}$$

where $y_p^{(i)}$ is the i^{th} element signal of $\boldsymbol{y}_p$, w_i are fixed BF weights (e.g., Hanning or Hamming windows) and $\boldsymbol{y}^{(p)}$ is the DAS BF signal of the p^{th} emission corresponding to the p^{th} element of vector, $\boldsymbol{y} \in \mathbb{C}^{P \times 1}$. Note that we consider in (5.1) the standard

case, where the horizontal (lateral) grid density of the DAS BF image corresponds to the number of US emissions. In other words, the data received for one emission serves at beamforming one position in the scanning grid. The positions to be beamformed with our method are highlighted by the symbol x and the positions corresponding to DAS beamforming are drawn by the symbol ◯ in Fig. 5.1. As we will explain in the next section, the proposed BF method will consider a further laterally refined scanning grid, as shown by the x symbols in Fig. 5.1.

5.2 Beamforming of US images modelled as stable random variables

5.2.1 Signal model

Let us denote by $\boldsymbol{x}$ the signal at depth n to be beamformed with the proposed method. We denote by K the size of this vector ($K \geq P$) as schematically highlighted in Fig. 5.1. Note that the total number of sensors M, the number of emissions P, and the number of lateral positions, K, on the scanned grid employed by the proposed method, are independent of each other. For a given depth n, similar with (4.2) (in Section 4.2) the model relating the received signal (raw channel data) $\boldsymbol{y}_p \in \mathbb{C}^{M_p \times 1}$ to the desired signal $\boldsymbol{x}$ can be written as follows:

$$\boldsymbol{y}_p = (\boldsymbol{A}_p^H \boldsymbol{A}_T)\boldsymbol{x} + \boldsymbol{g}_p, \tag{5.2}$$

where $\boldsymbol{A}_p \in \mathbb{C}^{M \times M_p}$ and $\boldsymbol{A}_T \in \mathbb{C}^{M \times K}$ are standard steering matrices relating the US probe element positions to the lateral positions on the scanline. More precisely, the form of $\boldsymbol{A}_p$ is considering that the K reflectors to be beamformed are impinging on M_p elements through their reflected pulses, while $\boldsymbol{A}_T$ is relating the positions of the M elements to the K reflectors, under the assumption that the elements are impinging on the reflectors. We denoted by $\boldsymbol{g}_p$ the additive white Gaussian noise affecting the raw channel data and with $(\cdot)^H$ the conjugate transpose. In the following, without loss of generality, we will consider that all US probe elements are active in reception, i.e., $\boldsymbol{A}_1 = \boldsymbol{A}_2 = \cdots = \boldsymbol{A}_p = \boldsymbol{A}$.

To reduce the dimensionality of the raw channel data, we applied beamspace processing [Malioutov et al., 2005], a common tool in array processing. It has been shown that in addition to reducing computational complexity sensitivity, beamspace processing allows improving the signal-to-noise ratio (SNR) [Tanter and Fink, 2014]. In our

case, DAS BF played the role of beamspace projection. Thus, while DAS only beamforms one position on the scanline for each emission, $\boldsymbol{y}_p \in \mathbb{C}^{M_p \times 1}$ in (5.2) becomes a scalar after applying DAS BF. Moreover, by making analogy to synthetic focusing [Jensen et al., 2006], $\boldsymbol{y}$ can be seen as the low resolution signal obtained by DAS, while $\boldsymbol{x}$ is the high resolution signal of interest. Finally, arranging all these scalars in a vector denoted by $\boldsymbol{y} \in \mathbb{C}^{P \times 1}$, the system of equations in (5.2) becomes:

$$\boldsymbol{y} = (\boldsymbol{A}^H \boldsymbol{A}_T)\boldsymbol{x} + \boldsymbol{g}, \tag{5.3}$$

where $\boldsymbol{A}_T \in \mathbb{C}^{M \times K}$, $\boldsymbol{A} \in \mathbb{C}^{M \times P}$, $\boldsymbol{x} \in \mathbb{C}^{K \times 1}$, and $\boldsymbol{g} \in \mathbb{C}^{K \times 1}$ have the same definition as in (5.2).

In the following, let us denote $\boldsymbol{\Phi} = \boldsymbol{A}^H \boldsymbol{A}_T$, $\boldsymbol{\Phi} \in \mathbb{C}^{P \times K}$. Thus, the direct model considered by our BF process becomes:

$$\boldsymbol{y} = \boldsymbol{\Phi}\boldsymbol{x} + \boldsymbol{g}. \tag{5.4}$$

Note that the system to invert is underdetermined, and more generally the inverse problem to solve is ill-posed, thus requiring regularization in order to obtain a valid solution.

5.2.2 α-stable distributions model

As explained previously, our BF solution is based on the hypothesis of α-stable distributed US signals. We remind that the characteristic function of a symmetric α-stable ($S\alpha S$) distribution has the form:

$$E(\theta) = \exp\left(j\theta\delta - \gamma|\theta|^\alpha\right), \tag{5.5}$$

where $\alpha \in (0, 2]$ is the characteristic index, $\delta \in (-\infty, \infty)$ is the location parameter, and $\gamma \in \mathbb{R}^+$ is the spread of the distribution. We emphasize that the stable law is a generalization of the Gaussian distribution, thus for $\alpha = 2$ the stable distribution is reduced to the Gaussian distribution [Shao and Nikias, 1993].

Interestingly, due to the stability property of this distribution and to the linear model that relates $\boldsymbol{x}$ to $\boldsymbol{y}$ (5.4), we can conclude that if $\boldsymbol{x}$ is supposed to follow an $S\alpha S$, then $\boldsymbol{y}$ can also be modelled by an $S\alpha S$ with the same parameter α [Achim et al., 2015]. This observation has an important practical interest, allowing us to estimate the parameter α corresponding to $\boldsymbol{x}$ from the observed vector $\boldsymbol{y}$. In this work, we have used the method in [Zolotarev, 1957] to estimate the parameter α from the discrete measurements $\boldsymbol{y}$.

5.2.3 Model inversion via ℓ_p-norm regularization

We have recently shown, in a different application context (compressive sampling), that the ℓ_p-norm regularization is well adapted to reconstruct $S\alpha S$-distributed signals [Achim et al., 2015]. Moreover, it has been shown that the optimal choice for parameter p is smaller but as close as possible to α [Achim et al., 2015], typically $p = \alpha - 0.01$. Following, this result, we propose herein to solve the BF problem in (5.4) by solving the following minimization problem:

$$\hat{\boldsymbol{x}} = \underset{\boldsymbol{x}}{\operatorname{argmin}}(\|\boldsymbol{y} - \boldsymbol{\Phi}\boldsymbol{x}\|_2^2 + \lambda\|\boldsymbol{x}\|_p^p), \tag{5.6}$$

where λ is the regularization parameter balancing the trade-off between the fidelity to the data and the regularization term.

Depending on the sparsity degree of the scanned medium, the value of p, directly related to α estimated from $\boldsymbol{y}$ (i.e., $p = \alpha - 0.01$), can take values smaller than 1. In this case, the function (5.6) to be minimized becomes non-convex. Several solutions to solve such non-convex problems exist in the literature (e.g., [Gould and Toint, 2002, Nikolova et al., 2008, Nikolova et al., 2010]). In this work, we used the half-quadratic optimization algorithm proposed in [Cetin and Karl, 2001], where a non-quadratic optimization problem is viewed as multiple quadratic problems. The main steps of the proposed beamforming approach, for a particular depth n, are described in the pseudo-code below:

Input: Raw channel data, $\boldsymbol{y}_p \in \mathbb{C}^{M_p \times 1}$.
Output: α-stable beamformed data, $\boldsymbol{x} \in \mathbb{C}^{K \times 1}$.
1) Apply DAS BF to $\boldsymbol{y}_p$ using (5.1) $\Rightarrow \boldsymbol{y} \in \mathbb{C}^{P \times 1}$.
2) Estimate α from $\boldsymbol{y}$.
3) Calculate p as: $p = \alpha - 0.01$.
4) Solve (5.6) using half-quadratic optimization $\Rightarrow \hat{\boldsymbol{x}}$.

Algorithm 3: α-stable beamforming at depth n.

Because the objective function of l_p-norm for $p < 1$ is not convex, and may converge to local optima, some smooth local optimization techniques are required for solving it. As solution to (5.6), in [Cetin and Karl, 2001] is proposed the half-quadratic regularization method, where a non-quadratic optimization problem is view as multiple quadratic problems. The algorithm can be seen as a quasi-Newton's method and iterates the following expression:

$$\boldsymbol{H}(\hat{\boldsymbol{x}}^{(i)})\hat{\boldsymbol{x}}^{(i+1)} = 2\boldsymbol{\Phi}^H\hat{\boldsymbol{y}}, \tag{5.7}$$

where i is the iteration number, and:

$$\begin{aligned} \boldsymbol{H}(\hat{\boldsymbol{x}}) &\triangleq 2\boldsymbol{\Phi}^H\boldsymbol{\Phi} + \lambda\Lambda(\hat{\boldsymbol{x}}) \\ \Lambda(\hat{\boldsymbol{x}}) &\triangleq diag\{\frac{p}{(|\hat{x}_i|^2+\epsilon)^{1-\frac{p}{2}}}\}, \end{aligned} \tag{5.8}$$

where $diag\{\cdot\}$ is the diagonal matrix with diagonal elements defined in the brackets and ϵ is called the smoothing parameter and has an important impact in the final results of BF. The algorithm stops when the following criteria is reached:

$$\frac{\|\hat{\boldsymbol{x}}^{(i+1)} - \hat{\boldsymbol{x}}^{(i)}\|_2^2}{\|\hat{\boldsymbol{x}}^{(i)}\|_2^2} < \delta, \tag{5.9}$$

with $\delta > 0$ a very small constant.

5.3 Results and discussion

To evaluate the proposed BF method (denoted hereafter by α-stable BF), we used both simulated and *in vivo* data. The simulated data contains 3 point reflectors at 50 mm in depth and an anechoic cyst structure of 10 mm radius at 80 mm in depth, embedded in speckle noise typical for US images. The simulated US probe had 64 elements, with the pitch of 256 μm, the height of 5 mm, and the center frequency of 3 MHz. The emissions corresponded to 52 steered plane waves (for the proposed method) and 260 steered plane waves (for DAS/MV BF methods), for angles between -30and30. The raw channel data was obtained using the state-of-the art ultrasound simulator Field II [Jensen, 2004].

The *in vivo* data represents the thyroid gland from a subject with a malignant tumor. The acquisition was done with a clinical Sonoline Elegra ultrasound system modified for research purposes, equipped with a Siemens Medical Systems 7.5L40 P/N 5260281-L0850 linear array transducer, emitting series of focalized waves.

Two of the most commonly used image quality metrics were calculated: the CNR and CR [dB]. Their definition can be found in Section 1.2.3. Region R_1 corresponds to a region inside the anechoic cyst structure for simulated data and to a region inside the tumor for *in vivo* data. Region R_2 is inside the homogeneous surrounding speckle

Table 5.1: CR, CNR, and FWHM values for simulated data beamformed images in Fig. 5.2

BF Method	CR[dB]	CNR	FWHM [mm]
DAS	58.22	6.40	1.55
MV	66.90	5.98	0.92
LS	56.41	6.08	1.29
α-stable	**69.74**	**7.65**	**0.32**

for both types of data, at the same depth with the region R_1. The results of simulated data were compared with standard DAS and MV method in [Asl and Mahloojifar, 2009]. Moreover, we have also compared our results to those obtained with the same BF model as the one proposed herein, but using a standard Tikhonov regularization (i.e. p equal to 2 in (5.6)) [Madore and Meral, 2012]. This method has been named LS (least-squares) BF. Since the *in vivo* data was acquired with a clinical scanner, the raw channel data necessary to apply MV was not accessible. Thus the results on *in vivo* data were only compared with standard DAS and LS BF methods.

5.3.1 Simulated data with point reflectors and an anechoic cyst structure

Fig. 5.2 presents the BF results of the simulated data containing 3 point reflectors and an hypoechoic cyst. The green circle represents the true border of the cyst. We can observe that DAS BF (Fig. 5.2(a)) is not able to resolve the dimensionality of the circular cyst. The cyst appears narrower than its original dimension, due to the low resolution provided by DAS. MV (Fig. 5.2(b)) and LS BF (Fig. 5.2(c)) provide better resolved results, i.e. the dimension of the cyst is closer to its real dimension. However, when using α-stable BF (Fig. 5.2(d)) we obtain better result in terms of spatial resolution, contrast, and resolution of the dimensionality of the scanned structures, compared with DAS, MV, and LS. The gain in contrast can be observed in the Table 5.1, where α-stable BF provides an improvement of 11.52 dB compared with DAS and of 2.84 dB compared with MV. Note that DAS and MV used raw channel data resulting from 5 times more US emissions than our method (i.e. 260 plane waves), such as the density of the beamforming grid was the same for all beamformers. With this example we showed

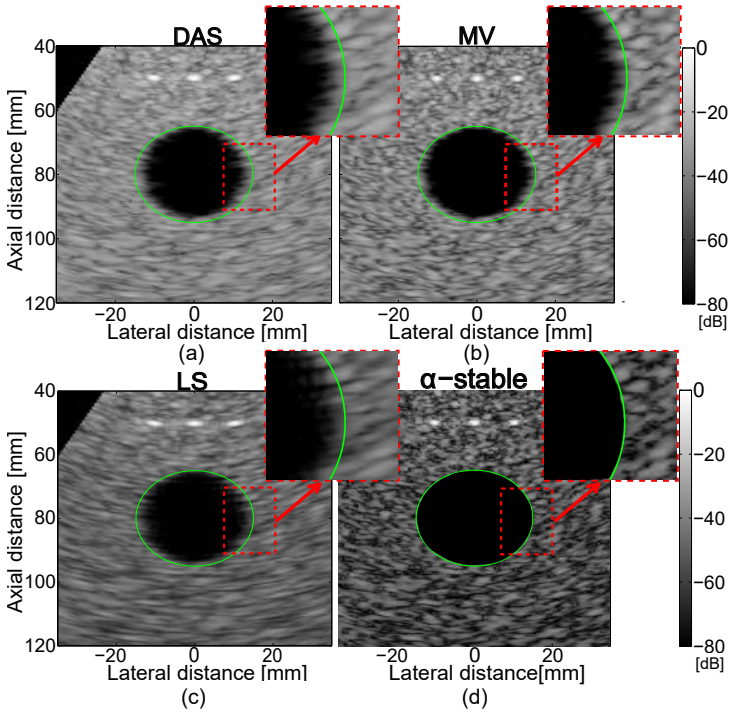

Figure 5.2: Results of (a) DAS, (b) MV, (c) LS (Tikhonov), and (d) $\alpha-$stable BF methods on simulated data with point reflectors and an anechoic cyst structure. The image quality metrics: CR, CNR, and FWHM are given in the Table 5.1.

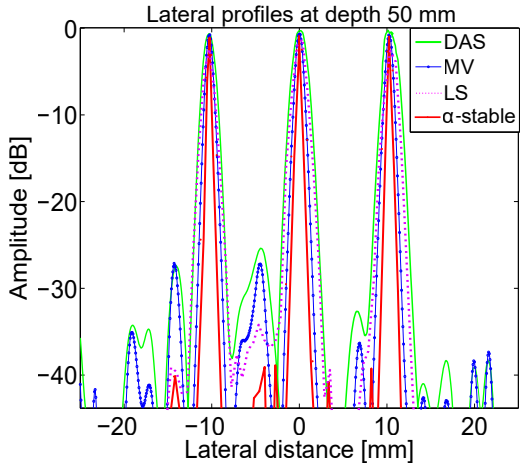

Figure 5.3: Lateral profiles at 50 mm of the DAS, MV, LS, and α-stable BF methods in Fig. 5.2.

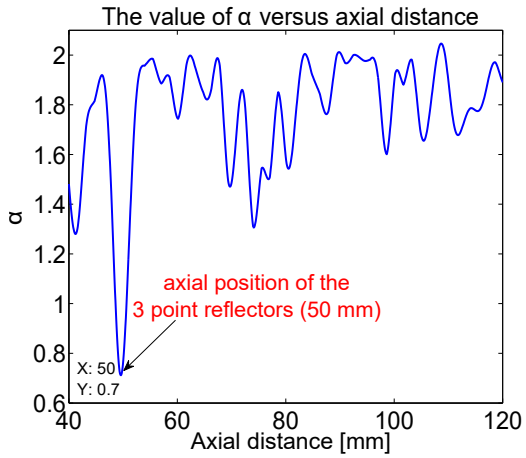

Figure 5.4: The value of α versus the axial distance in Fig. 5.2.

the ability of our method to work with reduced number of emissions. Of course, the result of our method with 260 emissions would be at least as good as the one using 5 times less emissions (52).

Fig. 5.3 depicts the lateral profiles at depth 50 mm (passing through the 3 point reflectors) obtained with the aforementioned BF methods. As expected, the 3 points reflectors are better resolved by α-stable beamformer, having narrower mainlobe and lower sidelobes compared with the other BF methods (we used FWHM - full width at half maximum, in Table 5.1, as quantitative indicator). Note that the FWHM is reduced at least 3 times using the proposed method compared with DAS, MV, and LS.

Fig. 5.4 illustrates the dependence of estimated parameter α on the structures at each depth of image in Fig. 5.2. We can observe that the minimum value of ($\alpha = 0.7$) is reached at depth 50 mm, where the 3 point reflectors are positioned, imposing sparse conditions to the scanned medium. Moreover, a value of $\alpha \approx 2$ is reached at the depths containing only homogeneous speckle structures, thus following a Gaussian distribution. The ability of α to adapt to the characteristics of the scanned medium is of high interest, as it allows p to automatically adapt to its best value in the optimization process.

5.3.2 *In vivo* data: thyroid with malignant tumor

The results of the BF of the thyroid data with a malignant tumor can be observed in the Fig. 5.5. The tumor (highlighted by the black arrow in Fig. 5.5(a)) is located

Table 5.2: CR and CNR values for the *in vivo* thyroid beamformed images in Fig. 5.5

BF Method	CR[dB]	CNR
DAS	2.98	0.16
LS	2.72	0.22
α-stable	**4.26**	**0.24**

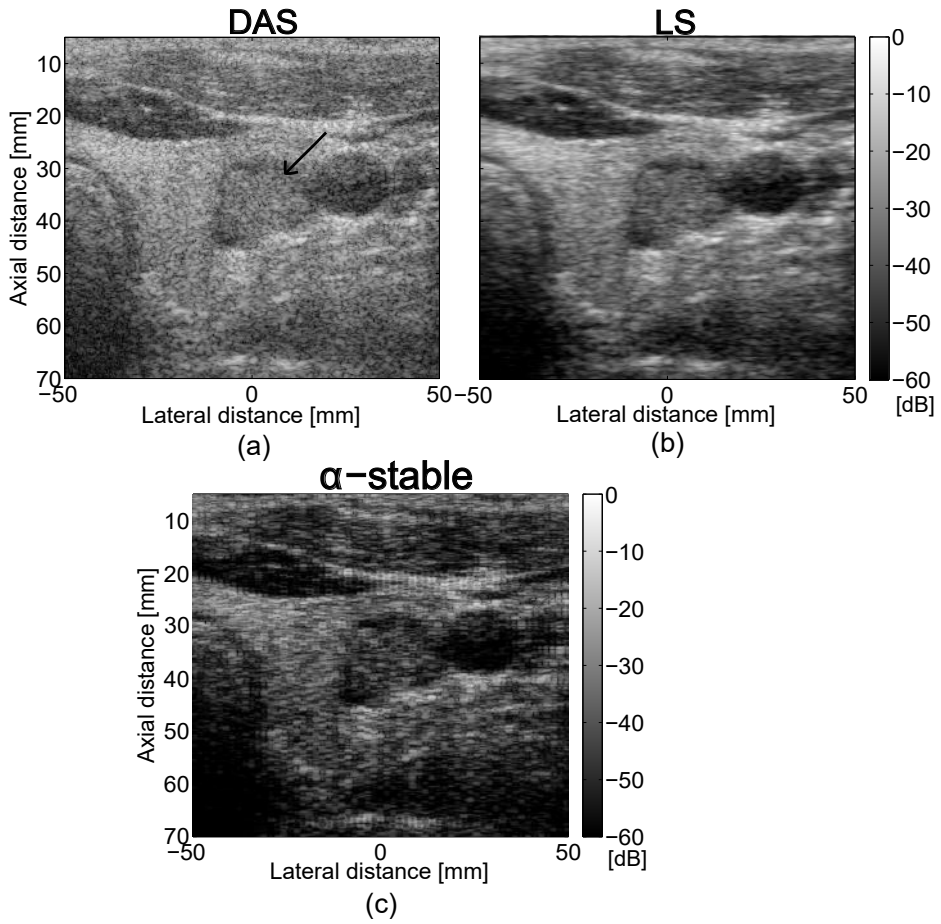

Figure 5.5: Results of (a) DAS, (b) LS, and (c) $\alpha-$stable BF methods on *in vivo* data of thyroid with malignant tumor (highlighted by the black arrow). The image quality metrics: CR and CNR are given in the Table 5.2.

in the left lobe of the thyroid, in the proximity of the carotid artery (the hypoechoic (dark) circular structure). The values of CR and CNR metrics are presented in the Table 5.2. Regarding the detection of the tumor, we can observe that by using DAS BF (Fig. 5.5(a)) it is difficult to delimit the region of the tumor because of the poor contrast and resolution of the image. The visual detection is improved when using LS BF (Fig. 5.5(b)). Furthermore, due to the increase in contrast, the edges of the tumor can be better visualized when using α-stable BF (Fig. 5.5(c)), compared with DAS and LS BF. Note that the raw channel *in vivo* data was not accessible (only DAS RF beamformed image was available), which may explain some banding artifacts visible on the α-stable final image (Fig. 5.5(c)).

5.4 Conclusion

In this chapter, we proposed a new beamforming method, by generalizing the previously proposed beamforming model (presented in the Chapter 4) in ultrasound imaging. Our method uses an ℓ_p-norm regularization to solve the inverse problem on which our model is based. Moreover, p is automatically calculated by relating it to the α-stable statistics of US images. Thus, our method, in contrast to minimum variance approaches, does not require any hyperparameter tunning and could also be of interest in other application domains such as direction of arrival estimation. Future work will include the evaluation of other acquisition strategies (e.g., ultrasound emissions in random directions) or the consideration of joint regularization terms for the joint reconstruction of several scanlines.

6

General conclusions and further research

6.1 Brief summary of the contributions of this work

The goal of this thesis was to model beamforming in ultrasound imaging as an inverse problem, relating the raw channel data to the signals to be recovered. This formulation was inspired from the source localization techniques that were very exploited in the last decades due to their different application areas. These techniques were developed to be robust to limited data, noise and the correlation of the sources.

We firstly investigated the used of sparse priors in medical ultrasound, by creating two-dimensional beamforming methods. With the proposed approaches, we were able to detect the position and the amplitude of the strong reflectors from the scanned medium by using the well-known Bayesian Information Criteria used in statistical modeling. Moreover, the proposed methods allow a parametric selection of the level of speckle in the final beamformed images. We showed, through simulated and recorded experimental data, the ability of the proposed methods to precisely detect the number and the spatial position of the strong reflectors in a sparse medium and to accurately reduce the speckle and highly enhance the contrast in a medium with speckle. In all experiments, the proposed approaches tend to preserve the speckle, which can be of major interest in clinical examinations, where it can contain useful information. However, when dealing with highly non-sparse scanning medium, we saw that our methods, since it examines each potential strong reflector, require high computational cost.

Secondly, we proposed a new framework for beamforming in medical ultrasound, by formulating beamforming as a linear inverse problem relating the reflected echoes to the signal to be recovered. This formalism allows us to invert the problem by imposing standard regularization such as ℓ_1, ℓ_2-norms, or elastic-net. The stated inverse problem is applied in lateral direction, contrarily with the most common beamforming methods in medical ultrasound that apply beamforming in axial direction. Our approach presents three major advantages: i) its flexibility in the choice of statistical assumptions on the signal to be beamformed, ii) its robustness to a reduced number of pulse emissions and iii) its robustness to correlation of the sources. Thus, the proposed framework allows for choosing the right trade-off between noise suppression and sharpness of the resulted image. We showed that the proposed beamforming approached, although based on the same model, are complementary. Concretely, the method based on Laplacian statistics enforces sparsity in the resulting ultrasound image, while the method based on Gaussian law results in more smooth and regular ultrasound images. A compromise between the two assumptions (Laplacian and Gaussian) can be obtained by using elastic-net regularization. The proposed framework taking into account the aforementioned statistic distributions was evaluated on both simulated and *in vivo* datasets and we showed an increase in contrast and the spatial resolution of the resulted images compared with four of the most efficient existing beamforming methods in medical ultrasound.

Finally, the third contribution was to model ultrasound medical imaging based on the statistical characterization of the ultrasound signals by α-stable distributions. While with the second contribution we took into account the Gaussianity assumption of the ultrasound signals, recently, was shown that the ultrasound signals can be more accurately modelled by a power-law shot noise model. In this work, we related the RF signals to the α-stable distributions. To the best of our knowledge, this is the first attempt to specifically consider an α-stable distribution while beamforming the received echoes in US imaging. Thus, the direct model presented with the second contribution was inverted using a more general ℓ_p pseudo norm regularization, with p automatically related to the parameter α estimated from the raw channel data. The main advantage of this contribution is the fact that it does not require any hyperparameter tunning. Moreover it could also be evaluated for other applications that solve source localization problem.

6.2 Suggestions for further research

6.2.1 Dictionary learning for sparse representation

Dictionary learning was already applied to 3D ultrasound imaging to reduce the volume of the data and speed up the acquisitions [Lorintiu et al., 2015]. Such dictionaries will result in even sparser representations of the signals, being optimized for a family of signals such as US images. In their work, they used K-SVD method to train the dictionaries for US signals. The model proposed in Chapter 4 could also use dictionary learning to learn about the characteristics of the US signals on each range.

6.2.2 Automatic estimation of hyperparameter p using a Bayesian framework

In our work the estimation of the regularization parameter p was done by relating p to the parameter α estimated from the RF signals which we characterized using α-stable distributions. Another method that is extensively used in image deconvolution, and can be of interest in beamforming of ultrasound images, is the Bayesian framework which could be used to estimate p in ℓ_p pseudo norm regularization problem. This framework is called Bayesian Blind Deconvolution (see, e.g., [Vega et al., 2014, Zhou et al., 2015, Zhao et al., 2016a]).

6.2.3 Joint time and space regularization

Our model presented in Chapter 4 and 5 is successively applied for each time sample (range). The main drawback of treating each range separately is the fact that we are not taking into account the correlation between the lateral scanlines. Thus, the results may suffer from sensitivity to SNR.

An interesting idea could be the combination of multiple scanlines by using joint regularization of several lateral scanlines [Chang et al., 2016]. Thus, multiple ranges could be used in synergy, unlike solving the inverse problem range by range. This technique was applied in source localization problem [Malioutov et al., 2005].

6.2.4 Combination with post-processing techniques

Our method is using raw channel data to model BF as an inverse problem. After applying BF, to the raw channel data, RF signals are formed. However, there exist

multiple techniques in ultrasound imaging that model RF lines as an inverse problem using regularization. These techniques are usually called post-processing techniques.

Being flexible, the proposed BF framework can be combined with the existing post-processing techniques, aiming to enhance the quality of the ultrasound images, such as deconvolution [Chen et al., 2016a] or super-resolution [Cox and Beard, 2015].

6.2.5 Evaluation of other acquisition strategies

The proposed framework can be evaluated for other acquisition strategies such as compressed acquisitions approaches used in compressive sampling [Liebgott et al., 2012]. Compressed acquisition mainly consists in randomly skipping the acquisition of several raw data channels. Thus, the amount of data needed is decreased and the acquisition is speed up. Integrating the compressed acquisition strategy with the framework proposed in Chapter 4, that also decreases the number of emissions, could result in even higher rates of acquisition. This could be of high interest in applications that require high acquisition rates (for e.g., cardiac imaging).

6.2.6 Evaluation of the proposed methods on other types of US data

Finally, it can be noticed that the validation of the proposed methods was performed on data containing healthy and pathological thyroid and healthy carotid. It is important to evaluate their performance on other types of *in vivo* data, such as cardiac data.

Appendix A

Results on plane-wave imaging

As stated in Section 1.1.5, there exist two common imaging modalities in medical US imaging. Until this point, all the results were shown by using the standard US imaging (Fig. 1.6(a)). Here, we test the proposed framework on plane-wave imaging (Fig. 1.6(b)).

In this section we used the datasets available during the PICMUS beamforming challenge [IUS, 2016]. The datasets were designed to evaluate two image quality metrics: resolution and contrast. Moreover, they were designed to ensure that there is no geometric distortion and that the speckle is preserved. Both simulated and experimental data were available. A Verasonics Vantage 256 platform was used to acquire data, with a linear L11-4v probe with the characteristics stated in Table A.1.

The results of applying DAS BF (described in Section 2.3) and the proposed BP BF (described in chapter 4) on the datasets proposed by the challenge for one plane-wave emission are illustrated in the Fig. A.1 and Table A.2. DAS BF method proposed by the challenge was used.

Table A.1: The characteristics of the L11-4v probe and of the transmit pulse

Pitch [mm]	0.3	Transmit frequency [MHz]	5.208
Element width [mm]	0.27	Sampling frequency [MHz]	20.832 MHz
Element height [mm]	5	Pulse bandwidth	67 %
Elevation focus [mm]	20	Transmit voltage	30 V
Number of elements [mm]	128	Excitation	2.5 cycles
Aperture [mm]	38.4		

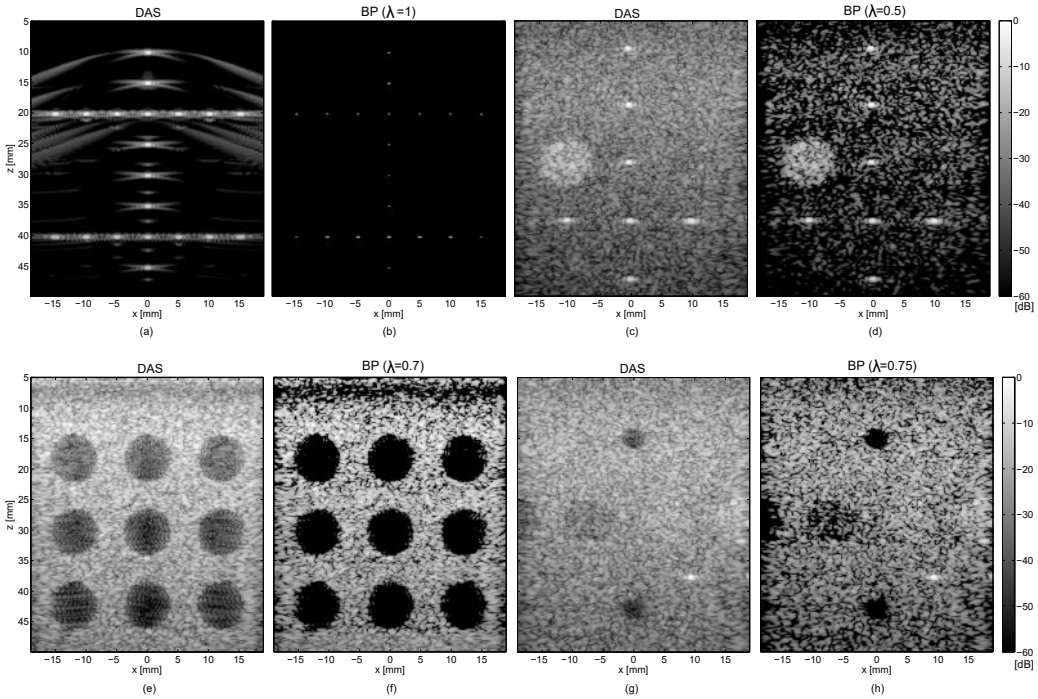

Figure A.1: (a) DAS - simulation (resolution), (b) BP - simulation (resolution), (c) DAS - experimental (resolution), (d) BP - experimental (resolution), (e) DAS - simulation (contrast), (f) BP - simulation (contrast), (g) DAS - experimental (contrast), (h) BP - experimental (contrast).

Table A.2: Mean resolution scores (axial & lateral) and contrast scores (dB) in Fig. A.1

BF Method and type	**Mean resolution (axial & lateral)**	**Mean contrast (dB)**
DAS - simulation	Fig. A.1(a): 0.40 0.82	Fig. A.1(e): 9.72
BP - simulation	Fig. A.1(b): **0.13 0.31**	Fig. A.1(f): **12.73**
DAS - experimental	Fig. A.1(c): 0.57 0.89	Fig. A.1(g): 7.90
BP - experimental	Fig. A.1(d): **0.35 0.57**	Fig. A.1(h): **10.10**

For this example, we observed that BP BF results in improved resolution and contrast than LS BF. Thus, Fig. A.1 presents the comparison between DAS and BP beamformers. For simulated point reflectors, we can observe that in the case of plane-wave imaging, DAS BF results in low resolution. It is hard to distinguish between the point reflectors present in the scanned medium (Fig. A.1(a)) and it is hard to predict their number. However, when using the proposed BP BF method (Fig. A.1(b)), the scatterers are very well resolved, at the correct positions. Table A.2 reinforces this observation, where we can observe that both axial and lateral resolutions are ≈ 3 times higher when using BP compared with DAS. In the case of experimental data we can also observe an improvement in the spatial resolution when using BP (Fig. A.1(d)) compared with DAS (Fig. A.1(c)). Note that an increase in spatial resolution can be obtained if the value of λ is increased, but at the cost of the degradation of the speckle's characteristics. Regarding the improvement of the contrast, we can observe that for both simulation (Fig. A.1(e) and Fig. A.1(f)) and experimental datasets (Fig. A.1(g) and Fig. A.1(h)), an improvement of ≈ 3 dB can be obtained by using BP compared with DAS (see Table A.2).

List of publications

ARTICLES DE REVUES INTERNATIONALES

2016 Strong reflector-based beamforming in ultrasound medical imaging (Teodora Szasz, Adrian Basarab, Denis Kouamé), *In Ultrasonics*, Elsevier, volume 66, pp. 111-124, 2016.

2016 Beamforming through regularized inverse problems in ultrasound medical imaging (Teodora Szasz, Adrian Basarab, Denis Kouamé), *In IEEE Transactions on Ultrasonics, Ferroelectrics and Frequency Control*, 2016 (to appear).

CONFERENCES

2016 Beamforming of ultrasound images modelled as stable random variables (to appear) (Teodora Szasz, Adrian Basarab, Denis Kouamé), *In 2016 IEEE International Ultrasonics Symposium*, pp. , 2016.

2016 Elastic-Net Based Beamforming in Medical Ultrasound Imaging (Teodora Szasz, Adrian Basarab, Mircea-Florin Vaida, Denis Kouamé), *In 2016 IEEE International Symposium on Biomedical Imaging*, pp. 477-480, 2016.

2015 Formation de voies avec renforcement des échos forts en imagerie ultrasonore (regular paper) (Teodora Szasz, Adrian Basarab, Denis Kouamé), *In Groupe de Recherche et d'Etudes du Traitement du Signal et des Images (GRETSI), Lyon, 08/09/2015-11/09/2015*, GRETSI CNRS, pp. (support électronique), 2015.

2014 Beamforming with sparse prior in ultrasound medical imaging (Teodora Szasz, Adrian Basarab, Mircea-Florin Vaida, Denis Kouamé), *In Ultrasonics Symposium (IUS), 2014 IEEE International*, pp. 1077-1080, 2014.

References

[Achim et al., 2015] Achim, A., Basarab, A., Tzagkarakis, G., Tsakalides, P., and Kouamé, D. (2015). Reconstruction of Ultrasound RF Echoes Modeled as Stable Random Variables. *IEEE Transactions on Computational Imaging*, 1(2):86–95. xxxii, 100, 103, 104

[Alessandrini et al., 2012] Alessandrini, M., Liebgott, H., Friboulet, D., and Bernard, O. (2012). Simulation of realistic echocardiographic sequences for ground-truth validation of motion estimation. In *Image Processing (ICIP), 2012 19th IEEE International Conference on*, pages 2329–2332. IEEE. xxviii, 49, 52, 79, 81

[Alessandrini et al., 2011] Alessandrini, M., Maggio, S., Poree, J., De Marchi, L., Speciale, N., Franceschini, E., Bernard, O., and Basset, O. (2011). A restoration framework for ultrasonic tissue characterization. *IEEE Transactions on Ultrasonics, Ferroelectrics, and Frequency Control*, 58(11):2344–2360. xxxii, 98, 100

[Angelsen, 2000a] Angelsen, B. (2000a). *Ultrasound imaging : Waves, Signals, and Signal Processing (vol 2)*. Ultrasound Imaging: Waves, Signals, and Signal Processing. Emantec. 5

[Angelsen, 2000b] Angelsen, B. (2000b). *Ultrasound Imaging: Waves, Signals, and Signal Processing (vol1)*. Ultrasound Imaging: Waves, Signals, and Signal Processing. Emantec. 5, 8

[Asl and Mahloojifar, 2009] Asl, B. M. and Mahloojifar, A. (2009). Minimum variance beamforming combined with adaptive coherence weighting applied to medical ultrasound imaging. *Ultrasonics, Ferroelectrics and Frequency Control, IEEE Transactions on*, 56(9):1923–1931. 28, 49, 80, 106

[Asl and Mahloojifar, 2012] Asl, B. M. and Mahloojifar, A. (2012). A low-complexity adaptive beamformer for ultrasound imaging using structured covariance matrix. *Ultrasonics, Ferroelectrics and Frequency Control, IEEE Transactions on*, 59(4):660–667. 28

[Candes et al., 2008] Candes, E. J., Wakin, M. B., and Boyd, S. P. (2008). Enhancing sparsity by reweighted l1 minimization. *Journal of Fourier analysis and applications*, 14(5-6):877–905. 47

[Capon, 1969] Capon, J. (1969). High-resolution frequency-wavenumber spectrum analysis. *Proceedings of the IEEE*, 57(8):1408–1418. xxiv, 25

[Cetin and Karl, 2001] Cetin, M. and Karl, W. (2001). Feature-enhanced synthetic aperture radar image formation based on nonquadratic regularization. *IEEE Transactions on Image Processing*, 10(4):623–631. xxxii, 100, 104

[Chang et al., 2016] Chang, K., Ding, P. L. K., and Li, B. (2016). Compressive Sensing Reconstruction of Correlated Images Using Joint Regularization. *IEEE Signal Processing Letters*, 23(4):449–453. 113

[Chen et al., 2002] Chen, J. C., Yao, K., and Hudson, R. E. (2002). Source localization and beamforming. *IEEE Signal Processing Magazine*, 19(2):30–39. 31

[Chen et al., 1998] Chen, S. S., Donoho, D. L., and Saunders, M. A. (1998). Atomic Decomposition by Basis Pursuit. *SIAM Journal on Scientific Computing*, 20(1):33–61. xxix, 75

[Chen et al., 2015] Chen, Z., Basarab, A., and Kouamé, D. (2015). A simulation study on the choice of regularization parameter in ℓ_2-norm ultrasound image restoration. In *2015 37th Annual International Conference of the IEEE Engineering in Medicine and Biology Society (EMBC)*, pages 6346–6349. 79

[Chen et al., 2016a] Chen, Z., Basarab, A., and Kouamé, D. (2016a). Compressive Deconvolution in Medical Ultrasound Imaging. *IEEE Transactions on Medical Imaging*, 35(3):728–737. xxix, 70, 98, 114

[Chen et al., 2016b] Chen, Z., Basarab, A., and Kouamé, D. (2016b). Compressive deconvolution in medical ultrasound imaging. *IEEE Transactions on Medical Imaging*, 35(3):728–737. 41

[Chernyakova and Eldar, 2014] Chernyakova, T. and Eldar, Y. C. (2014). Fourier-domain beamforming: the path to compressed ultrasound imaging. *IEEE Transactions on Ultrasonics, Ferroelectrics, and Frequency Control*, 61(8):1252–1267. 39

[Cox and Beard, 2015] Cox, B. and Beard, P. (2015). Imaging techniques: Super-resolution ultrasound. *Nature*, 527(7579):451–452. 114

[David et al., 2015a] David, G., Robert, J.-l., Zhang, B., and Laine, A. F. (2015a). Time domain compressive beam forming of ultrasound signals. *The Journal of the Acoustical Society of America*, 137(5):2773–2784. 39

[David et al., 2015b] David, G., Robert, J.-l., Zhang, B., and Laine, A. F. (2015b). Time domain compressive beamforming: Application to in-vivo echocardiography. In *Ultrasonics Symposium (IUS), 2015 IEEE International*, pages 1–4. IEEE. 39

[Diamantis et al., 2014] Diamantis, K., Holfort-Voxen, I. K., Greenaway, A. H., Anderson, T., Jensen, J. A., and Sboros, V. (2014). A comparison between temporal and subband minimum variance adaptive beamforming. In *SPIE Medical Imaging*, pages 90400L–90400L. International Society for Optics and Photonics. 30

[Dobigeon et al., 2012] Dobigeon, N., Basarab, A., Kouamé, D., and Tourneret, J.-Y. (2012). Regularized bayesian compressed sensing in ultrasound imaging. In *Signal Processing Conference (EUSIPCO), 2012 Proceedings of the 20th European*, pages 2600–2604. IEEE. 47

[Du et al., 2008] Du, L., Yardibi, T., Li, J., and Stoica, P. (2008). Review of user parameter-free robust adaptive beamforming algorithms. In *2008 42nd Asilomar Conference on Signals, Systems and Computers*, pages 363–367. 72, 75

[Dwight E. Gray, 1957] Dwight E. Gray (1957). *American Institute of Physics Handbook*. 10

[Ellis et al., 2010] Ellis, M. A., Viola, F., and Walker, W. F. (2010). Super-Resolution Image Reconstruction Using Diffuse Source Models. *Ultrasound in Medicine & Biology*, 36(6):967–977. 41

[Engl et al., 1996] Engl, H. W., Hanke, M., and Neubauer, A. (1996). *Regularization of Inverse Problems*. Springer Science & Business Media. 40

[Ensminger and Bond, 2011] Ensminger, D. and Bond, L. J. (2011). *Ultrasonics: Fundamentals, Technologies, and Applications, Third Edition*. CRC Press. 9

[Foster et al., 2000] Foster, F. S., Pavlin, C. J., Harasiewicz, K. A., Christopher, D. A., and Turnbull, D. H. (2000). Advances in ultrasound biomicroscopy. *Ultrasound in Medicine & Biology*, 26(1):1–27. 16

[Fuchs, 1996] Fuchs, J. (1996). Linear programming in spectral estimation. Application to array processing. In *, 1996 IEEE International Conference on Acoustics, Speech, and Signal Processing, 1996. ICASSP-96. Conference Proceedings*, volume 6, pages 3161–3164 vol. 6. xxix, 72, 73

[Galatsanos and Katsaggelos, 1992] Galatsanos, N. P. and Katsaggelos, A. K. (1992). Methods for choosing the regularization parameter and estimating the noise variance in image restoration and their relation. *Image Processing, IEEE Transactions on*, 1(3):322–336. 47, 68, 79

[Gould and Toint, 2002] Gould, N. I. M. and Toint, P. L. (2002). Numerical Methods for Large-Scale Non-Convex Quadratic Programming. In *Trends in Industrial and Applied Mathematics*, number 72 in Applied Optimization, pages 149–179. Springer US. DOI: 10.1007/978-1-4613-0263-6_8. 104

[Gudmundson et al., 2011] Gudmundson, E., Jakobsson, A., Jensen, J. A., and Stoica, P. (2011). Blood velocity estimation using ultrasound and spectral iterative adaptive approaches. *Signal Processing*, 91(5):1275–1283. 35

[Holfort et al., 2009] Holfort, I. K., Gran, F., and Jensen, J. A. (2009). Broadband minimum variance beamforming for ultrasound imaging. *Ultrasonics, Ferroelectrics and Frequency Control, IEEE Transactions on*, 56(2):314–325. 30

[Huang et al., 2010] Huang, J., Berger, C., Zhou, S., and Huang, J. (2010). Comparison of basis pursuit algorithms for sparse channel estimation in underwater acoustic OFDM. In *OCEANS 2010 IEEE - Sydney*, pages 1–6. 76

[(IAEA), 2014] (IAEA), I. A. E. A. (2014). Diagnostic Radiology Physics. xvii, 2, 4, 6

[IUS, 2016] IUS, I. (2016). PICMUS | Plane-wave Imaging Challenge in Medical UltraSound. 115

[Jensen and Austeng, 2012] Jensen, A. and Austeng, A. (2012). An approach to multibeam covariance matrices for adaptive beamforming in ultrasonography. *IEEE Transactions on Ultrasonics, Ferroelectrics, and Frequency Control*, 59(6):1139–1148. 33, 34, 80

[Jensen and Austeng, 2014] Jensen, A. and Austeng, A. (2014). The iterative adaptive approach in medical ultrasound imaging. *IEEE Transactions on Ultrasonics, Ferroelectrics, and Frequency Control*, 61(10):1688–1697. xxiv, 17, 35, 36, 80, 82

[Jensen, 2004] Jensen, J. (2004). Simulation of advanced ultrasound systems using Field II. In *IEEE International Symposium on Biomedical Imaging: Nano to Macro, 2004*, pages 636–639 Vol. 1. 79, 105

[Jensen and Svendsen, 1992] Jensen, J. and Svendsen, N. (1992). Calculation of pressure fields from arbitrarily shaped, apodized, and excited ultrasound transducers. *IEEE Transactions on Ultrasonics, Ferroelectrics, and Frequency Control*, 39(2):262–267. 29, 49, 79

[Jensen, 1992] Jensen, J. A. (1992). Deconvolution of ultrasound images. *Ultrasonic Imaging*, 14(1):1–15. 41

[Jensen, 1999] Jensen, J. A. (1999). Linear description of ultrasound imaging systems. 20

[Jensen, 2007] Jensen, J. A. (2007). Medical ultrasound imaging. *Progress in Biophysics and Molecular Biology*, 93(1-3):153–165. 16

[Jensen et al., 2006] Jensen, J. A., Nikolov, S. I., Gammelmark, K. L., and Pedersen, M. H. (2006). Synthetic aperture ultrasound imaging. *Ultrasonics*, 44, Supplement:e5–e15. 103

[Jirik and Taxt, 2008] Jirik, R. and Taxt, T. (2008). Two-dimensional blind Bayesian deconvolution of medical ultrasound images. *IEEE Transactions on Ultrasonics, Ferroelectrics, and Frequency Control*, 55(10):2140–2153. 70

[Kautz and Zoltowski, 1996] Kautz, G. and Zoltowski, M. (1996). Beamspace DOA estimation featuring multirate eigenvector processing. *IEEE Transactions on Signal Processing*, 44(7):1765–1778. 34

[Konishi and Kitagawa, 2008] Konishi, S. and Kitagawa, G. (2008). *Information criteria and statistical modeling*. Springer Science & Business Media. xxviii, 44, 47

[Krim and Viberg, 1996] Krim, H. and Viberg, M. (1996). Two decades of array signal processing research: the parametric approach. *IEEE Signal Processing Magazine*, 13(4):67–94. xxiv, 31

[Kutay et al., 2001] Kutay, M. A., Petropulu, A. P., and Piccoli, C. W. (2001). On modeling biomedical ultrasound RF echoes using a power-law shot-noise model. *IEEE Transactions on Ultrasonics, Ferroelectrics, and Frequency Control*, 48(4):953–968. 100

[Kuttruff, 1991] Kuttruff, H. (1991). Generation and Detection of Sound with Frequencies Above 1 GHz (Hypersound). In *Ultrasonics*, pages 187–205. Springer Netherlands. DOI: 10.1007/978-94-011-3846-8_7. xxiii, 4

[Lavarello et al., 2006] Lavarello, R., Kamalabadi, F., and O'Brien, W. D. (2006). A regularized inverse approach to ultrasonic pulse-echo imaging. *IEEE Transactions on Medical Imaging*, 25(6):712–722. 41

[Li and Stoica, 2006] Li, J. and Stoica, P. (2006). *Robust adaptive beamforming*. Wiley Online Library. 25

[Li et al., 2003] Li, J., Stoica, P., and Wang, Z. (2003). On robust Capon beamforming and diagonal loading. *IEEE Transactions on Signal Processing*, 51(7):1702–1715. 28

[Li and Li, 2003] Li, P.-C. and Li, M.-L. (2003). Adaptive imaging using the generalized coherence factor. *IEEE Transactions on Ultrasonics, Ferroelectrics, and Frequency Control*, 50(2):128–141. 28

[Liebgott et al., 2012] Liebgott, H., Basarab, A., Kouamé, D., Bernard, O., and Friboulet, D. (2012). Compressive sensing in medical ultrasound. In *2012 IEEE International Ultrasonics Symposium*, pages 1–6. 114

[Lingvall, 2004] Lingvall, F. (2004). A method of improving overall resolution in ultrasonic array imaging using spatio-temporal deconvolution. *Ultrasonics*, 42(1-9):961–968. 41

[Lingvall and Olofsson, 2007] Lingvall, F. and Olofsson, T. (2007). On Time-Domain Model-Based Ultrasonic Array Imaging. *IEEE Transactions on Ultrasonics, Ferroelectrics, and Frequency Control*, 54(8):1623–1633. 41

[Lorenz et al., 2015] Lorenz, D. A., Pfetsch, M. E., and Tillmann, A. M. (2015). Solving Basis Pursuit: Heuristic Optimality Check and Solver Comparison. *ACM Transactions on Mathematical Software*, 41(2):1–29. 76

[Lorintiu et al., 2015] Lorintiu, O., Liebgott, H., Alessandrini, M., Bernard, O., and Friboulet, D. (2015). Compressed Sensing Reconstruction of 3d Ultrasound Data Using Dictionary Learning and Line-Wise Subsampling. *IEEE Transactions on Medical Imaging*, 34(12):2467–2477. 113

[Madore and Meral, 2012] Madore, B. and Meral, F. C. (2012). Reconstruction algorithm for improved ultrasound image quality. *IEEE Transactions on Ultrasonics, Ferroelectrics, and Frequency Control*, 59(2):217–230. 41, 106

[Malioutov et al., 2005] Malioutov, D., Çetin, M., and Willsky, A. S. (2005). A sparse signal reconstruction perspective for source localization with sensor arrays. *Signal Processing, IEEE Transactions on*, 53(8):3010–3022. 40, 72, 73, 102, 113

[Malioutov et al., 2002] Malioutov, D. M., Cetin, M., Iii, J. W. F., and Willsky, A. S. (2002). Superresolution Source Localization through Data-Adaptive Regularization. In *In Adaptive Sensor Array Processing Workshop*, pages 3–17. 40

[Malioutov et al., 2003] Malioutov, D. M., Cetin, M., and Willsky, A. S. (2003). Source localization by enforcing sparsity through a Laplacian prior: an SVD-based approach. In *2003 IEEE Workshop on Statistical Signal Processing*, pages 573–576. 40

[Mallart and Fink, 1994] Mallart, R. and Fink, M. (1994). Adaptive focusing in scattering media through sound-speed inhomogeneities: The van Cittert Zernike approach and focusing criterion. *The Journal of the Acoustical Society of America*, 96(6):3721–3732. 28

[Merton, 1997] Merton, D. A. (1997). Diagnostic Medical Ultrasound Technology A Brief Historical Review. *Journal of Diagnostic Medical Sonography*, 13(5 suppl):10S–23S. 16

[Michailovich and Rathi, 2015] Michailovich, O. and Rathi, Y. (2015). Adaptive learning of tissue reflectivity statistics and its application for blind deconvolution of medical ultrasound scans. In *2015 IEEE. International Ultrasonics Symposium. Taipei, Taiwan, October 21 24.* xxix, 70

[Michailovich and Tannenbaum, 2007] Michailovich, O. and Tannenbaum, A. (2007). Blind deconvolution of medical ultrasound images: a parametric inverse filtering approach. *IEEE transactions on image processing: a publication of the IEEE Signal Processing Society*, 16(12):3005–3019. 40, 41, 70, 75

[Michailovich and Tannenbaum, 2006] Michailovich, O. V. and Tannenbaum, A. (2006). Despeckling of medical ultrasound images. *IEEE Transactions on Ultrasonics, Ferroelectrics, and Frequency Control*, 53(1):64–78. 41

[Morin et al., 2013] Morin, R., Bidon, S., Basarab, A., and Kouamé, D. (2013). Semi-blind deconvolution for resolution enhancement in ultrasound imaging. In *2013 IEEE International Conference on Image Processing*, pages 1413–1417. 41

[Mosci and Rosasco, 2010] Mosci, S. and Rosasco, L. (2010). Solving Structured Sparsity Regularization with Proximal Methods. In *Machine Learning and Knowledge*

Discovery in Databases, number 6322, pages 418–433. Springer Berlin Heidelberg. DOI: 10.1007/978-3-642-15883-4_27. 77

[Nikolova et al., 2008] Nikolova, M., Ng, M., Zhang, S., and Ching, W. (2008). Efficient Reconstruction of Piecewise Constant Images Using Nonsmooth Nonconvex Minimization. *SIAM Journal on Imaging Sciences*, 1(1):2–25. 104

[Nikolova et al., 2010] Nikolova, M., Ng, M. K., and Tam, C. P. (2010). Fast Nonconvex Nonsmooth Minimization Methods for Image Restoration and Reconstruction. *IEEE Transactions on Image Processing*, 19(12):3073–3088. 104

[Nilsen and Hafizovic, 2009] Nilsen, C. and Hafizovic, I. (2009). Beamspace adaptive beamforming for ultrasound imaging. *IEEE Transactions on Ultrasonics, Ferroelectrics, and Frequency Control*, 56(10):2187–2197. 32, 33, 73

[Nilsen and Holm, 2010] Nilsen, C. I. C. and Holm, S. (2010). Wiener beamforming and the coherence factor in ultrasound imaging. *IEEE Transactions on Ultrasonics, Ferroelectrics, and Frequency Control*, 57(6):1329–1346. 29

[Pereyra and Batatia, 2012] Pereyra, M. and Batatia, H. (2012). Modeling ultrasound echoes in skin tissues using symmetric α-stable processes. *IEEE Transactions on Ultrasonics, Ferroelectrics, and Frequency Control*, 59(1):60–72. xxxii, 100

[Quinsac et al., 2010] Quinsac, C., Basarab, A., Girault, J., and Kouamé, D. (2010). Compressed sensing of ultrasound images: sampling of spatial and frequency domains. In *Signal Processing Systems (SIPS), 2010 IEEE Workshop on*, pages 231–236. IEEE. 39

[Ramani et al., 2012] Ramani, S., Liu, Z., Rosen, J., Nielsen, J., and Fessler, J. A. (2012). Regularization parameter selection for nonlinear iterative image restoration and mri reconstruction using gcv and sure-based methods. *Image Processing, IEEE Transactions on*, 21(8):3659–3672. 47, 68, 79

[Rindal et al., 2014] Rindal, O. M. H., Asen, J. P., Holm, S., and Austeng, A. (2014). Understanding contrast improvements from capon beamforming. In *Ultrasonics Symposium (IUS), 2014 IEEE International*, pages 1694–1697. IEEE. xxiv, 17, 30, 55, 60, 64, 84, 91

[Schmidt, 1981] Schmidt, R. (1981). *A Signal Subspace Approach to Multiple Emitter Location and Spectral Estimation*. Stanford University. xxiv, 31

[Shao and Nikias, 1993] Shao, M. and Nikias, C. L. (1993). Signal processing with fractional lower order moments: stable processes and their applications. *Proceedings of the IEEE*, 81(7):986–1010. xxxii, 103

[Stoica and Sharman, 1990] Stoica, P. and Sharman, K. C. (1990). Maximum likelihood methods for direction-of-arrival estimation. *IEEE Transactions on Acoustics, Speech, and Signal Processing*, 38(7):1132–1143. xxiv, 31

[Synnevag et al., 2007a] Synnevag, J.-F., Austeng, A., and Holm, S. (2007a). Adaptive beamforming applied to medical ultrasound imaging. *Ultrasonics, Ferroelectrics and Frequency Control, IEEE Transactions on*, 54(8):1606–1613. 26, 27, 28

[Synnevag et al., 2009] Synnevag, J.-F., Austeng, A., and Holm, S. (2009). Benefits of minimum-variance beamforming in medical ultrasound imaging. *Ultrasonics, Ferroelectrics and Frequency Control, IEEE Transactions on*, 56(9):1868–1879. 26

[Synnevag et al., 2007b] Synnevag, J.-F., Nilsen, C.-I., and Holm, S. (2007b). P2b-13 speckle statistics in adaptive beamforming. In *Ultrasonics Symposium, 2007. IEEE*, pages 1545–1548. IEEE. 26

[Szasz et al., 2015] Szasz, T., Basarab, A., and Kouamé, D. (2015). Formation de voies avec renforcement des échos forts en imagerie ultrasonore (regular paper). In *Groupe de Recherche et d'Etudes du Traitement du Signal et des Images (GRETSI), Lyon, 08/09/2015-11/09/2015*, page (support électronique), http://www.traitementdusignal.fr/. GRETSI CNRS. 43

[Szasz et al., 2016a] Szasz, T., Basarab, A., and Kouamé, D. (2016a). Beamforming of ultrasound images modelled as stable random variables (regular paper). In *IEEE International Ultrasonics Symposium, Tours, France, 18/09/2016-21/09/2016*. 99

[Szasz et al., 2016b] Szasz, T., Basarab, A., and Kouamé, D. (2016b). Beamforming through regularized inverse problems in ultrasound medical imaging (to appear). *IEEE Transactions on Ultrasonics, Ferroelectrics and Frequency Control*. 69

[Szasz et al., 2016c] Szasz, T., Basarab, A., and Kouamé, D. (2016c). Strong reflector-based beamforming in ultrasound medical imaging. *Ultrasonics*, 66:111–124. 43

[Szasz et al., 2014] Szasz, T., Basarab, A., Vaida, M. F., and Kouamé, D. (2014). Beamforming with sparse prior in ultrasound medical imaging. In *2014 IEEE International Ultrasonics Symposium*, pages 1077–1080. 43

[Szasz et al., 2016d] Szasz, T., Basarab, A., Vaida, M. F., and Kouamé, D. (2016d). Elastic-net based beamforming in medical ultrasound imaging. In *2016 IEEE 13th International Symposium on Biomedical Imaging (ISBI)*, pages 477–480. 69

[Tanter and Fink, 2014] Tanter, M. and Fink, M. (2014). Ultrafast imaging in biomedical ultrasound. *IEEE Transactions on Ultrasonics, Ferroelectrics, and Frequency Control*, 61(1):102–119. 101, 102

[Taxt and Strand, 2001] Taxt, T. and Strand, J. (2001). Two-dimensional noise-robust blind deconvolution of ultrasound images. *IEEE Transactions on Ultrasonics, Ferroelectrics, and Frequency Control*, 48(4):861–866. 18

[Thomenius, 1996] Thomenius, K. E. (1996). Evolution of ultrasound beamformers. In *, 1996 IEEE Ultrasonics Symposium, 1996. Proceedings*, volume 2, pages 1615–1622 vol.2. xxiv, 22

[Tian and Van Trees, 2001] Tian, Z. and Van Trees, H. (2001). Beamspace MODE. In *Conference Record of the Thirty-Fifth Asilomar Conference on Signals, Systems and Computers, 2001*, volume 2, pages 926–930 vol.2. xxix, 73

[Tibshirani, 1996] Tibshirani, R. (1996). Regression shrinkage and selection via the lasso. *Journal of the Royal Statistical Society. Series B (Methodological)*, pages 267–288. 62

[Tikhonov, 1963] Tikhonov, A. (1963). Solution of Incorrectly Formulated Problems and the Regularization Method. *Soviet Math. Dokl.*, 5:1035/1038. xxix, 40, 76

[Tropp and Gilbert, 2007] Tropp, J. A. and Gilbert, A. C. (2007). Signal recovery from random measurements via orthogonal matching pursuit. *Information Theory, IEEE Transactions on*, 53(12):4655–4666. 62

[Tur et al., 2011] Tur, R., Eldar, Y. C., and Friedman, Z. (2011). Innovation rate sampling of pulse streams with application to ultrasound imaging. *Signal Processing, IEEE Transactions on*, 59(4):1827–1842. xxvii, 39, 44

[Van Veen and Buckley, 1988] Van Veen, B. D. and Buckley, K. M. (1988). Beamforming: A versatile approach to spatial filtering. *IEEE assp magazine*, 5(2):4–24. xxiv, 18

[Vega et al., 2014] Vega, M., Molina, R., and Katsaggelos, A. K. (2014). Parameter estimation in Bayesian Blind Deconvolution with super Gaussian image priors. In *2014 22nd European Signal Processing Conference (EUSIPCO)*, pages 1632–1636. 113

[Viola et al., 2008] Viola, F., Ellis, M. A., and Walker, W. F. (2008). Time-Domain Optimized Near-Field Estimator for Ultrasound Imaging: Initial Development and Results. *IEEE Transactions on Medical Imaging*, 27(1):99–110. 41

[Wagner et al., 2012] Wagner, N., Eldar, Y. C., and Friedman, Z. (2012). Compressed beamforming in ultrasound imaging. *Signal Processing, IEEE Transactions on*, 60(9):4643–4657. 39, 44

[Wagner et al., 1987] Wagner, R. F., Insana, M. F., and Brown, D. G. (1987). Statistical properties of radio-frequency and envelope-detected signals with applications to medical ultrasound. *Journal of the Optical Society of America A*, 4(5):910. 100

[Wan and Ebbini, 2009] Wan, Y. and Ebbini, E. S. (2009). A post-beamforming 2-D pseudoinverse filter for coarsely sampled ultrasound arrays. *IEEE Transactions on Ultrasonics, Ferroelectrics, and Frequency Control*, 56(9):1888–1902. 41

[Xu et al., 2014a] Xu, M., Yang, X., Ding, M., and Yuchi, M. (2014a). Spatio-temporally smoothed coherence factor for ultrasound imaging [correspondence]. *Ultrasonics, Ferroelectrics and Frequency Control, IEEE Transactions on*, 61(1):182–190. xxiv, 17

[Xu et al., 2014b] Xu, M., Yang, X., Ding, M., and Yuchi, M. (2014b). Spatio-temporally smoothed coherence factor for ultrasound imaging [Correspondence]. *IEEE Transactions on Ultrasonics, Ferroelectrics, and Frequency Control*, 61(1):182–190. 28, 30

[Yardibi et al., 2008] Yardibi, T., Li, J., and Stoica, P. (2008). Nonparametric and sparse signal representations in array processing via iterative adaptive approaches. In *2008 42nd Asilomar Conference on Signals, Systems and Computers*, pages 278–282. 35

[Yardibi et al., 2010] Yardibi, T., Li, J., Stoica, P., Xue, M., and Baggeroer, A. B. (2010). Source localization and sensing: A nonparametric iterative adaptive approach based on weighted least squares. *Aerospace and Electronic Systems, IEEE Transactions on*, 46(1):425–443. 47

[Yu et al., 2012] Yu, C., Zhang, C., and Xie, L. (2012). A blind deconvolution approach to ultrasound imaging. *IEEE Transactions on Ultrasonics, Ferroelectrics, and Frequency Control*, 59(2):271–280. 75

[Zhang, 2009] Zhang, Y. (2009). User-guide for yall1: Your algorithms for l1 optimization. xxx, 75

[Zhao et al., 2015a] Zhao, J., Wang, Y., Zeng, X., Yu, J., Yiu, B. Y. S., and Yu, A. C. H. (2015a). Plane wave compounding based on a joint transmitting-receiving adaptive beamformer. *IEEE Transactions on Ultrasonics, Ferroelectrics, and Frequency Control*, 62(8):1440–1452. 13

[Zhao et al., 2016a] Zhao, N., Basarab, A., Denis, K., and Tourneret, J.-Y. (2016a). Joint Segmentation and Deconvolution of Ultrasound Images Using a Hierarchical Bayesian Model based on Generalized Gaussian Priors. *IEEE Transactions on Image Processing*, 25(8):3736–3750. 113

[Zhao et al., 2014] Zhao, N., Basarab, A., Kouamé, D., and Tourneret, J.-Y. (2014). Restoration of ultrasound images using a hierarchical Bayesian model with a generalized Gaussian prior. In *2014 IEEE International Conference on Image Processing (ICIP)*, pages 4577–4581. 98

[Zhao et al., 2015b] Zhao, N., Basarab, A., Kouamé, D., and Tourneret, J. Y. (2015b). Joint Bayesian deconvolution and pointspread function estimation for ultrasound imaging. In *2015 IEEE 12th International Symposium on Biomedical Imaging (ISBI)*, pages 235–238. 41

[Zhao et al., 2016b] Zhao, N., Wei, Q., Basarab, A., Dobigeon, N., Denis, K., and Tourneret, J.-Y. (2016b). Fast Single Image Super-resolution using a New Analytical Solution for l2-l2 Problems. *IEEE Transactions on Image Processing*. xxxii, 100

[Zhou et al., 2015] Zhou, X., Zhou, F., and Bai, X. (2015). Parameter estimation for LP regularized image deconvolution. In *2015 IEEE International Conference on Image Processing (ICIP)*, pages 4892–4896. 113

[Zolotarev, 1957] Zolotarev, V. (1957). Mellin-Stieltjes Transforms in Probability Theory. *Theory of Probability & Its Applications*, 2(4):433–460. 103

[Zou and Hastie, 2005] Zou, H. and Hastie, T. (2005). Regularization and variable selection via the elastic net. *Journal of the Royal Statistical Society: Series B (Statistical Methodology)*, 67(2):301–320. xxix, 70

Résumé

L'imagerie ultrasonore (US) permet de réaliser des axamens medicaux non invasifs avec des méthodes d'acquisition rapides à des coûts modérés. L'imagerie cardiaque, abdominale, fœtale, ou mammaire sont quelques-unes des applications où elle est largement utilisée comme outil de diagnostic.

En imagerie US classique, des ondes acoustiques sont transmises à une région d'intérêt du corps humain. Les signaux d'écho rétrodiffusés, sont ensuite formés pour créer des lignes radiofréquences.
La formation de voies (FV) joue un rôle clé dans l'obtention des images US, car elle influence la résolution et le contraste de l'image finale.

L'objectif de ce travail est de modéliser la formation de voies comme un problème inverse liant les données brutes aux signaux RF. Le modèle de formation de voies proposé ici améliore le contraste et la résolution spatiale des images échographiques par rapport aux techniques de FV existants.

Dans un premier temps, nous nous sommes concentrés sur des méthodes de FV en imagerie US. Nous avons brièvement passé en revue les techniques de formation de voies les plus courantes, en commencent par la méthode par retard et somme standard puis en utilisant les techniques de **formation de voies adaptatives**.

Ensuite, nous avons étudié l'utilisation de signaux qui exploitent une **représentation parcimonieuse** de l'image US dans le cadre de la formation de voies. Les approches proposées détectent les réflecteurs forts du milieu sur la base de critères bayésiens.

Nous avons finalement développé une nouvelle façon d'aborder la formation de voies en imagerie US, en la formulant comme un **problème inverse linéaire** liant les échos réfléchis au signal final. L'intérêt majeur de notre approche est la flexibilité dans le choix des hypothèses statistiques sur le signal avant la formation de voies et sa robustesse dans à un nombre réduit d'émissions.

Finalement, nous présentons une nouvelle méthode de formation de voies pour l'imagerie US basée sur l'utilisation de caractéristique statistique des signaux supposée α**-stable**.